Astronomy Letters, Vol. 26, No. 9, 2000, pp. 553–557. Translated from Pis'ma v Astronomicheskiĭ Zhurnal, Vol. 26, No. 9, 2000, pp. 643–648.
Original Russian Text Copyright © 2000 by Tokarev, Kaĭser, Boĭko, Gustov.

Anisotropy of the Hectometer Cosmic Radio Background

Yu. V. Tokarev[1]*, M. L. Kaĭser[2], G. N. Boĭko[1], and P. V. Gustov[3]

[1] *Radiophysical Research Institute, Nizhni Novgorod State University, ul. Lyadova 25/14, GSP-51, Nizhni Novgorod, 603600 Russia*
[2] *NASA Goddard Space Flight Center, 8800 Greenbelt Road, Greenbelt, MD 20771, USA*
[3] *Nizhni Novgorod State University, pr. Gagarina 23, Nizhni Novgorod, 603600 Russia*

Received December 2, 1999

Abstract—The angular anisotropy of cosmic radio emission at frequencies of 260, 512, 772, and 1028 kHz was studied on the WIND spacecraft when it moved to a distance of ~1.5×10^6 km from the Earth at the deepest phase of the last solar minimum. The modulation index of the temperature of the spacecraft dipole antenna rotating in the plane of the ecliptic was found to have an indistinct frequency dependence with a maximum of 17% near 500 kHz. This result modifies significantly the conclusions of the only similar experiment on the IMP-6 spacecraft carried out under less favorable observing conditions. Existing ideas about the causes of the radio-background anisotropy in the opacity region of the Galactic gas disk are briefly reviewed. © *2000 MAIK "Nauka/Interperiodica".*

Key words: *Galaxy (Milky Way system)*

INTRODUCTION

The Galactic gas disk is known to be optically opaque to radio waves at frequencies $f \leq 0.$ MHz. Studies of the cosmic radio emission in this frequency band yield valuable information about the structure of the interstellar medium and the magnetic field in the immediate (≤0.5 kpc) vicinity of the Solar system.

At present, information about the ultralow-frequency cosmic radio emission is exhausted by the data obtained more than 20 years ago on the IMP-6 (Brown 1973) and RAE-2 (Novaco and Brown 1978) spacecraft. The IMP-6 receiver was equipped with a 91-m dipole antenna spin-stabilized in the plane of the ecliptic. The absolute values and intensity spectrum $I(f)$ of the radio background were measured at 32 discrete frequencies in the range 0.13–2.6 MHz. Because of the spacecraft rotation, the modulation index m, which describes the background angular nonuniformity, and the ecliptic longitude $L_{\max}$ of the effective "pointlike" radio source responsible for the observed background anisotropy were also measured.

Sporadic radio emission from the Earth and the Sun is one of the main interfering factors in such measurements. In order to reduce the effect of these factors, we used a special, fairly laborious technique when reducing the IMP-6 data. Nevertheless, the problem proved to be rather serious for this spacecraft, which operated at relatively small distances from the Earth (up to 200 000 km at the apogee). In particular, doubts remained as to whether the frequency dependence $m(f)$ at $f <$ 400 kHz, where interference from the circumterrestrial kilometric radio emission (CKR) and the surrounding plasma is significant, were properly determined, as well as about the location of the Galactic source, the directions to which during the observations (the spring of 1971) turned out to be close to the earthward direction (Brown 1973).

The RAE-2 observations were carried out with a *V*-shaped 229-m antenna with a nearly dipole beam at $f < 1$ MHz. To reduce the Earth's influence, the RAE-2 observations were performed in circumlunar orbits near a new moon, when the sources of radio interference are screened by the Earth's ionosphere. The radio background spectra were measured in four characteristic directions: the center, anticenter, south and north poles of the Galaxy (Novaco and Brown 1978). The radio background intensity for these directions was determined by a relative method using measured IMP-6 spectra as the reference ones.

Collectively, the IMP-6 and RAE-2 data could give a comprehensive idea of the large-scale features of the hectometer cosmic radio emission. Unfortunately, the above doubts as to whether the CKR effect was properly taken into account slightly reduce the value of the conclusions reached by Brown (1973) about the spectrum and anisotropy of the radio background at extremely low frequencies.

A good opportunity to eliminate this drawback appeared after the launch of the WIND spacecraft with the WAVES radio receiver (RAD1) and a 100-m dipole antenna on board, designed to study electromagnetic emissions in the range 20–1040 kHz (Bougeret *et al.* 1995). Of particular interest are the segments of the space-

* E-mail address for contacts: yt@nirfi.sci-nnov.ru

1063-7737/00/2609-0553$20.00 © 2000 MAIK "Nauka/Interperiodica"

craft orbit furthest from the Earth (up to 1.5×10^6 km), where the CKR effect must be greatly reduced. In late 1997, one of us proposed and implemented a program of observations, in which the spacecraft location at maximum distances from the Earth coincided with the deepest phase of the last solar minimum.

The low probability of occurrence of interfering sporadic emissions from the Earth and the Sun, the larger distance of the WIND spacecraft from the Earth, and the possibility of observing the Galactic "radio source" at various elongations allowed us to study the angular anisotropy of the hectometer radio background under more favorable conditions than those on IMP-6.

In this paper, we present the WIND measurements of the modulation index and the preferential arrival angles of the cosmic radio emission at frequencies of 260, 516, 772, and 1028 kHz from December 1997 until October 1998; we also compare them with the IMP-6 measurements and discuss probable causes of the observed angular anisotropy in the Galactic hectometer radio background.

OBSERVING CONDITIONS AND TECHNIQUE

From its launch on November 1, 1994, until October 1997, the WIND spacecraft was in elliptical orbits. After its encounter with the Moon on October 15, 1997, it was sent to the Lagrangian point L1, and from December 1997 until April 1998, it was in its vicinity in the so-called halo orbits with a mean distance from the Earth sunward of about 1.4×10^6 km.

The RAD1 WAVES receiver is equipped with two mutually orthogonal dipole antennas, one of which (*S*) lies in the plane of the ecliptic and the other (*Z*) is oriented along the spacecraft spin axis stabilized in the direction of the poles of the ecliptic. The lengths of the *S* and *Z* antennas are 100 and 15 m, respectively.

The spacecraft attitude control system allows the angle between the sunward direction and the *S*-antenna axis, counted clockwise as viewed from the north pole of the ecliptic, to be measured. All the data presented below refer to the *S* antenna.

In the standard mode of measurements, the RAD1 WAVES receiver scans the operating frequency range 20–1040 kHz with a frequency step of 4 kHz in 91.632 s. The outputs of all antennas are sampled sequentially. The reception bandwidth is 2 kHz, and the signal detection time is 0.119 s. The control system provides RAD1 switching to a mode with a different step (a multiple of 4 kHz) for certain restrictions on the number of working frequencies or to a mode with a fixed frequency of observation.

This experiment aimed at performing simultaneous observations in the widest possible frequency range with a time resolution high enough to estimate the angular coordinates of the effective source of the observed radio background anisotropy. The main series of observations was carried out on December 26–30, 1997, near the winter solstice. At this time, the spacecraft was at a distance of about 1.4×10^6 km from the Earth, the deviations from the Earth–Sun line and from the plane of the ecliptic did not exceed 120 000 km, and the rotation period was 3.00169 s.

Based on the capabilities of the RAD1 operation control system, we chose four frequencies for the observations: 260, 516, 772, and 1028 kHz. During the experiment, the receiver was switched to the mode of operation at four frequencies on each day near 21^h UT. Subsequently, 20-min-long observing sessions were carried out, during which the radio background intensity was first measured at 260 kHz and then sequentially at 516, 772, 1028, 260 kHz, etc. At each frequency, the signals from the *S* and *Z* antennas were recorded separately. Given the switchings, the data sampling period T_s at the output of each antenna at a specified frequency was 1.432 s.

When choosing the working frequencies, we also took into account the fact that the component attributable to thermal noise of the interplanetary plasma appears in the antenna signal at very low frequencies. As the frequency decreases, this component becomes dominant, and the Galactic noise becomes indiscernible against its background at $f < 150$ kHz (Hoang *et al.* 1980).

The observing conditions were good enough at all working frequencies: during most sessions, we observed no appreciable random perturbations of the recorded signals caused by sporadic radio emissions, such as solar type III bursts and CKR.

The data reduction showed stability of our results (average signal level, modulation index, direction to the emission peak) from session to session for the three upper frequencies. The records at 260 kHz were noisier; a daily scatter of the above parameters was noticeable even for the most stationary record segments. A probable cause is the residual effect of many weak, merging (in time) bursts of sporadic radio emission from the Earth and the Sun, which are difficult to separate from the Galactic radio noise. Therefore, the observations at 260 kHz were continued in the succeeding months at different position angles between the Earth–Sun line and the directions to the Galactic source.

Additional sessions were carried out on January 24–28, April 2–5, and October 4–10, 1998. Unfortunately, because of the growing solar activity, the observing conditions were not so favorable as those in December 1997, and only individual fragments of the records during the January 24–25, April 5, and October 4, 1998 sessions were included in the data reduction. On January 24 and 25, we also performed reference observations at 772 kHz, which confirmed the stability of our results at this frequency. In the last three series, we used a single-frequency recording mode of RAD1 with a data sampling period of 0.358 s.

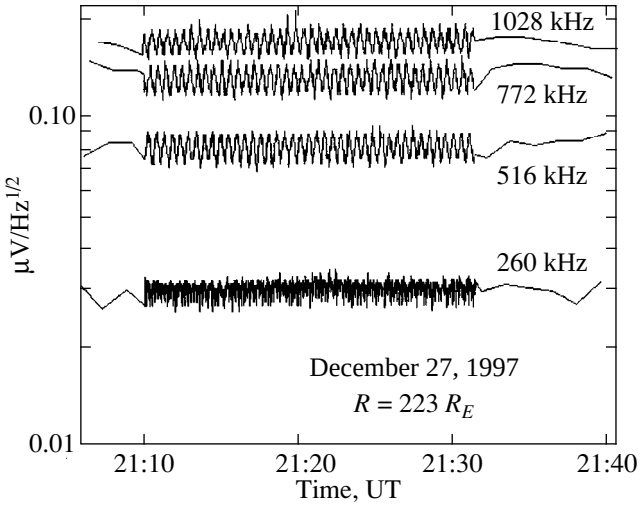

Fig. 1. Oscillograms of the cosmic noise recorded by the *S* antenna of the RAD1 WAVES receiver during the December 27, 1997 (UT) session. From top to bottom: signal voltages in the 1028, 772, 516, and 260 kHz channels (on a logarithmic scale). The beginning and end of the record correspond to the standard operation mode of the receiver with a scanning of the range 20–1040 kHz over 64 frequency channels.

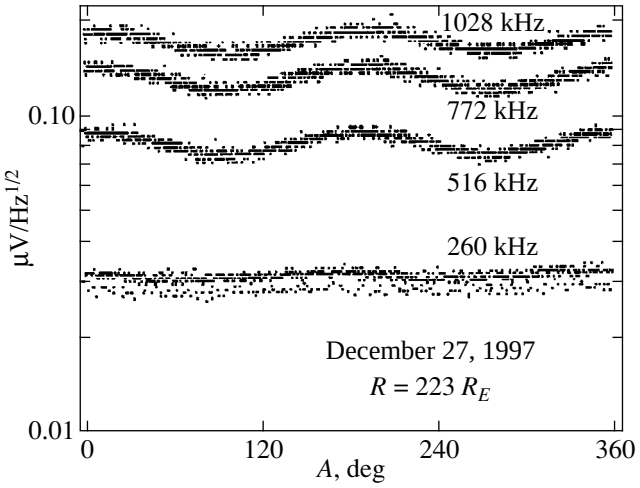

Fig. 2. Signal–angle plots constructed by the superposed-epoch technique for the December 27, 1997 session. Output voltage of the rotating *S* antenna is along the vertical axis; azimuthal angle *A* of the antenna axis, counted clockwise from the sunward direction, is along the horizontal axis.

RESULTS

Data on the output voltage of the RAD1 WAVES antennas are digitized in units of $\mu V\ Hz^{-1/2}$. The attitude control system outputs information about the *S*-antenna azimuth with respect to the sunward direction to within a 0.1 degree and the spacecraft rotation period.

By way of illustration, Fig. 1 shows oscillograms of the signals from the *S*-antenna output in the December 27, 1997 session. When RAD1 is switched from the standard mode (the beginning and end of the records correspond to this mode) to the mode of scanning over the four chosen frequencies, quasi-sinusoidal noise variations in the 516, 772, and 1028 kHz channels are clearly seen. The observed modulation with a quasi-period of 31.4 s is the result of a stroboscopic effect, because the data sampling time in this cycle, 1.431 s, was not enough to reproduce the fundamental modulation period of the dipole antenna signal equal to half the spacecraft rotation period for a continuous recording. The logarithmic scale along the vertical axis allows the relative depths of the variations at various frequencies to be directly compared.

At 260 kHz, the spectral composition of the variations is considerably richer. It should be noted that, at this frequency, the rare undershoots associated with partial blocking of the receiver input during the operation of other spacecraft instruments (telemetry, etc.) give some contribution to the observed signal modulation depth. For a more detailed study of the observed modulation, we constructed angular plots from original records by the superposed-epoch technique. Figure 2 shows a sample angular plot for the December 27, 1997 session.

It is easy to show that, for a rotating dipole antenna, the antenna-signal intensity I as a function of angle A can be represented as

$$I(A) = I_{max}[1 - m\cos(2(A - A_0))]/(1 + m),$$

where $m = (I_{max} - I_{min})/(I_{max} + I_{min})$ is the modulation index; I_{max}, and I_{min} are the mean maximum and mini-

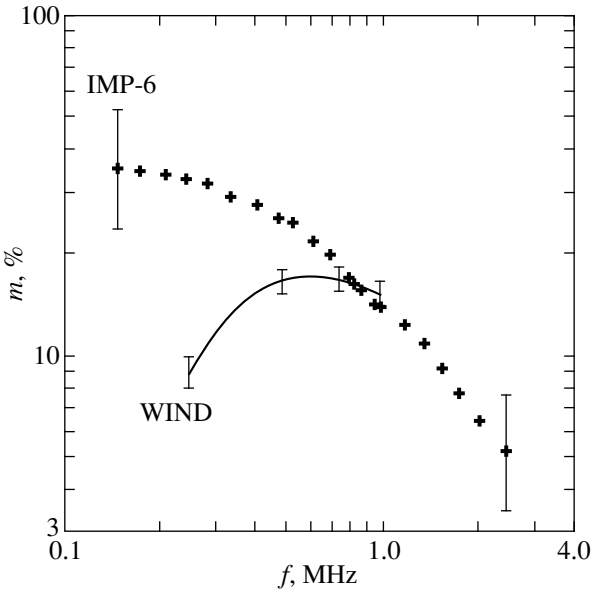

Fig. 3. Modulation index of the hectometer cosmic radio background as observed with the dipole antenna. The experimental data are fitted by the solid curve, and the IMP-6 observations are indicated by the dotted line. The vertical bars give admissible limits of *m* variations due to measurement errors.

Table 1

Observing session	December 1997					1998			
Date	26	27	28	29	30	24.01	25.01	05.04	04.10
m, %	2	6	9	5	4	8	8	18	19
L_{max}, deg	–	176	183	129	128	162	163	191	203

mum signal intensities of the rotating-antenna signal; and A_0 is the azimuthal angle of the antenna when it is directed toward the radio background maximum.

Fitting experimental angular plots by the dependence specified for $I(A)$, we can determine all the parameters introduced in it.

The ecliptic longitude of the radio emission maximum L_{max} is related to A_0 and the ecliptic longitude of the Sun L by $L_{max} = L - A_0(\pm 180°)$; the last term takes into account the 180-degree unertainty during observations with a dipole antenna. Clearly, for a stationary source, the azimuth A_0 must change with L from session to session by about one degree in a day so as the longitude L_{max} remains constant.

As was already noted above, an analysis of the angular plots shows that, at 516, 772, and 1028 kHz, the parameters m and L_{max} determined in all sessions match, within the error limits. At the same time, a noticeable daily scatter of these parameters is observed at 260 kHz. This is illustrated by Table 1. A dash in the table means that the preferential arrival angle in the December 26, 1997 session cannot be determined.

An analysis of the variations in m and L_{max} suggests that, apart from the Galactic source, there is also some additional radio source at 260 kHz, whose mean flux slowly varies with time. Since the pattern is stable at the three high frequencies, this is most likely weak residual circumterrestrial kilometric radio emission, which is most intensely generated precisely in the 200–300-kHz band (Kaiser and Alexander 1977). However, the possibility of weak, quasi-continuous type III solar bursts, which are commonly observed in a limited frequency band during interplanetary storm activity, cannot be ruled out either (Bougeret *et al.* 1984a).

To test this hypothesis, we represented the angular plots at 260 kHz as

$$I(A) = I_{max}[1 - m\cos(2(A - A_0))]/(1 + m) + I_0[1 - \cos(2A)],$$

where I_0 is the intensity of the second source. When deriving this relation, we assumed that the modulation index for the second source is equal to unity, and that its azimuth in the angular plot is either 0° or 180°. The former simplification does not result in any large errors unless the source angular size exceeds 10°. The latter simplification is justified by the spacecraft location near the Earth–Sun line far from the Earth.

After such a correction for the effect of interfering emissions along the Earth–Sun line, the sought-for quantities m and L_{max} at 260 kHz showed a satisfactory stability from session to session, which, in particular, justifies our assumptions. The decrease of the observed modulation index in the December session, when the position angle between the Earth–Sun line and the direction toward the Galactic source was close to 90°, and its increase in the April 5, 1998 and October 4, 1998 sessions, when the source was virtually on this line (see Fig. 3), can also be explained in terms of the model of two sources.

The resulting modulation index and ecliptic longitude of the effective Galactic radio source at the chosen frequencies are presented in Table 2 and in Fig. 3.

As follows from Table 2, the directions of the preferential arrival of radio waves are close to those determined by Brown (1973) for f = 600 kHz. He noted that the region of enhanced radio emission is localized at about 30° from the Galactic pole. The 180-degree uncertainty in observations with a dipole antenna does not allow us to exclude any of the two possible, diametrically opposite directions. The RAD1 observations show a tendency for L_{max} to increase with decreasing frequency of observation in the 1028–256-kHz band. As for the modulation index, the values of m at 500–1000 kHz are close, within the error limits, to those obtained by Brown (1973). At the same time, the frequency dependence $m(f)$ measured in the present experiment differs markedly in pattern from that obtained on the IMP-6 spacecraft. Instead of a monotonic increase in m with decreasing frequency f, a dependence with an indistinct maximum near $f \sim 600$ kHz is observed (see Fig. 3).

The favorable observing conditions on the WIND spacecraft mentioned above determine a higher reliability of the newly obtained data on the angular anisotropy of the hectometer cosmic radio background.

Table 2

f, kHz	260	516	772	1028
m, %	9 ± 1	17 ± 1	17.3 ± 1	16.3 ± 1
L_{max}, deg	185 ± 3	179 ± 2	177 ± 1	173 ± 1

CONCLUSION

When the peculiarities of the low-frequency cosmic radio background are discussed, two circumstances must first be taken into account. Because of the interstellar absorption of radio waves, the intensity of the Galactic radio emission is virtually completely deter-

mined by local sources in the region whose radius r can be found from the condition $\kappa r \simeq 1$, where κ is the absorption coefficient of the radio waves. According to existing estimates for the diffuse interstellar medium, $\kappa = 4 \times 10^{-3} (f_{[\mathrm{MHz}]})^{-2.1}$ [pc^{-1}]. In this case, the value of r, which may be called a visibility horizon, is smaller than the characteristic half-thickness of the Galactic gas disk (~500 pc) even near 1 MHz, decreasing to 15 pc at f = 260 kHz. The second important factor is a large (by more than two orders of magnitude) decrease of the radio background intensity with decreasing frequency f in the 1028–260-kHz band.

The available ideas of the nature of the observed anisotropy in the hectometer cosmic radio emission are few in number. Shortly after the first spacecraft with radio receiving equipment onboard were placed into orbit, Getmantsev (1965) essentially predicted the modulation of cosmic radio noise in observations with a rotating antenna. He associated this phenomenon with the beaming properties of synchrotron radio emission and expected its occurrence when the visibility horizon would become smaller than the uniformity scale of the Galactic magnetic field with decreasing f. According to his calculations, for the index of energy distribution of radioemitting electrons $\gamma = 3$, the modulation index m_s in measurements with a dipole antenna must be 23% and decrease to zero with decreasing γ.

In the literature, the observed anisotropy of the low-frequency radio background is usually associated with some radio source located near the north Galactic pole (Bougeret *et al.* 1984b). The 180-degree uncertainty in the source's position was removed after observations of its occultation by the coma of Comet Giacobini–Zinner on the ICE spacecraft; in the model of a spherically symmetric radio brightness distribution, its angular size must be about 70° (Steinberg *et al.* 1986).

Leaving a detailed interpretation of the hectometer radio background anisotropy for subsequent studies, we only note that the models considered to date—synchrotron radiation from a region of uniform magnetic field and an isolated local radio source—do not exhaust all the possibilities of explaining of the observed pattern. In particular, an analysis of frequency and angular variations in the intensity of cosmic radio emission in terms of the most realistic models for the spatial distribution of synchrotron sources and the ionized interstellar gas in the immediate vicinity of the Solar system seems very promising. In any case, the newly obtained information about the modulation index and the preferential arrival angles the low-frequency cosmic radio emission must be an important component in such studies.

ACKNOWLEDGMENTS

We are grateful to the Russian Foundation for Basic Research (project no. 99-02-17285) and to the INTAS Foundation (grant no. 97-1964) for financial support.

REFERENCES

1. J.-L. Bougeret, M. L. Kaiser, P. J. Kellogg, *et al.*, Space Sci. Rev. **71**, 231 (1995).
2. J.-L. Bougeret, J. Fainberg, and R. G. Stone, Astron. Astrophys. **136**, 255 (1984a).
3. J.-L. Bougeret, J. Fainberg, and R. G. Stone, Astron. Astrophys. **136**, 17 (1984b).
4. L. W. Brown, Astrophys. J. **180**, 359 (1973).
5. G. G. Getmantsev, Kosm. Issled. **3**, 495 (1965).
6. S. Hoang, J.-L. Steinberg, G. Epstein, *et al.*, J. Geophys. Res. **85**, 3419 (1980).
7. M. L. Kaiser and J. K. Alexander, J. Geophys. Res. **82**, 3273 (1977).
8. J. C. Novaco and L. W. Brown, Astrophys. J. **221**, 114 (1978).
9. J.-L. Steinberg, J. Fainberg, N. Meyer-Vernet, and S. Hoang, Geophys. Res. Lett. **13**, 407 (1986).

Translated by G. Rudnitskii

Astronomy Letters, Vol. 26, No. 9, 2000, pp. 558–564. Translated from Pis'ma v Astronomicheskiĭ Zhurnal, Vol. 26, No. 9, 2000, pp. 649–656.
Original Russian Text Copyright © 2000 by Efremov.

Dense Star Clusters as the Sources of Gamma-Ray-Burst Progenitors

Yu. N. Efremov*

Sternberg Astronomical Institute, Universitetskiĭ pr. 13, Moscow, 119899 Russia

Received January 20, 2000

Abstract—Two independent sets of arguments lead us to conclude that the progenitors of superintense bursts (with an energy yield larger than that for ordinary supernovae by one or two orders of magnitude) are born in massive dense star clusters, but generally flare up only after they have left the cluster; these are the same objects that are the progenitors of gamma-ray bursts (GRBs). Each of the giant stellar arcs which are grouped into multiple systems of stellar complexes in the LMC and NGC 6946 could only be produced by a single powerful energy release near its center. The progenitors of these systems of arc-shaped stellar complexes must have had a common source nearby, and it could only be a massive star cluster. Such clusters are actually known near both systems. On the other hand, calculations of the dynamical evolution of star clusters show that close binary systems of compact objects are formed in the dense central parts of the clusters and are then ejected from them during triple encounters. Mergers of the components of such systems are believed to be responsible for GRBs. Since their progenitors are ejected from the cluster before merging, the arc-shaped stellar complexes produced by GRBs are observed near (but not around) the parent clusters. If a considerable fraction of the GRB progenitors are formed as a result star encounters in massive star clusters, and if the GRBs themselves trigger star formation near the parent clusters, then observations of GRBs in star-forming regions are consistent with their origin during mergers of pairs of compact objects. *© 2000 MAIK "Nauka/Interperiodica".*

Key words: *star clusters and associations, stellar dynamics, gamma-ray bursts, star formation*

INTRODUCTION

Recently, we have hypothesized that the system of three or four giant stellar arcs in the region of the supershell LMC 4 in the Large Magellanic Cloud (LMC) was produced by explosions of the objects that left the old rich cluster NGC 1978 in the same region (Efremov 1999). These giant arcs are the complexes of star clusters of the approximately same (in each arc) age that evidently formed from the gas supershells swept up by some source of central pressure (Efremov and Elmegreen 1998). New data (Braun *et al.* 2000) confirm that there is no concentration of main-sequence stars with ages of about 30 Myr at the center of the most distinct arc, which would be expected if the hypothesis of Efremov and Elmegreen (1998) that this arc was produced by supernovae in a presently old association were valid. The need for assuming an abnormal luminosity function in such an association makes this hypothesis unlikely. The hypothesis that the arcs were produced by presently barely noticeable clusters or associations does not explain their concentration in the same region of the LMC and the absence of stellar arcs (or H I supershells) around many rich clusters in the LMC and other galaxies either (Efremov 1999, 2000).

The possibility of H I supershells being produced by powerful single explosions associated with gamma-ray bursts (GRBs) was suggested by Blinnikov and Postnov (1998). This possibility was considered in detail and confirmed by Efremov *et al.* (1998), who also pointed out that giant arcs of young stars like those observed in the LMC 4 region are formed from such supershells as well. Differences in the parameters of the supershells born after single superexplosions and after multiple supernova explosions were studied by Efremov *et al.* (1999), who used the stellar arcs in the region of the supershell LMC 4 as an example to show that they could be produced by a single superexplosion.

The concentration of stellar arcs in the neighborhood of each other clearly suggests that their progenitors were born somewhere in the same region, in some common source. It is clear from the most general considerations that this must be a star cluster rich enough for objects of some rare type to be able to form in it. There is such a cluster in the LMC 4 region, NGC 1978 (Efremov 1999), but there are no stellar arcs immediately around it. Therefore, the progenitors of the arcs must have a unique combination of properties: they are born in a cluster, but leave it and, before exploding, go away to a large distance, up to several hundred parsecs. Such objects turn out to exist. Moreover, these are the objects that have long been suggested as candidates for

* E-mail address for contacts: efremov@sai.msu.su

GRB progenitors without any association whatsoever with star clusters or arcs!

BINARY SYSTEMS OF COMPACT OBJECTS IN CLUSTERS

A unique type of objects which are born precisely in a dense star cluster, but inevitably leave it in the course of time are close binary systems whose both components are compact objects—neutron stars or black holes. The line of reasoning here is as follows. Many binaries with compact objects are not primary ones, but are formed in the dense central parts of globular clusters through triple star encounters. The high relative frequency of X-ray binaries in globular clusters (see, e.g., Bailyn 1996), two orders of magnitude larger than that in the field, is known to be explained precisely by this kind of processes. It is equally well known [the so-called law of Heggie (1975)] that encounters of close binaries with other cluster members make them increasingly close due to an increase in velocity dispersion in the cluster (whereas wider pairs immediately break up). This process continues until close binaries are disrupted through mergers of their components or acquire velocities high enough to escape from the cluster through triple or quadruple encounters (MacMillan *et al.* 1990). This process is effective in the dense central regions of globular clusters, into which more massive cluster members fall via mass segregation in a time of ~1 Gyr (MacMillan 1995) and considerably faster in open clusters (Kroupa 2000).

Thus, during each new encounter, a close binary becomes increasingly close, while its velocity in the cluster increases—the system (as well as the third star) acquires an increasingly large recoil velocity. In a system of normal stars, the components can merge together to form a peculiar blue star—a blue straggler. We emphasize that it is their abundance that accounts for the high ultraviolet brightness of the dense central region in NGC 1978 (Cole *et al.* 1997). However, if a system consists of two compact objects (whose sizes are many orders of magnitude smaller than those of normal stars), it acquires a velocity through multiple encounters with stars passing nearby that is high enough to escape from the cluster before its components merge together. This velocity for a typical globular cluster is ~40 km s^{-1} (Davies 1995).

Recently, the dynamical evolution of a cluster containing black holes has been extensively studied by Portegies Zwart and MacMillan (1999, 2000). They concluded that, in a time of about 1 Gyr for a globular cluster, black holes are drawn to the cluster core to form binaries with one another through triple encounters. Even if a black hole was initially a pair with a normal star, the latter rapidly gives way to another black hole. Subsequent interactions with other cluster members result in the members of a system of black holes coming closer together and in an increase in the velocity of all participants of the encounter. Numerical calculations on a dedicated GRAPE-4 computer show that, in several Gyr, well before the cluster-core collapse, 90% of the black holes are ejected from the cluster, with 30% of them as binary black holes. These calculations are in good agreement with previously obtained analytic estimates (Kulkarni *et al.* 1993; Sigurdsson and Hernquist 1993).

Of crucial importance is the fact that, if the parent clusters were very massive ($>5\times10^6 M_\odot$) or underwent core collapse shortly after their formation, so that the density and velocity dispersion at their centers were particularly large, then black holes are ejected, being already very close binaries, and merge together through gravitational radiation in a few Myr after their ejection from the cluster (Portegies Zwart and MacMillan 2000). These authors use their calculations to estimate the probability of observing gravitational radiation during mergers of black holes. However, these events, if black holes are surrounded by accretion disks, apparently also produce GRBs! It would also be natural to assume that pairs with a neutron star and a black hole must exhibit similar patterns of dynamical evolution as well.

BINARIES OF COMPACT OBJECTS AS GRB PROGENITORS

Up until now, the only ground for identifying objects capable of generating single explosions, powerful enough to produce stellar arcs or H I supershells, with GRBs has been the simple consideration that GRBs are the only known objects whose explosion energy is high enough. We now see that the property of stellar-arc triggers following from observations—to be born in a cluster, but to explode outside it—is also the property of binaries of compact objects, which are believed to be probable GRB progenitors [see the review by Postnov (1999)]. However, Paczynski (1999) points out that the model of a merger of neutron stars or black holes assumes that GRBs can be far from the parent galaxies (because the velocity of their progenitors and the time before a merger can be very large), but this is not confirmed by observations of GRB afterglows. In addition, he believes that evidence of the GRB localization in star-forming regions (and in galaxies with intense star formation), suggesting that a massive star was the direct progenitor of a GRB, also argues against this model.

The hypothesis outlined above resolves both problems in the model of a merger of compact objects noted by Paczynski (1999). Previous bursts of the objects originated from the same cluster could produce a star-forming region near it, and we know even cases of a GRB inside an H I supershell, presumably produced by a previous GRB (Ahn 1999). The presence of very massive star clusters in a galaxy, at least as old as 1 or 2 Gyr, is undoubtedly consistent with intense star formation in it, as is the case in the LMC. There are no such clusters in our Galaxy, in which the star-formation rate per unit mass is considerably lower than that in the LMC. In this

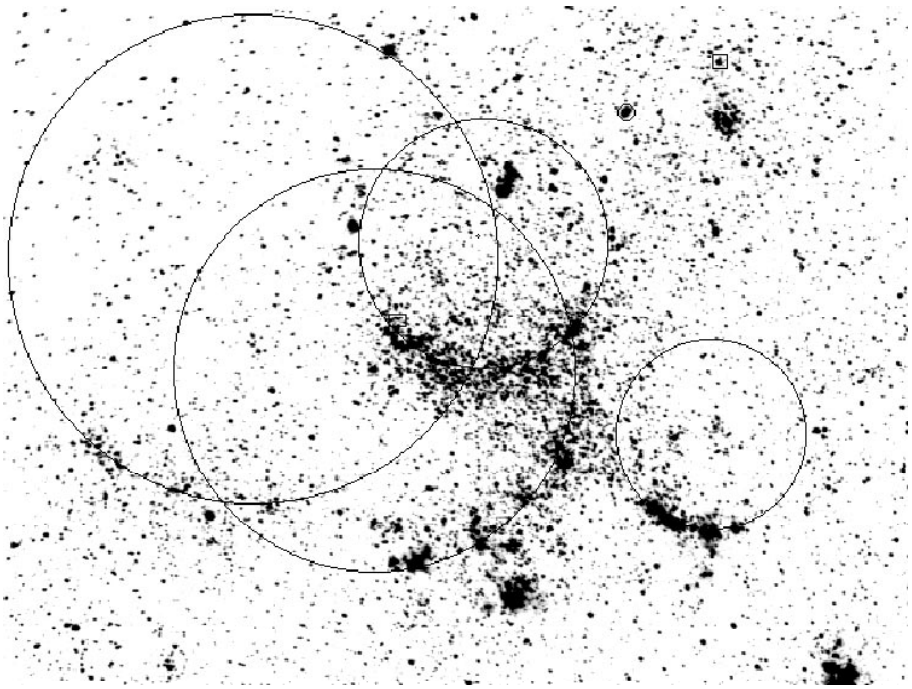

Stellar arcs in the region of the supershell LMC 4 in the LMC (from right to left in order of increasing sizes and ages): Sextant, Quadrant, Third and Fourth Arcs. The reality of the Fourth arc needs confirmation. The cluster NGC 1978 is encircled; SGR 0526-66 (not far from NGC 1978) and A0538-66 (near the left edge of Quadrant) are enclosed in squares. North is at the top, and east is on the left.

case, the absence of GRBs in elliptical galaxies, whose massive (globular) clusters are all very old and in which there is no gas, is also quite comprehensible. There are no longer objects capable for superstrong explosions in classical old globular clusters. It may also well be that some supernovae observed far from galaxies could be associated with GRBs.

PECULIARITIES OF THE CLUSTER NGC 1978 AND ITS NEIGHBORHOOD

The existence of a system of stellar arcs, which form an isolated complex of arc-shaped stellar complexes with ages of the oldest objects ~30 Myr, suggests that the "mass escape" of GRB progenitors is observed only during a few tens of Myr, probably at the stage of a particularly high core density of the parent cluster. The unusual ellipticity of NGC 1978, as well as the abundance of blue stragglers in it, may also be associated with the high density of its core.

As was already said above, the binary black holes ejected from dense clusters can be very close (because they experienced many encounters with other stars before acquiring a velocity high enough to escape from the cluster); therefore, they merge together rather rapidly not so far from the parent clusters. At a velocity of 40 km s^{-1}, an object will go away from the place of its birth to 400 pc in 10 Myr. The projected separations between the centers of the stellar arcs in the LMC and the cluster NGC 1978 are 400 and 800 pc; the actual values cannot be much larger, because, in any case, the arcs lie in the galactic plane, while the cluster is most likely located near it.

The uniqueness of the stellar arcs near NGC 1978 in the LMC most likely stems from the fact that this is a very rich and dense cluster, the most massive known cluster with an age of ~2 Gyr. The problem noted previously (Efremov 1999)—the absence of past GRBs with the center at the NGC 1978 itself—is also resolved: a merger in a pair of compact objects inside the cluster is highly unlikely, because, before this could occur, such a binary acquires a velocity after the components come closer together during encounters with a third star that is high enough to escape from the cluster.

The figure shows that the major axis of this highly elongated cluster is approximately directed toward the LMC 4 center and the centers of the two stellar arcs; on the other side of the cluster, the soft gamma repeater SGR 0526-66 in the supernova remnant N 49 lies on the line connecting these centers and NGC 1978 (Efremov 1999). A concentration of binary stars—X-ray sources (Haberl and Pietsch 1999), probable GRB progenitors (Spruit 1999)—is observed in the northern part of LMC 4 (not far from NGC 1978). Spruit (1999) considers millisecond X-ray pulsars as the descendants of the X-ray binaries which managed to avoid the fate of turning into GRB sources. The object A0538-66, one of the two such pulsars known in the LMC, lies in the same region and near the straight line connecting the following objects from northwest to southeast: SGR 0526-66, NGC 1978, the centers of Quadrant (the most pronounced arc) and the supershell LMC 4, the center of

the Third arc, and, finally, A0538-66 (see the figure). It is unlikely that all these objects fell on the same line by chance. Note that the position angle of this straight line is ~135°, while the position angle of the NGC 1978 major axis is about 160°; they are rather similar.

The cluster may be elongated along its orbit in the LMC (its position relative to the LMC center is consistent with this possibility, considering that the LMC clusters, including the old ones, lie near the galactic plane), and it would be natural to assume that the objects which left it with a relatively low velocity are in nearly the same orbit and are closer to the cluster. The youngest stellar arc (Sextant) lies well away from this line and furthest from the cluster; all these three circumstances can be explained by a higher ejection velocity of the progenitor of this arc from the cluster.

The elongated shape of the cluster and the loss of many stars spread along the cluster orbit can also be assumed to result from the gravitational impact of NGC 1978 on the LMC plane. The formation of the supershell LMC 4 may also be associated with the passage of NGC 1978 through the LMC gas disk. However, these assumptions need to be reconciled with the dynamical time scales of all these presumed events, the possibility of which is not obvious. The elongated shape of this cluster and the possibility that many stars escape from it can also be explained by its formation during a merger of two clusters (Efremov 1999), but alternative explanations now seem more likely.

Note that there is the cluster KGS 1806, which is similar in mass and age to NGC 1978, inside the second largest H I cavity in the LMC located near the western extremity of the bar (Vucs and Roaliphs 1992).

THE SPHERICAL COMPLEX OF STAR CLUSTERS IN THE GALAXY NGC 6946

Very massive, rapidly rotating single stars, which generate stronger explosions than do ordinary supernovae—the phenomenon of a hypernova (Paczinsky 1999), are considered as alternative GRB progenitors. Such explosions are clearly most probable in extremely rich young clusters, where the normal luminosity function suggests the presence of very massive stars. Such stars can also emerge in clusters through encounters and mergers of stars in the dense cluster cores; as a result, rapidly rotating massive stars and black holes can be formed. Recent calculations show that this process is very effective (two orders of magnitude more effective than followed from analytic estimates), resulting in the fast concentration of the most massive objects in the cluster core and in the subsequent ejection of many of them during star encounters (Portegies Zwart *et al.* 1999; Kroupa 2000). According to the estimate by Kroupa (2000), 10–50% of all massive stars in open clusters go away to distances larger than twice the cluster tidal radius in 5–50 Myr. (Note that this time is appreciably shorter than the mean Cepheid age; clearly, this may explain the commonly observed locations of Cepheids, the most massive stars in those clusters whose members they are, in the cluster halos rather than in the cores. Consequently, the difference between the velocity of SZ Tau and the mean velocity of the NGC 1647 stars is not an absolute argument against this Cepheid being a cluster member.)

We may succeed in explaining the origin of the system of four or five arc-shaped complexes of star clusters in the spiral galaxy NGC 6946 by explosions of the hypernovae that left a young massive cluster (Efremov 2000). When searching for objects similar to the system of stellar arcs in the LMC, Hodge (1967) discovered only one more such structure in NGC 6946. Note that he described both systems as super-supernova remnants. More than thirty years had passed before they attracted attention. Based on 6-m telescope images, we suspected the presence of a rich cluster inside the system of arcs in NGC 6946 (Efremov 1999); shortly afterward, Larsen and Richtler (1999) reported the results of their search for young massive clusters in 21 galaxies. Being unaware of Hodge's paper, they rediscovered the system of multiple arcs in NGC 6946 by describing it as a spherical cluster of star clusters. They found a young globular cluster inside it, the brightest young cluster in the galaxies they studied.

The regular circular shape of the complex of star clusters (about 500 pc in diameter) and the presence of several eccentric arcs composed of clusters with approximately the same ages inside it suggest their formation from supershells and triggered star formation, but no sources of central pressure are seen. It cannot be a young globular cluster if preliminary age estimates, which show that its age is approximately the same (10–20 Myr) as that of the other clusters in this system, are confirmed. Its mass can be $10^6 M_\odot$ (Elmegreen *et al.* 2000).

It is tempting to assume that this giant cluster is actually older than all the others, and that the hypernovae exploded in it and nearby are responsible for the formation of the arcs of star clusters near it. There is also an alternative possibility. A star-like object, which is most likely a foreground (of our Galaxy) F–G star, lies near the complex of clusters southwest of it. If, however, this is a very compact massive cluster in NGC 6946, its age must be ~0.6 Gyr; the close binaries of compact objects, as those in the region of NGC 1978 and the LMC, that left this cluster can then be responsible for the formation of the system of cluster arcs. The giant young cluster lies at the intersection of several cluster arcs and could arise from a collision of the gas shells that produced them. These hypotheses can soon be tested by using scheduled HST and 6-m telescope observations.

CIRCUMSTANTIAL EVIDENCE FOR THE RELATIONSHIP BETWEEN GRBS AND CLUSTERS

There is also circumstantial evidence for the relationship between GRBs and star clusters. We have already noted (Efremov *et al.* 1998) the presence in M 101 of a structure similar to the multiple arcs in NGC 6946 (they both appear as circular regions of enhanced brightness with a sharp edge at low resolution) and an H I supershell with the kinetic energy corresponding to the explosions of a thousand supernovae, which was found by Kamphius *et al.* (1991). A recently published map of X-ray sources in M 101 (Wang *et al.* 1999) exhibits only two concentrations of them, each consisting of four sources, and they both lie near the structures described above. If these sources will be shown to be X-ray binaries, their concentration in the same region can be explained only by the presence of a cluster nearby from which they, as well as the progenitors of superexplosions, were ejected.

A number of facts (see, e.g., Paczynski 1999) suggest a close relationship between soft gamma repeaters (SGRs), ordinary gamma-ray bursts (GRBs), and some types of supernovae. We have already mentioned the possibility that SGR 0526-66 could be produced by an object that left the cluster NGC 1978, which lies at 18′ from it almost on the extension of the cluster major axis. There is also an alternative possibility. The young, rather compact cluster SL 463, whose age, judging by integrated *UBV* photometry, is ~60 Myr, lies 4′ northeast of N 49.

The two most extensively studied soft gamma repeaters in our Galaxy have recently been found to be located on the outskirts of young clusters (Mirabel *et al.* 1999). Judging by the presence of two red supergiants, the age of the cluster with SGR 1900+14 on its outskirts is 10–30 Myr; the other object, SGR 1806-20, also lies at the edge of a cluster, which is still embedded in a cloud of gas and dust. Both clusters are discernible only in the infrared because of the large extinction (Mirabel *et al.* 1999).

DISCUSSION AND CONCLUSION

Thus, we can surmise that, contrary to popular belief, a close binary of compact objects more commonly emerges during a capture through star encounters in the dense central part of a star cluster rather than after supernova explosions of both massive stars in the original binary (resulting in its high velocity, which, however, is not observed in three well-known pairs of neutron stars in our Galaxy, if not in a breakup of the binary; see Fryer and Kalogera 1997). This possibility was rejected as unlikely when the origin of pairs of compact objects was considered. However, recent simulations of the dynamical evolution of clusters suggest a high efficiency of pair formation during star encounters in dense clusters and lend support to the analytical conclusion that binaries of compact objects are inevitably ejected from the cluster during subsequent encounters (Portegies Zwart and MacMillan 1999, 2000; Kroupa 2000). Clearly, the velocities of the ejected binaries can differ widely, but one might expect them to be mostly close to the minimum one needed for them to escape from a massive cluster (~40 km s^{-1}); as yet there are no necessary data for verifying this. Together with the conclusion of an impending merger of the pair after its ejection from a cluster, this accounts for the absence of GRBs far from galaxies.

This implies that rich, moderately old clusters must be the sources of GRB progenitors. We provided observational data justifying this conclusion. It is near such a cluster, NGC 1978, that the unique system of four giant stellar arcs in the LMC is observed. The core density of this cluster may have been very high several tens of Myr ago, which facilitated the ejection of binaries of compact objects from it. The merger of the components of a compact binary outside the cluster accounts for the absence of stellar arcs around the NGC 1978 itself. SGR 0526-66, the only soft gamma repeater in the LMC, is located near this cluster.

An energy of the order of 10^{52} erg (Efremov and Elmegreen 1998; Efremov *et al.* 1999), which corresponds to the energy released during a merger of the components of a binary of compact objects, was needed for each of the stellar arcs near NGC 1978 to be formed. This event leads to a GRB (see the review by Postnov 1999). Even for this reason, the objects triggering the formation of stellar arcs may well be identified with nascent GRBs, although GRBs are not needed to trigger star formation—only energy release into the interstellar medium matters. Supernovae with an explosion energy of the order of 10^{52} erg undoubtedly exist, though (for example, SN 1998bw associated with the weak GRB 980425 was such a supernova), and there are several arguments for the hypothesis that GRBs are related to beamed explosions of supernovae of some types (see Paczynski 1999). But could not the observational manifestations of such a relationship be explained by the fact that a GRB triggered a supernova explosion of the nearest massive star that was ripe for this, which accounts for the well-known mismatch between the positions of SN 1998bw and GRB 980425? The weakness of this GRB could stem precisely from the fact that the beam was not directed to the observer. A supernova explosion may well be triggered in a component of the multiple system in which a GRB took place (Milgrom and Usov 2000).

Our data on the stellar arcs in the LMC suggest that they are the projections of partial spherical shells (Efremov *et al.* 1999); their orientation, which is not related to the orientation of the LMC plane, indicates that these segments of stellar spheres viewed from the side are the result of a beamed explosion or outflow rather than an isotropic explosion outside the symmetry plane of the galactic gas disk. Note that an angle at the center of the

stellar arcs of several tens of degrees and the absence of paired arcs symmetric about the center of their curvature are consistent with the model of Usov (1992, 1999); according to this model, asymmetric relativistic plasma jets, whose ultimate source of energy is the energy of rotation in the merging pairs of neutron stars, are the gamma-ray sources. A development of this model is the hypothesis by Spruit (1999) that GRB progenitors and X-ray binaries are closely related.

The hypothesis that GRBs are capable of producing H I supershells and eventually trigger star formation is in agreement with data on GRB 971214 inside the supershell that may have been produced by a previous GRB in the same region (Ahn 1999). The repetition of GRBs in the same region of the galaxy strongly suggests the presence of the source of their progenitors in it. The system of multiple arcs in NGC 6946 could still be explained by the fall of the swarm of clouds on the galactic plane, but this hypothesis does not pass for the stellar arcs in the LMC, whose ages differ markedly. The entire situation suggests that the objects generating giant stellar arcs are also responsible for GRBs. Most of their progenitors are apparently born in dense star clusters through star encounters and are ejected from them during subsequent encounters. The hypothesis of Dokuchaev *et al.* (1998) that compact binaries—GRB progenitors—can be born in galactic nuclei and produce bursts after escape from them is inconsistent with the absence of any GRB concentration toward the galactic nuclei. The possibility of hypernova explosions (accompanied by GRBs) of massive stars, up to half of which are ejected from the cluster core in a time no larger than 50 Myr (Kroupa 2000), is not ruled out either. Data on GRB afterglows are consistent with the existence of two types of their progenitors (Chevalier and Li 1999).

We may also propose the hypothesis (suggested to me by V.A. Lefebvre) that the nearby supernova exploded at the end of the 18th century, whose remnant is known as the brightest radio source in the sky, Cas A, had a beamed emission but it was not directed to the observer; that is why its explosion was not observed. An even nearer supernova explosion in the 16th century, whose X-ray remnant has recently been discovered in Vela, may have not been observed for the same reason.

It may well be that events corresponding in energy release to hundreds (but not tens of thousands) of supernovae occur fairly frequently, and they may be responsible for the formation of isolated stellar complexes with a small spread in ages. Such regions are known, for example, in the LMC (Efremov 1989). Clearly, they appear arc-shaped only at a certain angle of view; it is possible that they assume the shape of arcs only in a sufficiently homogeneous medium. Regions of star formation triggered by relativistic jets outflowing from the nuclei are known in several galaxies.

Triggered star formation may be much more common than has been generally believed. We can even assume that the GRBs which began after most binary black holes or neutron stars had left the massive clusters in which they formed triggered star formation in galactic gas disks. This may be the reason why star formation in the disks of spiral galaxies began approximately 2 Gyr later than that in their halos (globular clusters in the galactic haloes were born almost simultaneously). The fact that this delay is close to the age of NGC 1978 may be not accidental. After massive stars emerge in galactic disks, they themselves can contribute to further star formation. Recall that the formation of massive stars is not yet completely understood; it may proceed only under external pressure on a gas cloud, and other sources of such pressure were needed for the first O stars and supernovae to emerge.

ACKNOWLEDGMENTS

I am grateful to A.D. Chernin for helpful discussions and to the Russian Foundation for Basic Research (project no. 00-02-17804) for financial support. Data from the NASA Astrophysics Data System helped me immensely.

REFERENCES

1. S.-H. Ahn, Astrophys. J. Lett. **530**, L9 (2000).
2. C. D. Bailyn, Astron. Soc. Pac. Conf. Ser. **90**, 320 (1996).
3. S. I. Blinnikov and K. A. Postnov, Mon. Not. R. Astron. Soc. **293**, L29 (1998).
4. J. M. Braun, K. Altmann, and K. S. de Boer, Preprint astro-ph/0006060 (2000).
5. R. A. Chevalier and Z.-Y. Li, Astrophys. J. Lett. **520**, L29 (1999).
6. A. A. Cole, J. R. Mould, J. S. Gallagher, *et al.*, Astron. J. **114**, 1945 (1997).
7. M. B. Davies, in *Proceedings of the 174th IAU Symposium on Dynamical Evolution of Star Cluster, 1995*, Ed. by P. Hut and J. Makino (Kluwer, Dordrecht, 1995), p. 243.
8. V. I. Dokuchaev, Yu. N. Eroshenko, and L. M. Ozernoy, Astrophys. J. **502**, 192 (1998).
9. Yu. N. Efremov, *Sites of Star Formation in Galaxies: Stellar Complexes and Spiral Arms* (Nauka, Moscow, 1989).
10. Yu. N. Efremov, Pis'ma Astron. Zh. **25**, 100 (1999) [Astron. Lett. **25**, 74 (1999)].
11. Yu. N. Efremov, Vestn. Ross. Akad. Nauk **70**, 314 (2000).
12. Yu. N. Efremov and B. G. Elmegreen, Mon. Not. R. Astron. Soc. **299**, 643 (1998).
13. Yu. N. Efremov, B. G. Elmegreen, and P. W. Hodge, Astrophys. J. Lett. **501**, L163 (1998).
14. Yu. N. Efremov, S. Ehlerova, and J. Palous, Astron. Astrophys. **350**, 457 (1999).
15. B. G. Elmegreen, Yu. N. Efremov, and S. Larsen, Astrophys. J. **535**, 548 (2000).

16. C. Fryer and V. Kalogera, Astrophys. J. **489**, 244 (1997).
17. F. Haberl and W. Pietsch, Astron. Astrophys. **344**, 521 (1999).
18. D. C. Heggie, Mon. Not. R. Astron. Soc. **173**, 729 (1975).
19. P. W. Hodge, Publ. Astron. Soc. Pac. **79**, 29 (1967).
20. J. Kamphius, R. Sancisi, and T. van der Hulst, Astron. Astrophys. **244**, L29 (1991).
21. P. Kroupa, astro-ph/0001202 (2000).
22. S. R. Kulkarni, P. Hut, and S. L. W. McMillan, Nature **364**, 421 (1993).
23. S. S. Larsen and T. Richtler, Astron. Astrophys. **345**, 59 (1999).
24. S. L. W. McMillan, in *Proceedings of the 174th IAU Symposium on Dynamical Evolution of Star Cluster, 1995*, Ed. by P. Hut and J. Makino (Kluwer, Dordrecht, 1995), p. 223.
25. S. L. W. McMillan, P. Hut, and J. Makino, Astrophys. J. **362**, 522 (1990).
26. F. I. Mirabel, Y. Fuchs, and S. Chaty, astro-ph/9912446 (1999).
27. B. Paczynski, astro-ph/9909048 (1999).
28. S. Portegies Zwart and S. L. W. McMillan, astro-ph/9912434 (1999).
29. S. Portegies Zwart and S. L. W. McMillan, Astrophys. J. Lett. **528**, 17 (2000).
30. S. Portegies Zwart, J. Makino, S. L. W. McMillan, and P. Hut, Astron. Astrophys. **348**, 117 (1999).
31. K. A. Postnov, Usp. Fiz. Nauk **169**, 545 (1999).
32. S. Sigurdsson and L. Hernquist, Nature **364**, 423 (1993).
33. H. C. Spruit, Astron. Astrophys. **341**, L1 (1998).
34. T. Lucs and K. Rohlfs, Astron. Astrophys. **263**, 41 (1992).
35. V. V. Usov, Nature **357**, 344 (1992).
36. V. V. Usov, astro-ph/9909435 (1999).
37. Q. D. Wang, S. Immler, and W. Pietsch, Astrophys. J. **523**, 121 (1999).

Translated by V. Astakhov

Astronomy Letters, Vol. 26, No. 9, 2000, pp. 565–571. Translated from Pis'ma v Astronomicheskiĭ Zhurnal, Vol. 26, No. 9, 2000, pp. 657–664.
Original Russian Text Copyright © 2000 by Moisseev, Mustsevoĭ.

The Effect of Projection on the Observed Gas Velocity Fields in Barred Galaxies

A. V. Moisseev[1] and V. V. Mustsevoĭ[2]

[1] *Special Astrophysical Observatory, Russian Academy of Sciences, Nizhni Arkhyz, Stavropol Krai, 357147 Russia*
[2] *Volgograd State University, Volgograd, Russia*

Received October 18, 1999

Abstract—The problem of determining the pattern of gas motions in the central regions of disk spiral galaxies is considered. Two fundamentally different cases—noncircular motions in the triaxial bar potential and motions in circular orbits but with orientation parameters different from those of the main disk—are shown to have similar observational manifestations in the line-of-sight velocity field of the gas. A reliable criterion is needed for the observational data to be properly interpreted. To find such a criterion, we analyze two-dimensional nonlinear hydrodynamic models of gas motions in barred disk galaxies. The gas line-of-sight velocity and surface brightness distributions in the plane of the sky are constructed for various inclinations of the galactic plane to the line of sight and bar orientation angles. We show that using models of circular motions for inclinations $i > 60°$ to analyze the velocity field can lead to the erroneous conclusions of a "tilted (polar) disk" at the galaxy center. However, it is possible to distinguish bars from tilted disks by comparing the mutual orientations of the photometric and dynamical axes. As an example, we consider the velocity field of the ionized gas in the galaxy NGC 972. © *2000 MAIK "Nauka/Interperiodica"*.

Key words: *barred disk spiral galaxies, gas motion, model calculations of velocity fields*

1. INTRODUCTION

The analyses of the structure and kinematics of spiral galaxies often require detailed information on the gas motion patterns in the stellar systems considered: the rotation curve and whether the velocity field includes noncircular motions. If gas motions are circular it is enough to measure line-of-sight velocity profiles along two sections passing through the disk center to unambiguously infer the orientation parameters and determine the rotation curve (Zasov 1993). This, however, is but a first, rough approximation to the real dynamics of the gaseous disk: the velocity fields of spiral galaxies can exhibit large-scale noncircular motions amounting to 20–30 km s^{-1}, which are primarily due to the spiral pattern.

Much more detailed information can be obtained by measuring the full "velocity field," i.e., by determining the line-of-sight velocity distribution over the entire galaxy disk. This has since long become common practice among radio astronomers who use interferometry technique to measure the spectral lines of neutral or molecular gas. Similar results are obtained at optical wavelengths with panoramic spectroscopy using Fabry-Perot interferometers or multi-pupil spectrographs. The common feature of all these methods is that they all involve construction of the so-called "data cube" (Tully 1974). A special technique allows the observational data to be reduced to a form where each image element has its own individual emission- (absorption-) line spectrum. The line-of-sight velocity field is then constructed from the Doppler shifts of the lines studied.

It is, however, often difficult to unambiguously reconstruct the rotation curve and analyze the direction of noncircular motions in the galaxy even if the full line-of-sight velocity field is available. Noncircular motions, which are primarily due to the spiral pattern, make it impossible to isolate the circular rotation component simply by averaging the total gas velocity field. Fourier analysis of the line-of-sight velocity field (Lyakhovich *et al.* 1997) allows the full spatial pattern of gas motions in a spiral galaxy to be reconstructed under certain assumptions about the nature of the spiral structure.

Barred galaxies exhibit noncircular motions of even larger amplitude. Although the interpretation of observed gas velocities in galaxy bars remains highly ambiguous, a number of important conclusions to be made about the motion pattern in the bar can be drawn by analyzing the gas rotation in terms of the circular-motion model. The bar produces a turn of the dynamical axis (i.e., the line of maximum line-of-sight velocity gradient) relative to the line of nodes (Chevalier and Furenlid 1978; Afanas'ev *et al.* 1992; Zasov and Moiseev 1999) and this turn can be determined using the

* E-mail address for contacts: moisav@sao.ru

well-known algorithms for the analysis of disk galaxy velocity fields.

The most comprehensive conclusions about the effect that the bar has on the galaxy disk can be drawn from numerous works on nonlinear computer simulations involving hydrodynamic equations written for "gas" consisting of macromolecules in the form of gas clouds. See (Lindblad 1996) for a review of various model simulations. The common result of these works is that they all find the bar to be an efficient mechanism for removing the angular momentum of the gas, thereby making the latter to partly move centerward along the bar and lose the energy at its shock edges (Athanassoula 1992a, 1992b; Levy *et al.* 1996). This motion pattern distorts the observed velocity contours, aligning them along the bar, whereas the dynamic axis, which is perpendicular to the velocity isolines it crosses, must, accordingly, turn in the opposite direction.

We must, nevertheless, bear in mind that the turn of the dynamic axis can also be caused by a tilted disk at the galaxy center (Zasov and Sil'chenko 1996; Zasov and Moiseev 1998). However, in this case, the dynamical axis of a circularly rotating disk coincides with the line of nodes and both the photometric and dynamic axes should therefore turn in the same direction. These are only qualitative considerations; therefore, concrete computations are needed, because the projection effect combined with radial gas flows in the bar can theoretically produce a pattern similar to that expected in the tilted disk case.

Extensive panoramic spectroscopy of HII velocity fields in spiral galaxies have been obtained with the Fabry-Perot interferometer attached to the 6-m BTA telescope of the Special Astrophysical Observatory of the Russian Academy of Sciences. It is very important, when interpreting these data, to analyze gas motions in the bars and identify eventual minibars (smaller than 1 kpc) from the dynamical manifestations they cause in the velocity field (see, e.g., Afanas'ev *et al.* 1989; Zasov and Sil'chenko 1996; Sil'chenko *et al.* 1997). To investigate whether the above patterns in the behavior of the mutual orientations of photometric and dynamical axes can in principle be applied to analyze observational data, it would be useful to consider the results of numerical velocity-field simulations with allowance for sky-plane projection effects and limited spatial and spectral resolution.

In this paper, we use the initial data, which are similar to the results of computations by Levy *et al.* (1996), to construct simulated HII velocity-field patterns similar to those actually observed in the Hα line with the standard Fabry-Perot attached to the BTA telescope [see Dodonov *et al.* (1995) for a detailed description of the instrument]. These data have a spatial resolution of (1.5–4) arcsec and a spectral resolution (50–150) km s^{-1} in velocity terms, with an accuracy of inferred line-of-sight velocities of (3–10) km s^{-1}.

2. CONSTRUCTING VELOCITY FIELDS

Our simulations are based on the numerical solution of hydrodynamics equations in an external gravitational field. The adopted gravitational potential model consists of a nonaxisymmetric perturbation superimposed on an axisymmetric component (bulge, disk, and halo) (see Matsuda *et al.* 1987).

The nonaxisymmetric perturbation (stellar bar mode) is turned on smoothly and gradually increased until it reaches the fixed level. The model exhibits a specific quasi-periodic regime of gas passage through the bar (Levy *et al.* 1994, 1996). Interestingly, the resulting flow pattern is bisymmetric—the gas flows centerward along the bar in two sectors, whereas in the other two sectors the flow direction is reversed; i.e., the gas flows away from the disk center due to the saddle point of the gravitational potential. As expected, the developing bar also produces a two-armed spiral pattern in the disk outside the corotation circle of the bar.

We used the results of simulations identical to those described in detail by Levy *et al.* (1996). The only difference was that we party adjusted the gravitational potential to closely reproduce the rotation curve of our Galaxy (Haud 1979). Our model had a maximum linear rotation velocity of 250 km s^{-1}; disk scale length of 3 kpc; radial bar scale length of ~1 kpc, and a radius of a simulated region 10 kpc. We further assumed that the galaxy is at a distance of 20.6 Mpc, where 1 arscec corresponds to 0.1 kpc, and has a systemic line-of-sight velocity (i.e., the center-of-mass velocity relative to the observer) of V_{sys} = 1545 km s^{-1}.

Our numerical simulations yielded the distributions of gas surface density $\sigma_{gas}(R, \varphi)$, radial ($V_R(R, \varphi)$ and azimuthal ($V_\varphi(R, \varphi)$) gas velocity components. Here, R and φ are the radial and azimuthal coordinates in the galactic plane, respectively. The polar grid cells had sizes of $\Delta\varphi = 2°$ in the azimuthal and $0.016 \le \Delta R \le 0.2$ kpc in the radial direction, depending on the galactocentric distance. Based on these data, we constructed model cubes using the following algorithm.

Line-of-sight velocity at point (R, φ):

$$V_{obs}(R, \varphi) = V_{sys} + V_R(R, \varphi)\sin\varphi\sin i + V_\varphi(R, \varphi)\cos\varphi\sin i, \quad (1)$$

where V_{sys} and i are the systemic line-of-sight velocity and the inclination of the galaxy plane to the sky plane, respectively. We set $\varphi = 0$ for the line of nodes.

We then projected distributions $V_{obs}(R, \varphi)$ and $\sigma_{gas}(R, \varphi)$ onto a Cartesian grid with a cell size of 0.02 kpc, assuming that the position angle of the line of nodes in the sky plane is $PA_0 = 90°$. As a result, we obtained the distributions of line-of-sight velocity and gas surface density distributions $V_{obs}(x, y)$ and $\sigma_{gas}(x, y)$, respectively. We fitted the emission-line spectrum at each point by a Gaussian centered on $V_{obs}(x, y)$ with a halfwidth of FWHM = 130 km s^{-1}, which approximately corresponds to the spectral resolution of the

Fabry-Perot spectrometer attached to the BTA telescope. When computing the total spectrum we neglected the velocity dispersion of individual gas clouds because of the coarse spectral resolution. We assumed that the spectral-line intensity is proportional to $\sigma_{gas}(x, y)$ and coarsened the spatial scale to the pixel size of 0.8 arcsec. The images in all spectral channels were Gaussian smoothed to make the resulting spatial resolution equal to 2 arcsec, which is close to the typical seeing value during real observations.

Based on the smoothed-cube spectra, we constructed the velocity field and the spectral-line image (the observed distribution of gas surface density) and determined the observed orientation parameters of the gaseous disk using the technique similar to that described by Begeman (1989). A similar algorithm is used in the well-known GIPSI radio astronomical data reduction software to analyze the observed velocity fields.

Below, we briefly describe the procedure used for the analysis.

Introduce polar coordinate system (r, PA) in the sky plane, where r and PA are the distance from the rotation center and position angle, respectively. The observed line-of-sight velocity V_{obs} in the case of purely circular rotation is

$$V_{obs}(r, \mathrm{PA}) = V_{sys} + V_{rot}(R(r))\frac{\cos(\mathrm{PA} - \mathrm{PA}_0)\sin i}{(1 + \sin^2(\mathrm{PA} - \mathrm{PA}_0)\tan^2 i)^{1/2}}, \quad (2)$$

and the distance from the rotation center in the galaxy plane is

$$R(r) = r(1 + \sin^2(\mathrm{PA} - \mathrm{PA}_0)\tan^2 i)^{1/2}, \quad (3)$$

where V_{rot} and PA_0 are the circular rotation velocity and position angle of the line of nodes, respectively.

During reduction, the observed velocity field is subdivided into elliptical rings defined by equation (3) for R = const. We then use the nonlinear least squares technique to fit model curve (2) to the observed dependence V_{obs}(PA). As a result, we obtain for each radius r the corresponding disk orientation parameters PA and i, and the circular rotation velocity V_{rot}.

Note that while the positions of the extrema of function (2) allow PA to be determined quite unambiguously, i estimates are much more uncertain. Thus, at small inclination angles i (in galaxies seen face-on), it is impossible to separate the contributions of V_{rot} and i to the observed velocity projection and only $V_{rot}\sin i$ can be unambiguously inferred. Begeman (1989) used a reduction of radio data to show the coupling of the two parameters at inclination angles $i < 40°$.

We constructed and analyzed simulated fields for various bar development stages and inclination angles ranging from 30° to 70°. We varied the angle between the line of nodes and the bar with a step of 15° and constructed a total of more than 400 simulated galaxies.

3. RESULTS AND ANALYSIS

In Fig. 1, we plot the gas surface-density distribution and line-of-sight velocity contours for various bar orientation angles. What is shown is a typical pattern for dimensionless time instants $T < 3$–4 (where $T = 1$ corresponds to one bar revolution). The bar then saturates and the spirals degenerate into a pseudo-ring [see Levy *et al.* (1996) for details]. The contour turns inside $r <$ (10–15) arcsec are caused by the bar, whereas at greater galactocentric distances they are determined by the motions in spiral arms. The typical S-shaped radial-velocity contours can be seen in the central region. It is interesting that the contours in question are distorted even if the bar is aligned along the major axis of the galaxy ($\phi = 0$, where ϕ is the angle between the major axis of the bar and the line of nodes measured in the galaxy plane). The line-of-sight velocity projection is formally equal to zero in this case; however, the bar has a finite width and velocity perturbations contain an azimuthal component, which also contributes to the radial velocity.

Figure 2 shows typical results for dynamical axis orientation for an inclination angle of $i = 70°$. Consider now the behavior of the position angle of the dynamical axis. At the very center of the galaxy, the dynamical axis always deviates significantly from the line of nodes $\mathrm{PA}_0 = 90°$ (except $\phi \approx 0°$ and –90° i.e., in the vicinity of the major and minor axes, respectively). Beginning with $r \approx 5$ arcsec, the angle between the two lines decreases and becomes negligible at $r \approx 10$ arcsec (in the vicinity of the bar tips). At greater galactocentric distances, the dynamical axis turns to the other side of the line of nodes and misalignment disappears only at $r > 20$ arcsec.

As the bar evolves, a shock develops at its leading edge and this shock is especially conspicuous in the pressure maps due to the strong gas in the region considered. Such an arrangement of shock fronts is consistent with both the observations of dust lanes in bars and with the results of earlier numerical simulations (Athanassoula 1992a, 1992b). The beat-frequency modulation about PA_0 is due to the complex velocity pattern at the bar tips, where the shock front moves from the leading bar edge to the inner edge of the trailing arms (because the corotation radius is $r \approx 20$ arcsec). The PA variation pattern is asymmetric with respect to $\phi = -90°$, because of a preferred direction of angle-counting determined by the pitch angle of the spiral density wave, whose direction is opposite to that of galactic rotation (trailing spiral).

The thick line in Fig. 2 shows the orientation of the sky-plane projection of the (the observed photometric) axis of the bar. It is evident from the figure that, in spite of the complex pattern of PA radial variation, the dynamical axis in the bar ($r < 10$ arcsec) always turns

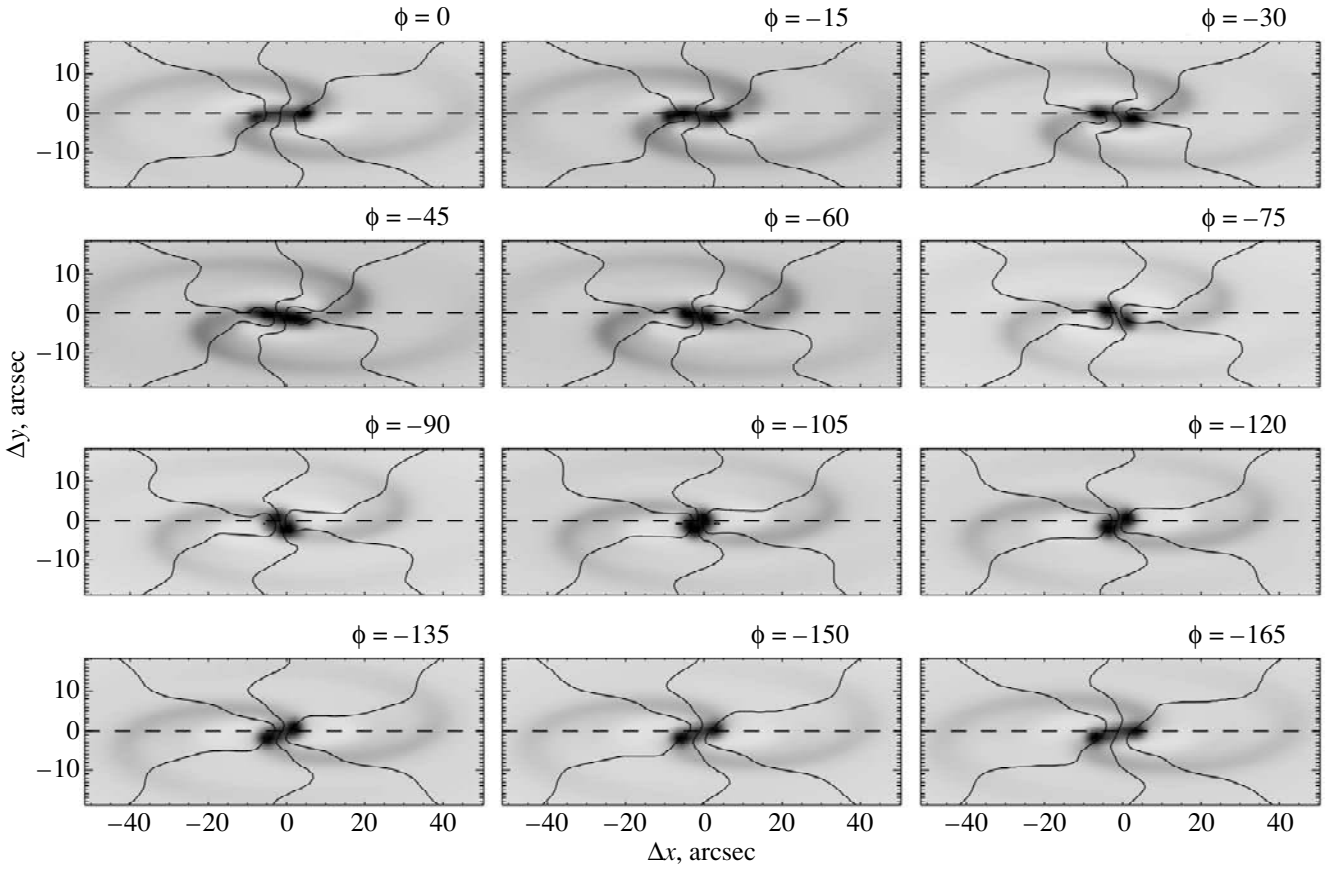

Fig. 1. Sky plane projection of the gas surface brightness in the central region for various bar turn angles ϕ (indicated at the top right corner in each graph) at time $T = 2.0$ since the start of the simulation. Contours show the V_{sys} and $V_{sys} \pm 100$ km s^{-1} line-of-sight isolines of model velocity field. The galaxy plane tilt is $i = 70°$; the dashed curve shows the line of nodes (position angle PA = 90°).

with respect to the photometric axis in the direction opposite that of the line of nodes: the two lines turn in antiphase. This conclusion applies to all simulated fields with different i, ϕ, and T.

In order to better illustrate this effect, we show in Fig. 3 how the deviations of the dynamical axis (averaged over all points with r (6 arcsec) depends on the bar orientation. In this figure, the amplitudes of the turn of the dynamical axis are somewhat smoothed by averaging; however, the overall trend remains conspicuous at all inclination angles and various bar development stages.

At ϕ angles ranging from 0° to ±45° (which correspond to PA ≈ ±(30°–45°) depending on the inclination angle i), the dynamical axis turns virtually in antiphase with the bar orientation. With a further increase of the angle between the bar and the line of nodes the dynamical axis begins to "lag behind"; its orientation changes slower than that of the photometric axis and it virtually coincides with the line of nodes at ϕ ≈ ±90°. However, the turn of the dynamical axis from the line of nodes is always in the sense opposite that of the bar axis. The "lag" of the dynamical axis is a result of a combined effect of projection and the evident fact that the bar fails to stop the gas rotation completely (the maximum bar contrast in our experiment was 30%), and there is always an azimuthal component besides the radial motions.

We now analyze the behavior of the tilt angle i formally inferred from the velocity field (Fig. 2). Radial motions in the bar region distort relation (2), which should have been observed if the rotation is purely circular. Therefore the inclination inferred at these radii can differ substantially from the true inclination of the disk. The variations of i can have amplitudes as high as 20°–30° and are often rather chaotic. However, the following pattern can be observed: for galaxy inclinations $i \geq 60°$–70°, the formally inferred inclination in the bar region becomes virtually constant at ϕ > –30° (ϕ < –150°). One gets a false impression that the galaxy center contains a decoupled disk whose inclination to the sky plane is 15°–25° smaller than that of the "outer" disk of the galaxy. The real angle between the disk planes can be as high as 90° (the polar disk).

The point is that, although at $i > 50°$–60°, the V_{obs} dependence on PA in formula (2) differs strongly from the cosine relation, radial motions whose projected velocities are maximum at the minor axis of the galaxy

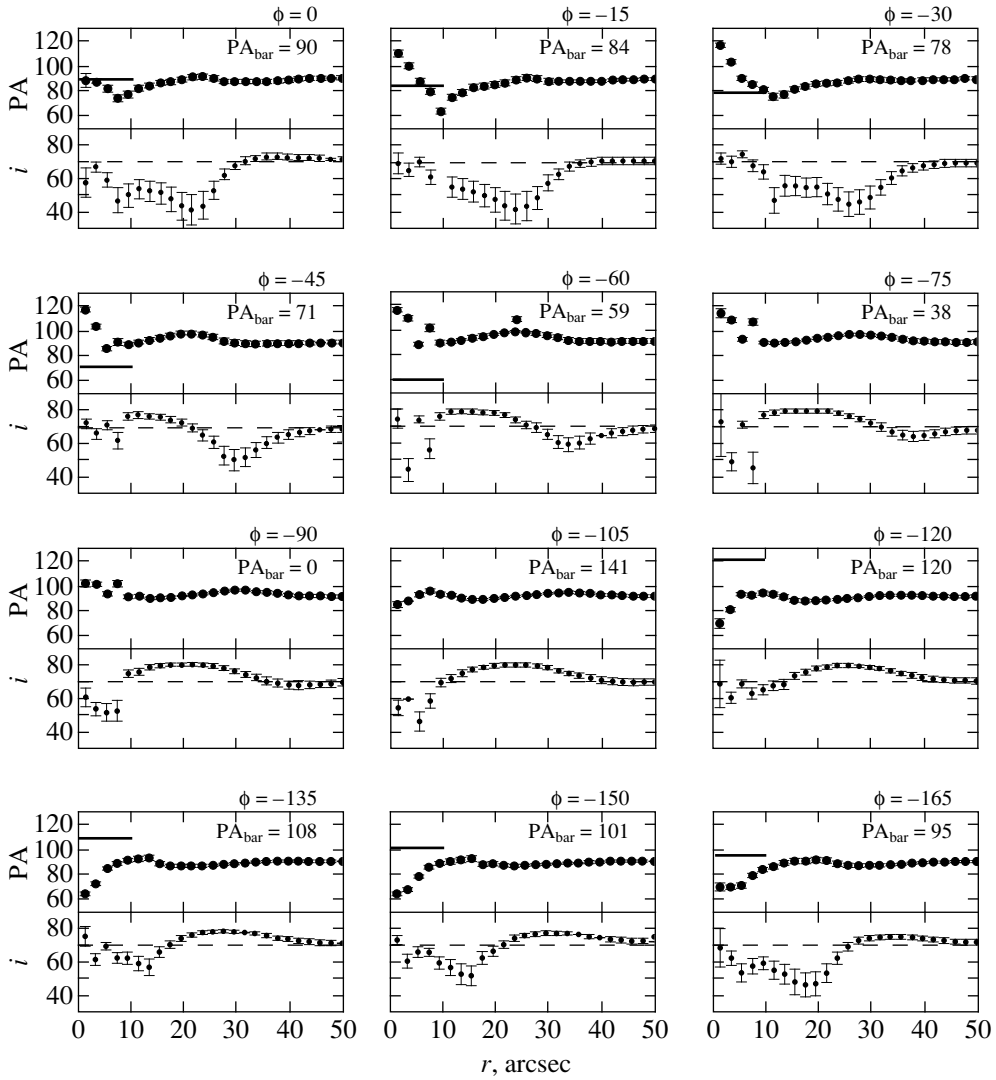

Fig. 2. Results for model velocity fields corresponding to various bar turn angles at time $T = 2$. Radial variations of the dynamical axis orientation PA and tilt angle i. Solid lines in PA plots show the position angle of the bar projected on the sky plane (indicated by "PA_{bar} = …" on each graph). Dashed lines in i plots show the galaxy plane tilt $i = 70°$.

distort the pattern implied by equation (2) making it more like a cosinusoid corresponding to smaller i. It is thus evident that restricting the analysis to surface photometry alone makes it rather difficult to distinguish a minibar from a nuclear polar disk; one may erroneously take the observed pattern for a manifestation of gas moving in curricular orbits with smaller inclination angles, whereas it might simply be a line-of-sight projection of a superposition of circular and noncircular motions in the bar. A turn of the dynamical axis should also be observed in the case of a real tilted (including polar) disk, and analyzing the velocity field alone can lead to wrong conclusions. Recall that in the tilted disk case, both the dynamical and photometric axes should turn in the same direction (Zasov and Moiseev 1999). A tilted disk can therefore be distinguished from a bar only by comparing the PA inferred from the velocity field analysis with the surface photometry data.

4. KINEMATICS OF GAS IN THE NGC 972 GALAXY

In order to illustrate our approach, we applied it to the NGC 972 galaxy. We observed this galaxy in the [NII]λ6583 line with the scanning Fabry-Perot interferometer attached to the 6-m BTA telescope of the Special Astrophysical Observatory of the Russian Academy of Sciences. The seeing and spectral resolution were ~1″.5 and ~50 km s^{-1}, respectively. We also modeled two velocity fields with different image orientations relative to the detector (Kvant two-dimensional photon counter). The results of the velocity-field analysis are briefly described by Zasov and Moiseev

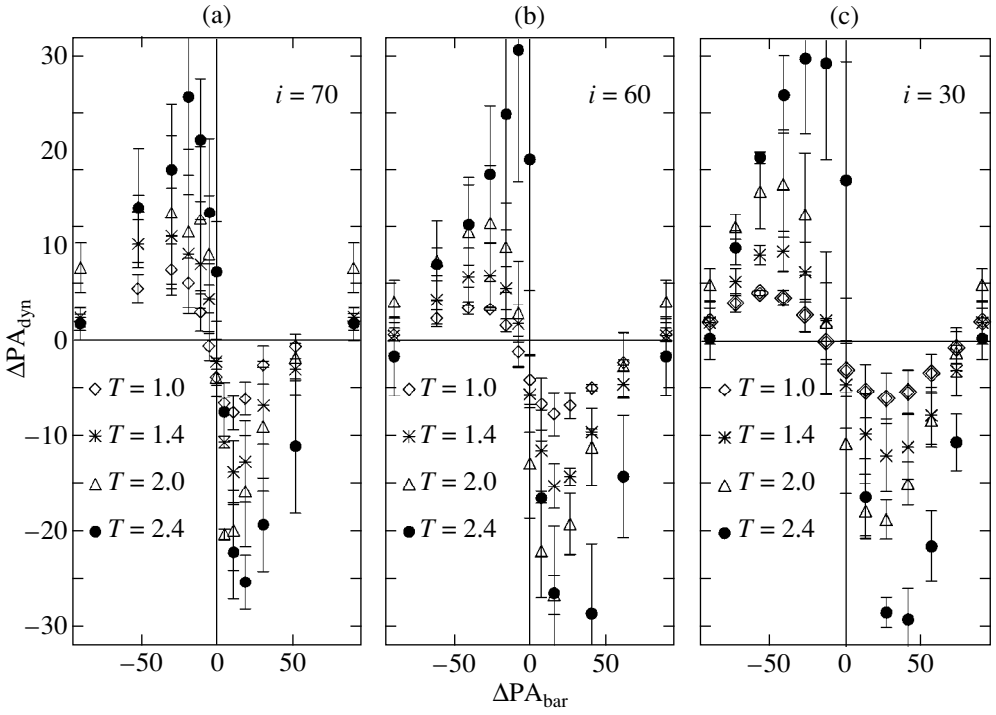

Fig. 3. Mean deviation of the position angle of the line of nodes in the bar region ΔPA_{dyn} plotted as a function of the bar position angle ΔPA_{bar} for various *i*. Different signs correspond to different dimensionless time instants *T*.

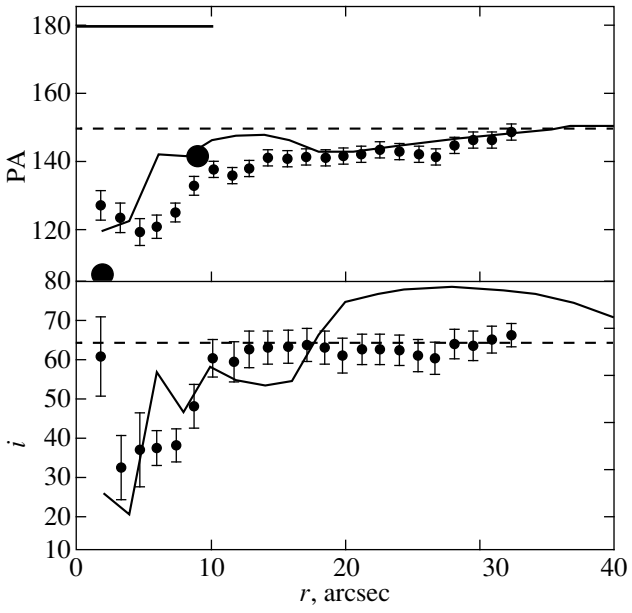

Fig. 4. Results of an analysis of the [NII] line velocity fields of the NGC 972 galaxy (black dots with error bars). Two large circles show the results of Zasov and Sil'chenko (1996). Above: radial variations of the dynamical axis orientation, thick interval shows the mean orientation of central *K*-band isophotes of NGC 972 (bar position). Below: gaseous disk tilts as inferred from velocity fields. Solid lines in each graph show model dependencies for the dimensionless time instant $T = 2.2$ and bar turn angle $\phi = 120°$.

(1999), and a more detailed paper is now in preparation. Figure 4 shows the radial profiles of the position angle of the dynamical axis (PA) and inclination angle *i* formally inferred from the velocity field in terms of the circular rotation approximation as described in Section 2. Dots are mean values averaged over both velocity fields. Filled circles show the position angles taken from Zasov and Sil'chenko (1996).

The mean inclinationt of the galaxy to the line of sight is $i \approx 64°$; the position angle of the line of nodes, PA = 150°, in agreement with the orientation of the outermost *K*-band isophotes (2.2 μm) based on observations taken at the UKIRT infrared telescope (Hawaii). The abrupt change of PA and *i* at $r < 10$ arcsec can be interpreted in terms of both inclined disk or minibar models.

However, comparing the turns of the dynamic axis with the *K*-band isophote orientation allows this ambiguity to be resolved. The black line segment in Fig. 4 indicates the mean orientation in the central isophotes of the galaxy, i.e., the position of the photometric axis. It is evident from the figure that the orientation of the photometric axis (relative to the line of nodes) varies in "antiphase" with that of the dynamical axis, a pattern that is indicative of a ~10 arcsec (1 kpc) bar whose axis makes an angle of $\phi \approx -120°$ to the line of nodes. Variations of angle *i* in this case are due to noncircular motions in the bar, as noted above in Section 3.

We constructed model velocity fields with orientation parameters equal to those of the NGC 972 disk for various time instants T corresponding to a gradual increase of the contrast of the gravitational potential of the bar (Levy *et al.* 1996). Solid lines in Fig. 4 show the results for the model velocity field at $T = 2.2$. Note that the observed plots agree well with the computed ones given the fact that, strictly speaking, the mass distribution in NGC 972 differs from that of the adopted model.

5. CONCLUSION

Our analysis of model velocity fields constructed from numerical nonlinear two-dimensional simulations of gas flows in bars showed that, if the galaxy plane is inclined by more than $i > 60°$–$70°$ to the sky plane, the observed distribution of gas line-of-sight velocities in the bar region can create an illusion of a "tilted nuclear disk," implying a wrong interpretation of the observed velocity field.

However, in the case of a bar, the dynamical axis always turns with respect to the line of nodes in antiphase with the photometric axis, thereby allowing the bar to be distinguished from a tilted disk by a combined analysis of the kinematics and photometry.

We illustrated the use of this criterion by applying it to the NGC 972 galaxy.

ACKNOWLEDGMENTS

We are grateful to A.V. Zasov for calling our attention to the problem and providing velocity fields of NGC 972 obtained in the framework of his BTA observing program. We are also grateful to O.K. Sil'chenko for her critical comments, interest in our work, and primary reduction of observational material. The image of the NGC 972 galaxy was provided by S. Rider. We thank the staff members of the SFVO laboratory (Special Astronomical Observatory, Russian Academy of Sciences) who performed all observations at the BTA telescope. Special thanks are due to V.L. Afanas'ev for his constructive criticism and valuable suggestions. The work was partly supported by the Russian Foundation for Basic Research (grant no. 98-02-17102) and INTAS (grant no. 95-0988).

REFERENCES

1. V. L. Afanas'ev, A. N. Burenkov, A. V. Zasov, and O. K. Sil'chenko, Astron. Zh. **69**, 19 (1992) [Sov. Astron. **36**, 10 (1992)].
2. V. L. Afanasiev, O. K. Sil'chenko, and A. V. Zasov, Astron. Astrophys. **213**, L9 (1989).
3. E. Athanassoula, Mon. Not. R. Astron. Soc. **259**, 328 (1992a).
4. E. Athanassoula, Mon. Not. R. Astron. Soc. **259**, 345 (1992b).
5. K. G. Begeman, Astron. Astrophys. **223**, 47 (1989).
6. R. A. Chevalier and I. Furenlid, Astrophys. J. **225**, 67 (1978).
7. S. N. Dodonov, V. V. Vlasyuk, and S. V. Drabek, *Fabry–Perot Interferometer: User's Guide* (Nizhniĭ Arkhyz, 1995).
8. U. A. Haud, Pis'ma Astron. Zh. **5**, 124 (1979) [Sov. Astron. Lett. **5**, 68 (1979)].
9. V. V. Levy, V. V. Mustsevoĭ, and V. A. Sergienko, in *Physics of the Gaseous and Stellar Disks of the Galaxy*, Ed. by R. King, Astron. Soc. Pac. Conf. Ser. **66**, 93 (1994).
10. V. V. Levy, V. V. Mustsevoĭ, and V. A. Sergienko, Astron. Astrophys. Trans. **11**, 1 (1996).
11. P. A. B. Lindblad, *Gas Dynamics in Barred Spiral Galaxies*, Ph. D. Thesis (Stockholm Univ., Stockholm, 1996).
12. V. V. Lyakhovich, A. M. Fridman, O. V. Khoruzhiĭ, and A. I. Pavlov, Astron. Zh. **74**, 509 (1997) [Astron. Rep. **41**, 447 (1997)].
13. T. Matsuda, M. Inaoue, K. Sawada, *et al.*, Mon. Not. R. Astron. Soc. **229**, 295 (1987).
14. R. B. Tully, Astrophys. J., Suppl. Ser. **27**, 415 (1974).
15. O. K. Sil'chenko, A. V. Zasov, A. N. Burenkov, and J. Boulesteix, Astron. Astrophys., Suppl. Ser. **121**, 1 (1997).
16. A. V. Zasov, in *The Physics of Galaxies* (Mosk. Gos. Univ., Moscow, 1993), p. 62.
17. A. V. Zasov and A.V. Moiseev, in *Proceedings of the 194th IAU Symposium on Activity in Galaxies and Related Phenomena, 1999*, Ed. by Y. Terzian, E. Khachikian, and D. Weedman, p. 279; astro-ph/9812121.
18. A. V. Zasov and O. K. Sil'chenko, Astron. Soc. Pac. Conf. Ser. **91**, 207 (1996).

Translated by A. Dambis

Astronomy Letters, Vol. 26, No. 9, 2000, pp. 572–581. Translated from Pis'ma v Astronomicheskiĭ Zhurnal, Vol. 26, No. 9, 2000, pp. 665–675.
Original Russian Text Copyright © 2000 by Zabrodina, Imshennik.

A Hydrodynamic Model for Asymmetric Weak Explosion of Collapsing Supernovae with Rapid Initial Rotation

E. A. Zabrodina and V. S. Imshennik*

Institute of Theoretical and Experimental Physics, Bol'shaya Cheremushkinskaya ul. 25, Moscow, 117259 Russia

Received December 27, 1999

Abstract—We further investigate the two-dimensional hydrodynamic explosion model for rapidly rotating and collapsing supernovae (Aksenov *et al.* 1997), in which the initial energy release inside a fragmenting low-mass neutron star of critical mass $\approx 0.1 M_\odot$ moving in a circular orbit at a velocity of ≈18 000 km s^{-1} is reduced considerably. This velocity closely corresponds to a pulsar escape velocity of ≈1000 km s^{-1} (at a total mass of $\approx 1.9 M_\odot$ for the binary of neutron stars). Compared to our previous study (Zabrodina and Imshennik 1999), this energy release was reduced by more than a half. Otherwise, the model in question does not differ from the explosion model with a self-consistent chemical composition of nuclides investigated in the above paper. In particular, the initial energy release was carefully reconciled with a chemical composition. Our numerical solution shows that the reduction in energy release due to the time scales of β processes and neutrino energy losses being finite does not alter the qualitative results of our previous studies (Aksenov *et al.* 1997; Imshennik and Zabrodina 1999). An intense undamped diverging shock wave (with a total post-shock energy $\gtrsim 10^{51}$ erg at a front radius of ≈10 000 km) is formed; a large asymmetry of explosion with a narrow cone (with a solid angle of $\approx \pi/4$) around the leading direction, which coincides with the velocity direction of the low-mass neutron star at the instant of its explosive fragmentation in the two-dimensional model, emerges. A jet of synthesized radioactive nickel, whose mass is estimated by using simple threshold criteria to be $M_{\mathrm{Ni}} \approx (0.02\text{–}0.03) M_\odot$, is concentrated inside this cone. This appears to be the integrated parameter that is most sensitive to the specified reduction in initial energy release; it is also reduced by almost a half compared to our previous estimate (Imshennik and Zabrodina 1999). The time of propagation of the shock wave inferred in our model to the presupernova surface was estimated for SN 1987A to be 0.5–1.0 h, in agreement with observations. © *2000 MAIK "Nauka/Interperiodica".*

Key words: *supernovae and supernova remnants; neutron stars, hydrodynamics and shock waves*

1. Here, we continue to consider the rotational explosion mechanism for collapsing supernovae (SNe), but with a considerable reduction in the initial internal energy assumed for the explosive fragmentation of a low-mass neutron star (NS), exactly by half compared to that adopted by Aksenov *et al.* (1997) in their hydrodynamic modeling of asymmetric explosion. This initial internal energy is also approximately a factor of 2 lower than the value specified in our previous study (Imshennik and Zabrodina 1999) (below referred to as IZ), in which we analyzed the effect of iron dissociation–recombination on the hydrodynamic pattern of asymmetric explosion in terms of the universal equation of state (Imshennik and Nadyozhin 1965, 1982). Given iron dissociation–recombination, the equivalent reduction in this parameter must clearly be even larger if the self-consistent mass fraction of iron is less than unity at the initial instant. The above internal energy turns out (see below) to be $\varepsilon_0 = 0.38 \times 10^{51}$ erg instead of $\varepsilon_0 = 0.90 \times 10^{51}$ erg (Aksenov *et al.* 1997). The value of ε_0 is then almost equal to the initial kinetic energy of an exploding low-mass NS (with a critical mass of $0.1 M_\odot$), $W_0 = 0.322 \times 10^{51}$ erg, which closely corresponds to the pulsar (a more massive NS of mass $1.8 M_\odot$) escape velocity of 1000 km s^{-1} assumed by Aksenov *et al.* (1997). Using the equation of state from IZ, we show below the following through hydrodynamic modeling: (1) the explosion shock wave (SW) propagating through the outer region of the collapsing iron core of a ($\sim 0.1 M_\odot$) star has a total energy of $\sim 10^{51}$ erg behind its front and outside the explosion remnants of the low-mass NS that is enough for a typical SN; and (2) the explosion SW is characterized by an appreciable asymmetry with the leading direction that coincides in the two-dimensional approximation used here (Aksenov *et al.* 1997) with the direction of motion of the low-mass NS at the instant of its explosive fragmentation. Thus, the corresponding conclusions from IZ do not change qualitatively. The same is also true for the conclusions by Aksenov *et al.* (1997), but quantitative differences naturally increase in this comparison.

The reduction in initial internal energy is dictated by the series of studies by Colpi *et al.* (1989, 1991, 1993)

* E-mail address for contacts: imshennik@vxitep.itep.ru

and the recent study by Sumiyoshi *et al.* (1998), who took into account the finite time scales of β processes and neutrino energy losses when considering the explosive fragmentation of a low-mass NS. Note that they differed in this from the hydrodynamic model by Blinnikov *et al.* (1990) with a simple equation of state for catalyzed nuclear matter; the above initial internal energy $\varepsilon_0 = 0.90 \times 10^{51}$ erg obtained in the latter model was most likely overestimated because of the rough description of weak interactions. The effects of reduced energy release have already been discussed previously (Aksenov *et al.* 1997; IZ), but here we present a quantitative model of weak explosion. Of course, it would be of interest to reduce the energy release to the limit, to zero (Sumiyoshi *et al.* 1998), but this reduction would result in the violation of validity conditions for the adopted equation of state, because the initial temperature in the region of energy release would be even lower than the well-known critical value of $(3–5) \times 10^9$ K from the outset.

The problem of a weak explosion is numerically solved by the Lagrangian method (LM) with the parameters from IZ. See also Aksenov *et al.* (1997) for the essence and advantages of the LM method (Godunov *et al.* 1976) over the well-known PPM method (Collela and Woodward 1984; Collela and Glaz 1985) as applied to the problem in question. The entire solution region was broken up into two tiers: the region of energy release (tier 1) and the outer region bounded by the shock front and the contact boundary with the region of energy release (tier 2).

2. Let us first consider the problem of initial internal energy ε_0 in terms of specific internal energy e_0. For a simple equation of state (an ideal, completely ionized iron gas plus blackbody radiation) and in accordance with the model by Blinnikov *et al.* (1990) mentioned above, $e_0 = E_0 = 4.5 \times 10^{18}$ erg g^{-1} = 4.7 MeV/nucleon. According to the adopted universal equation of state, which takes into account free nucleons (p, n) and helium (^{4}He) and iron (^{56}Fe) nuclides for the baryonic component, as well as Fermi–Dirac electron–positron gas together with blackbody radiation (IZ), part of the internal energy is contained in the rest energy of the nuclides if the iron mass fraction is not unity. Let this part of the internal energy in the sum with specific internal energy e_0 account for a fraction ξ of E_0. In the notation of IZ, we then have the following relation between e_0 and E_0:

$$\frac{Q_{\rm Fe} + 26\Delta Q_n}{56m_u}(1 - X_{0\,\rm Fe}) - \frac{Q_{\rm He} + 2\Delta Q_n}{4m_u}X_{0\,\rm He} - \frac{\Delta Q_n}{m_u}X_{0\,p} + e_0 = \xi E_0, \quad (1)$$

where Q_i is the binding energy of the ith nuclides in their ground state, and X_{0i} are the mass fractions of these nuclides. The quantity $\Delta Q_n = (m_n - m_p)c^2$ is the energy threshold for β decay of a neutron. Substituting $Q_{\rm Fe}$ = 492.3 MeV, $Q_{\rm He}$ = 28.30 MeV, and ΔQ_n = 1.294 MeV (Wapstra 1958), as well as E_0 = 4.670 MeV/nucleon in relation (1) yields the dimensionless coefficient $\alpha = e_0/E_0$,

$$\alpha = \xi - 2.012(1 - X_{0\rm Fe}) + 1.654X_{0\rm He} + 0.2771X_{0p}. \quad (2)$$

Under the model assumption of uniform structure for the region of energy release at the initial instant in time $t = 0$ (Aksenov *et al.* 1997), we derive the dependence $\alpha = \alpha(\xi)$ by solving Eq. (2) together with the adopted equation of state by iterations. For the two values ξ = 1.0 and 0.5 of interest, this solution is given in the table[1]. Our case of a weak explosion corresponds to ξ = 0.5. The sought-for α decreases with decreasing ξ, but appreciably more slowly by a factor of a mere 1.66; this is natural, because the store of energy in the form of rest energy decreases with decreasing ξ (by contrast, the mass fraction $X_{0\rm Fe}$ increases).

The data in the table suggest that some inaccuracy has crept into IZ. Indeed, a self-consistent solution for ξ = 1 yields the initial internal energy $\varepsilon_0 = 0.63 \times 10^{51}$ erg (see table) for the explosion of a low-mass neutron star rather than $\varepsilon_0 = \varepsilon_{02} = 0.675 \times 10^{51}$ erg, as specified in our previous study (see Table 1 from IZ); i.e., the latter value turned out to be overestimated by ~7%. It can be noted in this connection that, unfortunately, the auxiliary formulas (10) and (11) from IZ proved to be inaccurate. It would be more appropriate to use the following obvious approximate relation instead of these formulas (in general, $\xi \le 1$):

$$\tilde{\alpha}_{\rm eff} = \xi[0.75 + 0.25X_{0\rm Fe} - 0.25(X_{0\rm He} + X_{0n})] \simeq (0.50 + 0.50X_{0\rm Fe})\xi, \quad (3)$$

if we disregard the proton mass fraction, according to the table. We will then actually obtain $\tilde{\alpha}_{\rm eff}$ very close to α from the table: $\tilde{\alpha}_{\rm eff}$ = 0.69 at $X_{0\rm Fe}$ = 0.38 (ξ = 1.0) and $\tilde{\alpha}_{\rm eff}$ = 0.46 at $X_{0\rm Fe}$ = 0.83 (ξ = 0.5). As a matter of fact, we already stipulated in IZ [immediately after the erroneous inequality (11)] that ε_{02} could be overestimated, but this correct stipulation was not realized in the form of a negative term in the preceding formula (10). This term just appears in (3) here.

Nevertheless, the inaccuracy committed in determining the initial value of ε_0 does not serve as a reason for a new calculation with the correct $\varepsilon_0 \approx 0.63 \times 10^{51}$ erg, because the hydrodynamic pattern of explosion depends only slightly on ξ [or $\alpha(\xi)$]. This can be verified by considering ξ = 0.5, whose solution is presented below. Incidentally, using relation (2), we can determine precisely what final energy release corresponded to our main calculation in IZ. Indeed, by specifying α = 0.750 in (2), which corresponds to $\varepsilon_{02} = 0.675 \times 10^{51}$ erg, and the chemical composition from Table 1 in IZ

[1] Unfortunately, since slightly different nuclear constants Q_i appeared in the derivation of (2) and in the equation of state, α and ε_0 are given in the table only to within the second decimal place.

Table

Quantities	Initial parameter	
	$\xi = 1.0$	$\xi = 0.5$
$\varepsilon_0(10^{51}$ erg)	0.63	0.38
$e_0(6.09 \times 10^{-17}$ erg g^{-1})	5.16	3.10
$T_0(4.17 \times 10^9$ K)	2.13	1.87
$P_0(2.29 \times 10^{24}$ erg cm^{-3})	163	128
α	0.70	0.42
$X_{0\mathrm{Fe}}$	0.385	0.834
$X_{0\mathrm{He}}$	0.566	0.153
X_{0n}	4.65×10^{-2}	1.22×10^{-2}
X_{0p}	2.58×10^{-3}	3.90×10^{-4}

($X_{0\mathrm{Fe}} = 0.302$, $X_{0\mathrm{He}} = 0.642$, $X_{0p} = 3.14 \times 10^{-3}$), we obtain $\xi = 1.09$ and the corresponding $\varepsilon_0 = 0.98 \times 10^{51}$ erg. Consequently, the final internal energy (after complete iron recombination) $\varepsilon_0 = 0.45 \times 10^{51}$ erg taken here for weak explosion is lower than its previous value by a factor of 2.2.

3. The only difference in the initial conditions and in the statement of the problem under consideration between this study and IZ is as follows: the specific internal energy is specified in dimensional units, $e_0 = 1.9 \times 10^{18}$ erg g^{-1} = 2.0 MeV/nucleon, which is taken to be constant within a sphere of uniform density $\rho_0 = 5.66 \times 10^8$ g cm^{-3} with the outer radius $R_0 = 4.38 \times 10^7$ cm $= 0.1R_{\mathrm{Fe}}$. The remaining thermodynamic quantities (T_0 and P_0) are given in the table ($\xi = 0.5$) together with the corresponding mass fractions of the nuclides ($X_{0\mathrm{Fe}}$, $X_{0\mathrm{He}}$, X_{0n}, X_{0p}). Of course, they all result from the specified e_0 and ρ_0 (the latter does not differ from the previous ρ_0), according to the adopted universal equation of state. The dimensional identical initial velocity along the z axis is $v_{0z} = 18\,000$ km s^{-1}; i.e., it closely matches the velocity specified previously (Aksenov *et al.* 1997; IZ).

The results of our calculation, which continued up to the dimensionless instant in time $t = 1.53486$ ($[t] = 0.561$ s) with 2183 steps (in time), are presented for some characteristic dimensionless instant in time $t = 0.7695$. The choice of this instant is characteristic from the viewpoint of comparison with our previous calculations. According to Aksenov *et al.* (1997) (see Figs. 5 and 8), it is at this instant that the shock front in the lagging direction, which coincides with the negative z direction ($z < 0$), reached the radius of the initial iron core, $z_{\mathrm{SW}}^{\min} \simeq -1.0R_{\mathrm{Fe}}$, where $R_{\mathrm{Fe}} = 4.38 \times 10^8$ cm; thus, the entire, nearly spherical shock front went outside the iron core. Strictly speaking, for a detailed comparison with our previous calculations, it is better to borrow the results from them obtained by the LM method, because this method with the same difference grid is also used here. For this reason, there were no references above to the figures constructed by the PPM method. However, the above figures also give $z_{\mathrm{SW}}^{\min} \simeq -1.0R_{\mathrm{Fe}}$, at the same instant in time, while $z_{\mathrm{SW}}^{\max} \simeq +2.8R_{\mathrm{Fe}}$ for the leading direction, according to both LM and PPM methods.

Figures 1–5 show a full hydrodynamic pattern of motion of the explosion remnants (tier 1) and of the surrounding matter behind the shock front (tier 2) at the above dimensionless instant in time $t = 0.7695$ ($t = 0.43$ s in dimensional units). We see that the shock front is actually nearly spherical with the center near $z_{\mathrm{SW}}^{(\mathrm{c})} \simeq 1.0R_{\mathrm{Fe}}$ and with two extrema: $z_{\mathrm{SW}}^{\max} \simeq 2.5R_{\mathrm{Fe}}$ (the leading direction $z > 0$) and $z_{\mathrm{SW}}^{\min} \simeq -0.5R_{\mathrm{Fe}}$ (the lagging direction $z < 0$). Thus, the principal distinction of weak explosion is not only a considerable lag of the shock front at $z < 0$, but also some lag in the leading direction $z > 0$. Curiously enough, the symmetry centers of the shock front virtually coincide, $z_{\mathrm{SW}}^{(\mathrm{c})} \simeq 1.0R_{\mathrm{Fe}}$; the center of initial energy release was located at $z^{(\mathrm{c})} = 0.16R_{\mathrm{Fe}}$ (Aksenov *et al.* 1997). However, the above authors used a simple equation of state in which the important processes of iron dissociation–recombination and the Fermi–Dirac statistical properties of electrons were disregarded.

In reality, allowance for these effects has already yielded a reduction in the propagation velocity of the shock front, despite a small (~7%) overestimate of the initial internal energy (see above). As suggested by Figs. 4 and 10 from IZ, $z_{\mathrm{SW}}^{\max} \simeq 2.6R_{\mathrm{Fe}}$ and $z_{\mathrm{SW}}^{\min} \simeq -0.7R_{\mathrm{Fe}}$ were obtained at the close dimensionless instant in time $t = 0.76956$. Thus, the effect of passage to a new equation of state is clear enough: it resulted in a general deceleration of the shock front with a certain tendency for a more noticeable lag precisely in the lagging direction $z < 0$. Remarkably, the symmetry center displaced only slightly when passing to a new equation of state, $z_{\mathrm{SW}}^{(\mathrm{c})} \simeq 1.0R_{\mathrm{Fe}}$. Roughly speaking, such qualitatively different factors as a refinement of the equation of state with allowance for significant departures from a Boltzmann ideal gas and a reduction in the initial internal energy of the explosion by half caused approximately the same reduction in the propagation velocities of the shock front, ~10%, as can be easily estimated. Finally, note that the degree of asymmetry $z_{\mathrm{SW}}^{\max} / \left| z_{\mathrm{SW}}^{\min} \right|$ assumed in our previous studies increases appreciably, to 5.0, compared to our previous estimates of 2.8 and 3.7. These estimates naturally reflect a predominant effect in the lagging direction. The above qualitative conclusions do not change at other instants in time.

4. Let us next consider some more results shown in Figs. 1–5, which, in our view, are of interest. Figure 3 shows that the iron recombination in tier 1 has virtually ended, while the initial dissociation of iron in tier 2 has long given way to its recombination. Lines of constant iron mass fraction in both tiers are also shown in IZ (Fig. 10). Interestingly, there are strict inequalities,

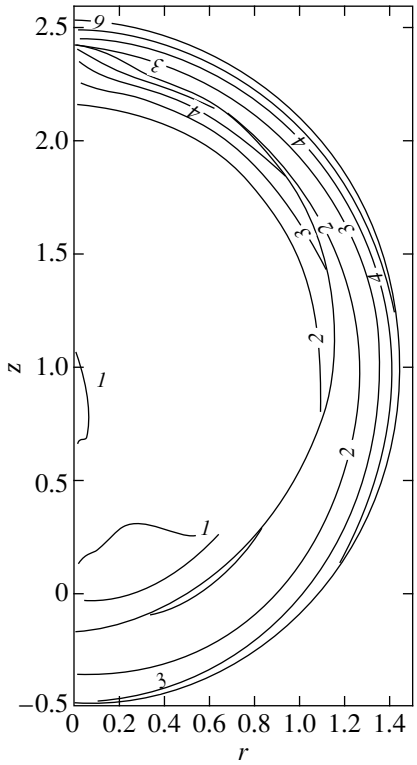

No.	Tier 1	Tier 2
1	0.011	0.040
2	0.192	0.201
3	0.381	0.370
4	0.571	0.539
5	0.761	0.708
6	0.941	0.869
Min	0.002	0.032
Max	0.951	0.877

Fig. 1. Lines of constant dimensionless density ρ as a function of r and z coordinates for a weak explosion and for the instant in time $t = 0.7695$ in units of $[r] = [z] = 4.38 \times 10^8$ cm, $[t] = 0.561$ s, $[\rho] = 3.77 \times 10^6$ g cm^{-3}. These lines, which are denoted by numbers (where possible) in the figure, are identified in the table. In contrast to the lines of constant density, both highlighted boundaries (the shock front and the contact boundary of tiers 1 and 2) reach the z axis.

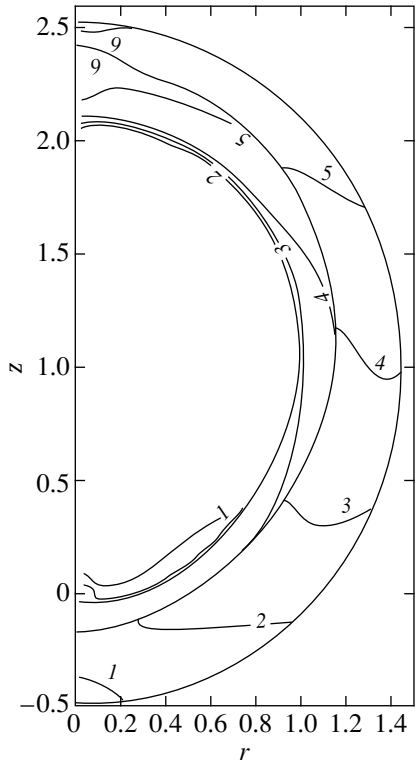

No.	Tier 1	Tier 2
1	0.1064	0.2126
2	0.2265	0.3280
3	0.3530	0.4496
4	0.4795	0.5712
5	0.6060	0.6927
6	0.7262	0.8082
Min	0.1000	0.2065
Max	0.7325	0.8143

Fig. 2. Same as Fig. 1 for the dimensionless temperature T. The unit of temperature is $[T] = 4.17 \times 10^9$ K.

$X_{\mathrm{Fe1}}^{(\mathrm{IZ})} < X_{\mathrm{Fe1}}^{(\mathrm{ZI})}$ and $X_{\mathrm{Fe2}}^{(\mathrm{IZ})} > X_{\mathrm{Fe2}}^{(\mathrm{ZI})}$, where numbers 1 and 2 in the subscripts denote the tier number, and the superscripts distinguish our previous study (IZ) from this one (ZI). These inequalities are derived in distant decimal places as if implying that, during a weak explosion, the recombination is "stronger" in tier 1, while the dissociation is "stronger" in tier 2. These differences can hardly be attributed to the effect of a slightly later instant in time from IZ (see above), because the recombination in tier 1 increases with time. Such natural subtle differences in the calculations of X_{Fe} may point to a high accuracy of the entire calculation.

Figure 4 shows isobars at the selected instant in time. We see that, by contrast to the isotherms in Fig. 2 with a nearly radial direction in tier 2, the isobars here are nearly parallel to the shock front and the contact boundary. This implies that the pressure gradient is more likely directed radially than parallel to the shock front. By contrast, the temperature gradient is closer to the longitudinal direction in tier 2. In all probability, the behavior of the pressure is more strongly affected by the direction of the density gradients, which, according to Fig. 1, is also almost radial. Of course, the pressure and density gradients are directed inward, in accordance with the general situation of shock-front deceleration with time. In general, the pressure gradients are oriented in such a way that any noticeable mass flow behind the shock front from the leading direction to the lagging one cannot develop in tier 2. This absence of tangential flow is clearly seen in Fig. 5, where the vector velocity field is shown at the characteristic dimensionless instant in time $t = 0.7695$ under consideration. The arrows of the velocity vectors are mostly directed along the radius drawn from the geometric center of a

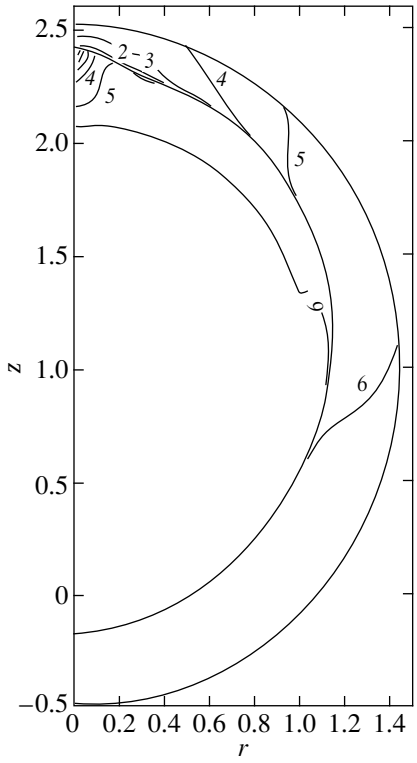

No.	Tier 1	Tier 2
1	0.9998534	0.998914
2	0.9998815	0.999123
3	0.9999112	0.999342
4	0.9999407	0.999561
5	0.9999703	0.999781
6	0.9999985	0.999989
Min	0.9998519	0.998904
Max	0.9999999	1.000000

Fig. 3. Same as Fig. 1 for the iron mass fraction X_{Fe}.

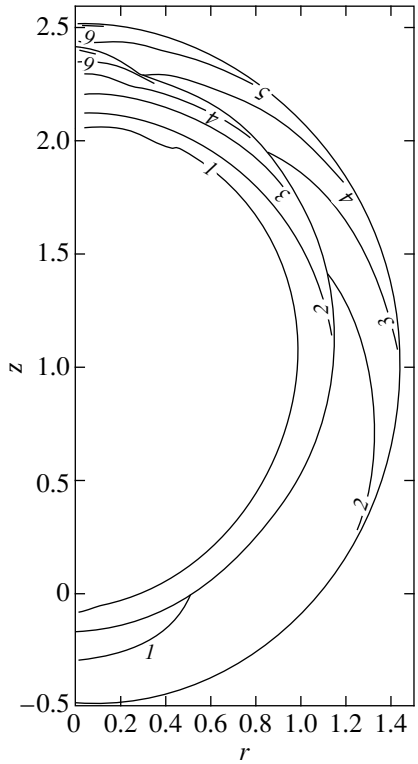

No.	Tier 1	Tier 2
1	0.0029	0.0106
2	0.0572	0.0865
3	0.1142	0.1664
4	0.1713	0.2464
5	0.2284	0.3263
6	0.2826	0.4022
Min	0.0001	0.0066
Max	0.2855	0.4062

Fig. 4. Same as Fig. 1 for the dimensionless pressure *P*. The unit of pressure is $[P] = 2.29 \times 10^{24}$ erg cm^{-3}.

spherical shock front, i.e., from the point with $r_c = 0$ and $z_c \simeq 1.0R_{\mathrm{Fe}}$. It is of interest to note the enormous difference between these velocities in tier 2 (Fig. 5): from the maximum $v_z^{\max} \simeq 1.26 \times 10^9$ cm s^{-1} to the minimum $v_z^{\min} \simeq -2.34 \times 10^7$ cm s^{-1}, for the leading and lagging directions, respectively. The contact boundary between the tiers in the lagging direction even turns back. The pattern of velocities in tier 1 is very complex with intense mass flow in the leasing direction.

Finally, Figs. 1–5 show that virtually no Rayleigh–Taylor instability develops near the contact boundary of both tiers. However, this kind of instability begins to show up at later instants in time, particularly in a sector around the leading direction with a characteristic wavelength of $\sim 0.5R_{\mathrm{Fe}}$. At the dimensionless instant in time $t = 1.53486$ $z_{\mathrm{SW}}^{\max} \simeq 3.6R_{\mathrm{Fe}}$, and $z_{\mathrm{SW}}^{\min} = -0.9R_{\mathrm{Fe}}$, while the shock front differs markedly in shape from a sphere with a sharp protrusion in the leading direction. The difference grid does not withstand such deformation, and the calculation soon stops.

5. Let us next make an attempt to roughly estimate the time of propagation of the shock front to the very presupernova (PSN) surface in the specific case of SN 1987A, whose presupernova radius is known to be $R_{\mathrm{PSN}} \simeq 40.2R_\odot$ (Imshennik and Popov 1992). By the end of our calculation, the shock front had already penetrated deep into the CO envelope of the PSN, whose radius may be taken from Deputovich and Nadyozhin (1999), $R_{\mathrm{CO}} \simeq 3 \times 10^9$ cm: $R_{\mathrm{SW}} \simeq z_{\mathrm{SW}}^{\max} \simeq 1.5 \times 10^9$ cm for the last dimensional instant in time $t = 0.86$ s (see above). Therefore, the preshock gas density can already decrease by approximately an order of magnitude (see above). The propagation velocity of the shock front apparently could not then have dropped, as was the case at constant density in our calculation: as is easy to find, the mean velocity between the characteristic instant in

time $t = 0.43$ s and the instant at which the calculation terminates was 1.1×10^9 cm s^{-1}. At the same time, the instantaneous shock-front velocity D^*_{SW} can be estimated at the characteristic instant $t = 0.43$ s. According to Fig. 1, the degree of gas compression within the hemisphere around the leading direction is ~5, so $D^*_{SW} \simeq (5/4)\, v_z^{max} \simeq 1.5 \times 10^9$ cm s^{-1}, because the dimensionless gas velocity in Fig. 5 is 1.62. If we disregard the calculated shock-front deceleration and take $D^*_{SW} = 1.5 \times 10^9$ cm s^{-1} as the effective shock velocity, then we can determine the total time of propagation of the shock front to the PSN 1987A surface in the roughest approximation of constant shock-front velocity:

$$t^{tot}_{SW} = \frac{R_{PSN}}{D^*_{SW}} \simeq \frac{40.2 R_\odot}{D^*_{SW}} \simeq 1.9 \times 10^3 \text{ s} \simeq 31 \text{ min}. \quad (4)$$

This value is consistent with direct hydrodynamic calculations of this important parameter of SN explosion, which can be a lower limit of the time interval between the "instant" of the neutrino signal from the collapsing supernova and the onset of its optical explosion immediately after the shock front emerges on the PSN surface. By definition, the instant of powerful energy release coincides with the shock formation, but, in general, it can occur later than the "instant" of collapse, when the neutrino signal is generated.

In the rotational explosion mechanism for collapsing SNe, this signal corresponds to the collapse of a more massive NS, which got rid of its significant intrinsic rotation slightly earlier. The latter assertion is based on the neutrino-signal theory for SN 1987A developed by Imshennik and Nadyozhin (1988), which is consistent with observations precisely in the absence of rotation. In principle, the "instant" of explosion of a low-mass NS does not necessarily match the instant at which a more massive NS gets rid of its intrinsic rotation. Imshennik (1992) argues for an earlier instant (within ~1 h) at which a more massive NS gets rid of its intrinsic rotation, but both these instants can also be almost equal (Imshennik and Popov 1998). The term "instant" implies that these processes actually proceed in a certain finite time interval $\lesssim 10$ s.

It is desirable to refine the estimate (4), for example, by using an approximate formula from Klimishin and Gnatyk (1981) for the velocity of the shock front propagating through a sequence of PSN envelopes: Si; O, C; He; He, H. The accuracy of this simple formula was analyzed by Deputovich and Nadyozhin (1999), though for a specific example of a PSN with the structure of a red supergiant, which is inapplicable to PSN 1987A[2].

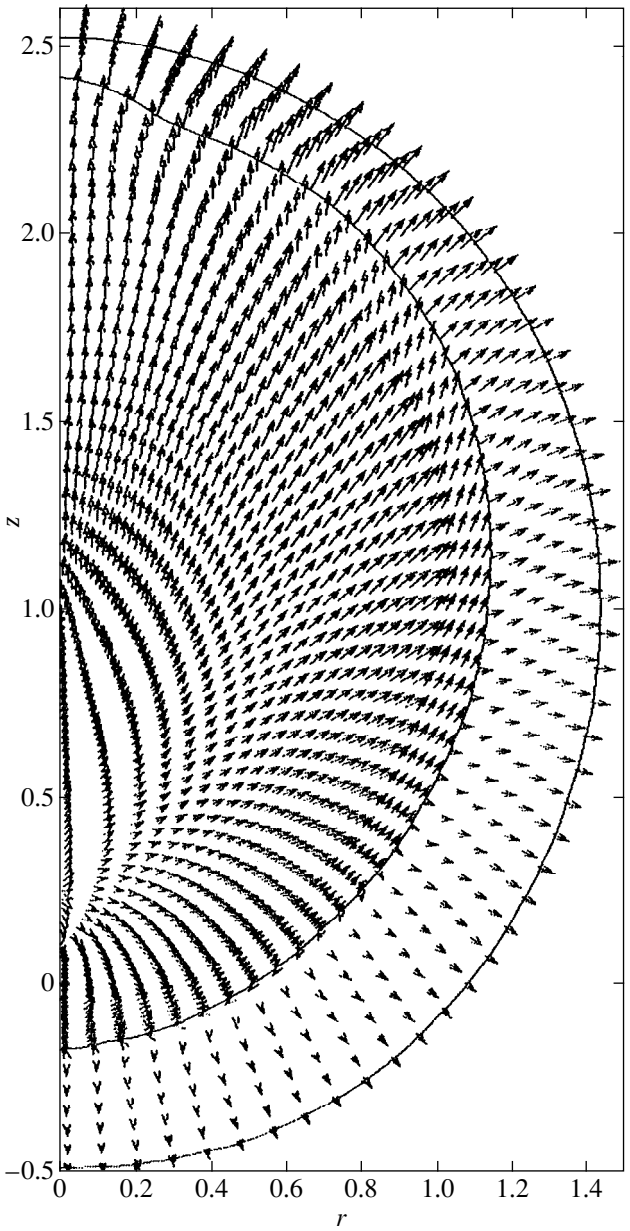

No.	Tier 1	Tier 2
Min	0.03	0.03
Max	2.52	1.62

Fig. 5. The field of dimensionless velocities v as a function of r and z coordinates for a weak explosion and for the same instant in time as in Figs. 1–4. The unit of velocity is $[v] = 7.79 \times 10^8$ cm s^{-1}. The length of the arrows in vectors v is proportional to the magnitude of the velocity. The minimum and maximum velocities for the entire field are identified in the table.

However, the mass of this PSN was approximately equal to the known mass of PSN 1987A, which most likely implies that the parameters of all envelopes in both stars, except the outermost He, H one, are similar.

[2] The structure of a red supergiant was determined through the evolutionary calculation of a $15.08 M_\odot$ PSN by Woosley and Weaver (1995) as a typical progenitor of SNe II. PSN 1987A is known to belong to atypical compact PSNe and was identified with the blue supergiant Sk–69°202 in the LMC.

Thus, we have an approximation of D_{SW} in the case of its deceleration (Klimishin and Gnatyk 1981),

$$D_{SW} = C_d(\rho_0 R_{SW}^3)^{-1/2}. \quad (5)$$

If we substitute $D_{SW}^* = 1.5 \times 10^9$ cm s^{-1} in (5), then we obtain the constant C_d from our calculation with $R_{SW} > R_{Fe} = 4.38 \times 10^8$ cm at the specified density $\rho_0 = 5.66 \times 10^5$ g cm^{-3} (for the Si and/or C, O envelopes):

$$C_d = 4.16 \times 10^{25} \text{ cm g}^{1/2}/\text{s}. \quad (6)$$

The distribution of density $\rho_0 = \rho_0(R_{SW})$ in the outer part of the He, H envelope for PSN 1987A was approximately determined by Imshennik and Nadyozhin (1988) (with $M = 18M_\odot$, $L = 1.3 \times 10^5 L_\odot$, $\kappa = 0.34$, $\mu = 0.62$; see the same paper for the notation):

$$\rho_0 = 1.095 \times 10^{-4}\left(\frac{R_0}{R_{SW}} - 1\right)^3 \text{ g/cm}^3, \quad (7)$$

where $R_0 = 47R_\odot = 3.27 \times 10^{12}$ cm is the PSN radius. Substituting this distribution in (5) yields the shock-front velocity

$$D_{SW} = 0.672 \times 10^9\left(1 - \frac{R_{SW}}{R_0}\right)^{-3/2} \text{ cm/s}, \quad (8)$$

which is certainly applicable in the range $1 \geq \frac{R_{SW}}{R_0} \geq 0.4$. In particular, from (8) at $R_{SW} = 0.4R_0 = 1.31 \times 10^{12}$ cm, we obtain $D_{SW} = 1.33 \times 10^9$ cm s^{-1}, a value that is virtually equal to the initial D_{SW}^* near the stellar center. The time of propagation of the shock front over the above range of R_{SW}/R_0 can also be easily calculated by integration:

$$t_{SW} = 543 \text{ s} \simeq 9 \text{ min}.$$

For a slightly different, apparently optimal set of parameters for PSN 1987A (Imshennik and Popov 1992): $M = 17M_\odot$, $L = 1.3 \times 10^5 L_\odot$, $\kappa = 0.266$, $\mu = 0.62$, and $R_0 = 40.2R_0$, we obtain from (8) after integration a similar value,

$$t'_{SW} = 507 \text{ s} \simeq 8.5 \text{ min},$$

although the corresponding density ρ_0 (7) has almost doubled here. If, however, we formally extend the validity range of formula (8) to the outer radius of the He envelope (Deputovich and Nadyozhin 1999), $R_{SW}/R_0 \simeq 0.02$, then we obtain the total time it takes for the shock front to pass through the He, H envelope of PSN 1987A,

$$t_{SW}^* = 1730 \text{ s} \simeq 29 \text{ min}.$$

The time of propagation of the shock front through the inner envelopes of PSN 1987A for $R_{SW} < 0.4R_0$ (for t_{SW} and t'_{SW}) and $R_{SW} < 0.02R_0$ (for t_{SW}^*) should also be added to all t_{SW}, t'_{SW}, and t_{SW}^*. If, in addition, we assume the propagation velocity of the shock front there to be constant with the initial velocity $D_{SW}^* = 1.5 \times 10^9$ cm s^{-1} [see Deputovich and Nadyozhin (1999) for a qualitative justification of this assumption], then we obtain the following estimates in the same sequence:

$$t_{SW}^\Sigma = 24 \text{ min}, \; t_{SW}^{'\Sigma} = 20 \text{ min}, \; t_{SW}^{*\Sigma} = 30 \text{ min}. \quad (9)$$

In short, under all assumptions, the sought-for time (9) is about half an hour, which differs only slightly from the initial rough estimate $t_{SW}^{tot} = 31$ min (4).

The above estimates (9) most likely have the meaning of lower limits for the following reasons: first, we implied the validity of the sector approximation for the shock-front propagation in the leading direction, which may result in the velocity being slightly overestimated in this direction; and, second, when testing formula (5) in the He, H envelope, Deputovich and Nadyozhin (1999) found the reflected shock wave accompanying the acceleration of the diverging shock front as it enters the He, H envelope to emerge near its boundary (from the inside); strictly speaking, this would imply the replacement of (5) by a different formula, which was also derived by Klimishin and Gnatyk (1981) with a more modest increase of the shock-front velocity in the He, H envelope than that given by formula (8). We therefore propose to take $t_{SW} = 0.5$–1.0 h as the final estimate for the time of propagation of the shock front in our calculation, which is consistent with observations of SN 1987A (given the above remark on the interpretation of the neutrino signal).

6. In IZ, we estimated the mass of the ^{56}Ni synthesized behind the shock front after it enters the PSN envelopes surrounding the stellar iron core. This was a threshold estimate; $T_{th} = [T] = 4.17 \times 10^9$ K falling within the well-known theoretical range of critical temperatures in which the approximation of nuclear statistical equilibrium (NSE) is valid was chosen as the temperature threshold ($T > T_{th}$). For a weak explosion, this estimate yields the following nickel masses:

$$M_{Ni} = 0.0185M_\odot(r \geq R_{Fe}),$$
$$M'_{Ni} = 0.0277M_\odot(r \geq 0.54R_{Fe}), \quad (10)$$

where some of the designations from our previous paper are used. The radii r of the shells of the Si envelope in which radioactive nickel—the most bound nuclide among the iron-peak α-particle nuclides (^{56}Ni)—is synthesized even in a short hydrodynamic time after the NSE conditions are established (see above) are given in parentheses. These radii are limited below by the radius of the inner boundary of the Si envelope, which generally can decrease when the collapsed PSN iron core fills up. Thus, a spatial threshold for the region of nickel synthesis is added to the above temperature threshold. The second estimate M'_{Ni} in

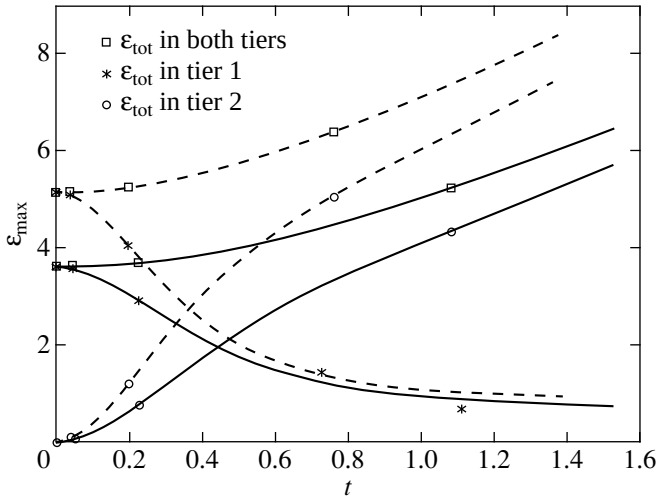

Fig. 6. Dimensionless total energy ε_{tot} (for both tiers separately and the total ε_{tot}) versus dimensionless time t for a weak explosion (solid lines). For comparison, the dashed lines indicate the corresponding plots for energy ε_{tot} from the main case of IZ. The units of energy and time are $[\varepsilon_{tot}] = 1.94 \times 10^{50}$ erg and $[t] = 0.561$ s. The energies are given without allowance for the rest energy in nuclides and the constant rest energy of electrons.

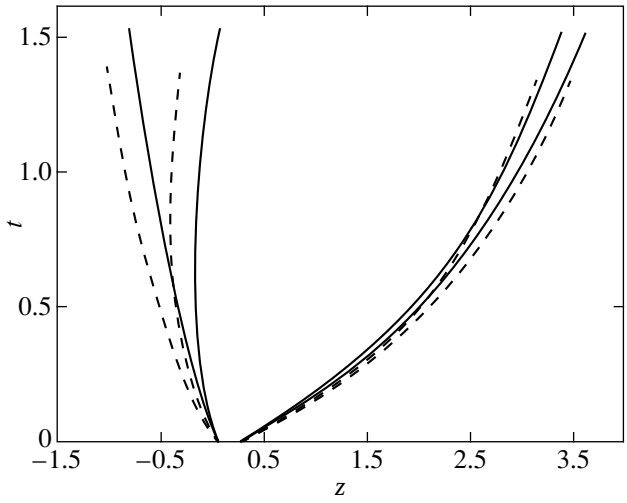

Fig. 7. z–t diagrams for the shock front and the contact boundary of tiers 1 and 2 for a weak explosion (solid lines). For comparison, the dashed lines indicate the corresponding z–t diagrams from the main case of IZ. The diagrams for the contact boundaries naturally lag behind the diagrams for the adjacent shock fronts. The initial diameters of the region of energy release ($t = 0$), equal to 0.2 with its center at $z_c = 0.16$, are seen to be the same. The units of z coordinate and time t are the same as those in Fig. 1.

(10) assumes that the inner boundary r of the Si envelope can approach the stellar center in a relatively long lifetime of a NS binary (~1 h), according to the arguments given previously (IZ). Our threshold estimates (10) show a reduction in the nickel mass approximately by half, with nickel being synthesized here in an even narrower solid angle around the leading direction ($<\pi/4$) with an opening angle $<\pi/3$. The calculated masses of nickel are appreciably lower than its observed mass of $0.075M_\odot$ in SN 1987A, being very sensitive to the explosion energy release, which is natural by the meaning of the threshold criteria used.

In general, other integrated explosion parameters are less sensitive to the initial conditions, as suggested by Figs. 6 and 7. These figures show a plot of total energy ε_{tot} against time t and diagrams of the shock front and the contact boundary also versus time t, respectively. It should be immediately emphasized that ε_{tot} in Fig. 6 does not include the rest energy of the nuclides and electrons, being only the sum of the internal energy of thermal motion of the particles and photons ε_{int} and the kinetic energy of the gas. It is this parameter for $t = 0$ that appears in the first row of the table as $\varepsilon_{int} = \varepsilon_0$ at $m_{ns} = 0.1M_\odot$. The z–t diagrams in Fig. 7 evidently have the meaning of sections of the shock-front surface and the contact boundary by the z axis. Note that, in the dimensionless units of Fig. 6, the characteristic energy for SN explosions (10^{51} erg) is 5.15, so ε_{tot} exceeds this value by the end of our calculation in both compared cases. The total energy ε_{tot} exceeds 5.15 even in tier 2 (Fig. 6). We see in the same figure that the difference between ε_{tot} by the end of both calculations exceeds their difference specified in the initial conditions: $\Delta\varepsilon_{tot} \simeq 2.4$, i.e., 0.47×10^{51} erg, for the dimensionless time $t = 1.4$ (instead of 0.30×10^{51} erg at $t = 0$). It can be shown that this difference is mainly attributable to the conversion of the nuclide rest energy during complete iron recombination into the energy ε_{tot} under consideration. The store of energy for a weak explosion is approximately a factor of 3 smaller than its previously calculated value (~0.1×10^{51} erg compared to ~0.3×10^{51} erg). By the end of our calculations, the absolute values of ε_{tot} gain a further significant increase through the energy of a completely degenerate preshock iron gas, ~0.4×10^{51} erg, almost the same in both calculations[3].

The z–t diagrams in Fig. 7 differ by a lag of both lines of weak explosion in the lagging direction ($z < 0$) for all t, but the contact boundary of weak explosion in the leading direction ($z > 0$) leads the corresponding line of the previous case starting from some instant in time ($t \gtrsim 0.5$ s). Note that, in Fig. 12 from IZ, no such effect arose when compared with the previous case of a simplified equation of state from the calculations by Aksenov *et al.* (1997). Here, it is clearly associated with the development of Rayleigh–Taylor instability, which is most pronounced in the leading direction (see above). Nevertheless, in general, the z–t diagrams in Fig. 7 differ relatively little from each other, with the differences in the leading direction being particularly small. The same circumstance was emphasized in IZ.

[3] In IZ, this energy was erroneously overestimated by a factor of 1.5.

Thus, Figs. 6 and 7 show that, qualitatively, the hydrodynamic pattern of weak explosion differs only slightly from the pattern of explosion when the final total energy release in the form of internal energy increases by a factor of 2.2 (the ratio of ξ equal to 1.09 and 0.5, respectively).

7. Thus, the formation of a diverging shock wave with a total post-shock energy of about 10^{51} erg is also confirmed for a weak explosion of a low-mass NS. The explosion weakening is simulated by a factor of ~1.8 reduction in the initial internal energy compared to our previous calculation (IZ), in which it was 0.675×10^{51} erg. In both calculations, we used the universal equation of state, which allows us to describe self-consistent iron dissociation–recombination in the NSE approximation justified *post factum* in our calculations. It should be noted once again that this ratio became even larger, by a factor of ~2.2, after complete iron recombination, i.e., after the store of the rest energy converted into thermal internal energy, because the initial self-consistent iron mass fraction in a weak explosion was found to be 0.834 instead of 0.302, as was in the calculation of a strong explosion. The considerable reduction in energy release is intended in part to compensate for its possible overestimation by Blinnikov *et al.* (1990), which we took as a basis from the beginning of this series of calculations (Aksenov *et al.* 1997). Indeed, having simulated the explosive fragmentation of a low-mass NS that reached its critical mass of $\sim 0.1 M_\odot$ with allowance for the finite times of β interactions and neutrino radiation, the authors of other studies (Colpi *et al.* 1989, 1991, 1993; Sumiyoshi *et al.* 1998) obtained a considerable reduction in energy release, although the fact of NS explosive expansion was confirmed (Sumiyoshi *et al.* 1998). The explosive fragmentation of a low-mass NS apparently needs further investigation with an improvement of both the physical statement of the problem and of the numerical method. For now, in our view, it makes sense to simulate the subsequent asymmetric explosion of a low-mass NS by a considerable reduction in initial energy release and then to compare such a calculation with previous calculations performed by the same numerical LM algorithm, which proved to be reliable up to large radii of shock propagation, ~10 000 km. Our numerical solution of an axially symmetric problem presented here, where we took the direction of the velocity vector for a low-mass NS at the time of its explosion as the symmetry axis (see Aksenov *et al.* (1997) and IZ for a justification of the two-dimensional approximation for the essentially three-dimensional hydrodynamic problem of explosion), clearly shows that the hydrodynamic pattern of explosion is only slightly sensitive to the initial internal energy. In addition, for a weak explosion, we obtained here a plausible estimate for the time of propagation of the shock wave (with the parameters from this calculation) to the presupernova surface in the specific case of SN 1987A, 0.5–1.0 h, in agreement with the observed difference between the times of the neutrino signal and the initial explosion. The main result of our previous calculations for a large asymmetry of the shock front, to which the asymmetry in the synthesis of radioactive nickel is closely related, was also obtained for a weak explosion even with some increase in the degree of asymmetry. Note that the most important physical processes of iron dissociation–recombination have already been analyzed previously (Imshennik 1998) for a strong explosion; in the above paper, we firmly concluded that their role in the hydrodynamic pattern of an asymmetric explosion is minor. In the present calculation, this role is even smaller because of the reduction in characteristic gas temperatures.

At present, all potentialities of the two-dimensional approximation appear to have been almost exhausted, and performing simulations in the full three-dimensional statement of the problem with allowance for the gravitational interaction with a more massive NS (or a black hole) is of current interest[4]. Previous estimates and auxiliary calculations testify that the main conclusions (about an intense diverging shock wave and about characteristics of the explosion asymmetry) mentioned above must also hold in the full three-dimensional calculation. Nevertheless, a full justification of the energetics of the diverging shock wave (the total energy is $\sim 10^{51}$ erg in these calculations) is primarily needed in the three-dimensional simulation of explosion.

ACKNOWLEDGMENTS

We wish to thank A.V. Zabrodina for the interest in this study and for providing a multiprocessor computer at the Institute of Applied Mathematics (Russian Academy of Sciences) and D.K. Nadyozhin for helpful discussions. We are grateful to N.A. Vulikh for help in preparing the article. This study was supported by the International Science and Technology Center (project no. 370-97) and, in part, by the Russian Foundation for Basic Research (project no. 96-15-96465).

REFERENCES

1. A. G. Aksenov, E. A. Zabrodina, V. S. Imshennik, and D. K. Nadyozhin, Pis'ma Astron. Zh. **23**, 779 (1997) [Astron. Lett. **23**, 677 (1997)].
2. S. I. Blinnikov, V. S. Imshennik, D. K. Nadyozhin, *et al.*, Astron. Zh. **67**, 1181 (1990) [Sov. Astron. **34**, 595 (1990)].

[4] As before, we deal with hydrodynamic simulations of an asymmetric explosion without regard for β processes and neutrino radiation, which, as was already noted in our previous papers, cannot play a significant role at relatively low characteristic gas densities. This is shown, in particular, by an analysis of the equation of state in question (Imshennik and Nadyozhin 1965), in which the effect of weak interactions was taken into account, though in the rough approximation of catalyzed matter. For the same reason, there is little point in including the initial explosive fragmentation of a low-mass NS in the assumed three-dimensional model, because a consistent allowance for weak interactions is just important in it.

3. P. Collela and H. M. Glaz, J. Comput. Phys. **59**, 264 (1985).
4. P. Collela and P. R. Woodward, J. Comput. Phys. **54**, 174 (1984).
5. M. Colpi, S. L. Shapiro, and S. Teukolsky, Astrophys. J. **339**, 318 (1989).
6. M. Colpi, S. L. Shapiro, and S. Teukolsky, Astrophys. J. **369**, 422 (1991).
7. M. Colpi, S. L. Shapiro, and S. Teukolsky, Astrophys. J. **414**, 717 (1993).
8. A. Yu. Deputovich and D. K. Nadyozhin, Pis'ma Astron. Zh. **25**, 750 (1999) [Astron. Lett. **25**, 649 (1999)].
9. S. K. Godunov, A. V. Zabrodin, M. Ya. Ivanov, *et al.*, *Numerical Solution of Multi-Dimensional Gas-Dynamical Problems* (Nauka, Moscow, 1976).
10. V. S. Imshennik, Pis'ma Astron. Zh. **18**, 489 (1992) [Sov. Astron. Lett. **18**, 194 (1992)].
11. V. S. Imshennik, in *Modern Problems of Stellar Evolution*, Ed. by D.S. Wiebe (Geos, Moscow, 1998), p. 163.
12. V. S. Imshennik and D. K. Nadyozhin, Astron. Zh. **42**, 1154 (1965) [Sov. Astron. **9**, 896 (1965)].
13. V. S. Imshennik and D. K. Nadyozhin, Itogi Nauki Tekh., Ser. Astron. **21**, 63 (1982).
14. V. S. Imshennik and D. K. Nadyozhin, Usp. Fiz. Nauk **156**, 561 (1988).
15. V. S. Imshennik and D. V. Popov, Astron. Zh. **69**, 497 (1992) [Sov. Astron. **36**, 251 (1992)].
16. V. S. Imshennik and D. V. Popov, Pis'ma Astron. Zh. **20**, 620 (1994) [Astron. Lett. **20**, 529 (1994)].
17. V. S. Imshennik and D. V. Popov, Pis'ma Astron. Zh. **24**, 251 (1998) [Astron. Lett. **24**, 206 (1998)].
18. V. S. Imshennik and E. A. Zabrodina, Pis'ma Astron. Zh. **25**, 123 (1999) [Astron. Lett. **25**, 93 (1999)].
19. I. A. Klimishin and B. I. Gnatyk, Astrophys. **17**, 306 (1981).
20. K. Sumiyoshi, H. Suzuki, W. Hillebrandt, and S. Yamada, Astron. Astrophys. **334**, 159 (1998).
21. A. N. Wapstra, *Hand. der Physik* (Springer, Berlin, 1958), Vol. 38/1.
22. S. E. Woosley and T. A. Weaver, Astrophys. J., Suppl. Ser. **101**, 181 (1995).

Translated by V. Astakhov

Astronomy Letters, Vol. 26, No. 9, 2000, pp. 582–588. Translated from Pis'ma v Astronomicheskiĭ Zhurnal, Vol. 26, No. 9, 2000, pp. 676–682.
Original Russian Text Copyright © 2000 by Grasberg.

Shock Waves with Large Energy Losses by Direct Radiation from the Front

E. K. Grasberg*

Institute of Astronomy, University of Latvia, Raina bulv. 19, Riga, LV 1586 Latvia

Received December 23, 1999

Abstract—Highly nonadiabatic shock waves are formed at an early stage of a supernova explosion inside a stellar wind because of the large energy losses by direct radiation from the front. The properties of such waves are considered for velocities of $(5–25) \times 10^3$ km s^{-1} and gas densities of 10^{-17}–10^{-10} g cm^{-3}. A critical energy flux going to "infinity" that separates two modes is shown to exist. If the flux is lower than the critical one, then energy losses cause even an increase in the post-shock temperature. An excess of the flux over its critical value results in an abrupt cooling and in a strong compression of the gas. For the flux equal to the critical one, the post-shock gas velocity matches the isothermal speed of sound. Approximate formulas are given for estimating the degree of gas compression and the post-shock radiation-to-gas pressure ratio at energy losses equal to the critical ones and for the limiting compression. © *2000 MAIK "Nauka/Interperiodica".*

Key words: *plasma astrophysics, hydrodynamics, shock waves*

INTRODUCTION

During supernova (SN) explosions, when a strong shock wave (SW) emerges on the stellar surface, it begins to intensely lose its energy through radiation "to infinity." The energy losses are so large that the SW becomes highly nonadiabatic, and its parameters differ greatly from those of classical SWs. In particular, as numerous model calculations of SN explosions show, the gas compression in such a SW can exceed the limiting compression for an adiabatic SW by several orders of magnitude.

Such large radiative energy losses are not typical of conditions when the photon mean free path $l_r \ll L$, where L is the size of the region in which the SW propagates. In large-amplitude waves, radiation can play a crucial role in forming the shock-front structure. A heating zone is formed ahead of the viscous discontinuity, which essentially determines the SW front width. However, the radiation going to infinity is generated in a relatively narrow region near the front edge of the heating zone (Zel'dovich and Raizer 1966; Klimishin 1984). The effective temperature of the outgoing radiation $T_{\rm eff}$, which characterizes the energy losses, is determined by absorptive properties of the gas and is much lower than the temperature behind the viscous discontinuity for large-amplitudes SWs (Zel'dovich and Raizer 1966). Relatively small energy losses affect only slightly the integrated SW parameters—the degree of compression and the post-shock temperature. When a strong SW emerges on the presupernova surface, the optical depth of all the gas ahead of the discontinuity up to infinity turns out to be smaller than the optical depth of the front $\Delta\tau_{\rm SW}$ typical of such a SW (with the same velocity and the same gas density, but for $l_r \ll L$).

A strong gas compression in a nonadiabatic SW is accompanied by the raking of the matter in the presupernova upper layers to produce a dense raked-up layer behind the front (Grasberg *et al.* 1971; Falk and Arnett 1977; Chevalier and Klein 1979; Blinnikov and Bartunov 1993). As model calculations show, this layer proves to be optically thick, with true absorption dominating in it. This effect is especially pronounced in the case of an extended and tenuous presupernova atmosphere, which is typical of most Type II SNe with a plateau in their light curves. Many SNe of this type are surrounded by an envelope of the gas lost by the star in the form of stellar wind at late evolutionary stages. If the wind is sufficiently dense, then the forward-going radiation can produce a heating zone in the stellar-wind matter. In a stationary wind, $\rho_{\rm w} \propto r^{-2}$, and the inequality $\tau_\infty < \Delta\tau_{\rm SW}$ is only strengthened and can even be $\tau_\infty \ll 1$. Thus, if the wind density is low, then no heating zone is actually formed, and much of the radiation generated in the SW goes to infinity. At the initial stage, after the SW emerges in the stellar wind, the pattern remains as before: an optically thick zone exists behind the SW, the raking of gas into a thin layer continues, and the SW itself remains highly nonadiabatic. At this stage, the SN luminosity can be determined by direct radiation from the shock front (Grasberg and Nadyozhin 1987; Grasberg 1994). The duration of this stage is relatively

* E-mail address for contacts: egras@latnet.lv

short, because the raked-up layer becomes transparent through expansion and cooling, and the energy losses acquire a different, three-dimensional pattern. The entire pattern of motion asymptotically passes to a mode that is well described by the self-similar solutions of Nadyozhin (1981, 1985) and Chevalier (1982).

Here, our goal is to ascertain the basic properties of highly nonadiabatic SWs under the conditions described above without resorting to complex calculations.

STATEMENT OF THE PROBLEM

In our case, the highly nonadiabatic SWs are generally nonstationary. In the first approach, we apply the approximation of "instantaneous quasi-stationarity." Without aiming at studying the SW structure, but investigating only its integrated parameters, we consider it as a discontinuity on which Hugoniot's conditions are satisfied. We "include" the entire front structure into the discontinuity, whose optical depth may be large. We assume that an optically thick region (corresponding to the raked-up layer) exists behind the discontinuity, in which the gas and the radiation are in equilibrium and there is no radiation flux. A transparent region with $\tau_\infty < 1$ lies ahead of the discontinuity, and the radiation freely escapes from it. The flux density of the energy emitted to infinity is F_∞. Denote the quantities ahead of and behind the discontinuity by the subscripts "0" and "1," respectively. Hugoniot's conditions in the frame of the shock front can then be written as (Imshennik 1975)

$$\rho_1 u_1 = \rho_0 D, \tag{1}$$

$$\frac{R\rho_1 T_1}{\mu_1} + \frac{aT_1^4}{3} + \rho_1 u_1^2 = P_{G0} + \rho_0 D^2 + K_0, \tag{2}$$

$$\begin{aligned}\rho_1 u_1 &\left(\frac{\gamma}{\gamma-1}\frac{RT_1}{\mu_1} + \frac{4aT_1^4}{3\rho_1} + E_{i1} + \frac{u_1^2}{2}\right)\\ &= \rho_0 D\left(\frac{\gamma}{\gamma-1}\frac{P_{G0}}{\rho_0} + E_{i0} + \frac{D^2}{2}\right) + S_0.\end{aligned} \tag{3}$$

Here, D is the velocity of gas inflow into the discontinuity, i.e., the SW velocity with respect to the matter; P_{G0} is the gas pressure ahead of the discontinuity; $E_i(\rho, T)$ is the specific ionization energy; $\mu(\rho, T)$ is the molecular mass; K and S are the integrated moments of radiation intensity I corresponding to the momentum and energy flux densities:

$$K = \frac{2\pi}{c}\int_{-1}^{1} I\mu_I^2 d\mu_I, \quad S = 2\pi\int_{-1}^{1} I\mu_I d\mu_I, \tag{4}$$

where μ_I is the cosine of the angle between the directions of the velocity and the radiation intensity. For them to be determined, we must consider the shock-front structure by using the transfer equation with allowance for gas motion (Imshennik and Morozov 1964, 1969; Morozov 1966). The structure is usually calculated from the equilibrium state ahead of the discontinuity to the equilibrium state behind the discontinuity. In our case, the optical depth ahead of the discontinuity is small, and there is no equilibrium. Since we do not consider the front structure, S_0 and K_0 are the parameters of the problem (boundary conditions on the "transparent" side) for specified ρ_0, P_{G0}, and D. The radiation ahead of the discontinuity is assumed to be completely "decoupled" with the matter and freely go to infinity. We assume that there is only one-way flux from the discontinuity: no radiation flows into the discontinuity ($I_0 = 0$ for $0 \le \mu_I \le 1$). In this case, disregarding corrections for the motion, we have $S_0 = -F_\infty = -\sigma T_{\rm eff}^4$, where $\sigma = ac/4$ is the Stefan–Boltzmann constant. The flux is taken with the minus sign, because its direction is opposite to the velocity of gas inflow into the discontinuity. The effective temperature $T_{\rm eff}$ is an energy characteristic of the losses and does not necessarily match the color temperature: the spectrum of the outgoing radiation is determined by the front structure, i.e., by processes inside the discontinuity (see, e.g., Tsikulin and Popov 1977). However, it is more convenient to choose parameters related to the temperature T_1 in the final state

$$\delta = \frac{F_\infty}{\sigma T_1^4}, \quad W = \delta^{1/4} = \frac{T_{\rm eff}}{T_1}, \tag{5}$$

and write S_0 as

$$S_0 = -\delta\frac{acT_1^4}{4}. \tag{6}$$

Clearly, $0 \le \delta \le 1$, and the limiting flux from the discontinuity is reached for $\delta = 1$. Assuming the intensity of the outgoing radiation I_0 to be isotropic in the "transparent" hemisphere ($-1 \le \mu_I \le 0$) and using (4) and (6), we obtain

$$K_0 = \frac{1}{2}\delta\frac{aT_1^4}{3}. \tag{7}$$

In fact, the assumption about the angular dependence $I_0(\mu_I)$ is of little importance, because the main contribution to the results comes from the energy flux in (3). As usual, we denoted the reciprocal compression by

$$\eta_1 = \frac{\rho_0}{\rho_1}. \tag{8}$$

Introducing the constants characterizing the initial conditions

$$B = R\left(\frac{3}{a}\right)^{1/4}\rho_0^{1/4}D^{-3/2}, \quad g = \frac{D}{c}, \quad \lambda = \frac{P_{G0}}{\rho_0 D^2} \tag{9}$$

and designating

$$\Theta = \frac{T}{T_{un}}, \quad T_{un} = \left(\frac{3}{a}\right)^{1/4}\rho_0^{1/4}D^{1/2}, \qquad \varepsilon_i = \frac{2}{D^2}(E_{i1} - E_{i0}), \tag{10}$$

from (1)–(3), (6) and (7) we derive the following dimensionless equations, which are convenient for analysis:

$$B\Theta_1\frac{1}{\mu_1} + \Theta_1^4\eta_1 = (1+\lambda)\eta_1 - \eta_1^2 + \frac{1}{3}gQ\eta_1, \tag{11}$$

$$\left(\frac{2\gamma}{\gamma-1}\right)B\Theta_1\frac{1}{\mu_1} + 8\Theta_1^4\eta_1 + \varepsilon_i = 1 + \left(\frac{2\gamma}{\gamma-1}\right)\lambda - \eta_1^2 - Q, \tag{12}$$

where

$$Q = \frac{2F_\infty}{\rho_0 D^3} = \frac{acT_{eff}^4}{2\rho_0 D^3} = \frac{3}{2}\frac{\delta}{g}\Theta_1^4. \tag{13}$$

We also introduce the designations for the ratio of the gas pressure to the total pressure in the final state $\beta_1 = (P_G/P)_1$ and the radiation-to-gas pressure ratio $h_1 = (P_R/P_G)_1$:

$$\beta_1 = \frac{B\Theta_1}{B\Theta_1 + \Theta_1^4\eta_1\mu_1}, \quad h_1 = \frac{\Theta_1^3\eta_1\mu_1}{B}. \tag{14}$$

We are interested in SW velocities typical of SN at the stage when the wave emerges on the stellar surface and begins to propagate through the stellar-wind matter, i.e., of the order of $(5–25)\times 10^3$ km s^{-1}. The range of densities satisfying the conditions when the optical depth of the stellar wind upstream the SW is not enough for the viscous discontinuity to be completely screened is estimated to be of the order of 10^{-16}–10^{-10} g cm^{-3}. This corresponds to a rate of mass loss by the star of 10^{-7}–10^{-3} $M_\odot$ year^{-1} for an outflow velocity of 10–20 km s^{-1}.

Under these conditions, the SWs are strong, and the gas pressure ahead of the discontinuity can be disregarded; we therefore assume that $\lambda = 0$ and $E_{i0} = 0$. We also restrict ourselves to the case of $\gamma = 5/3$ and perform all calculations for pure hydrogen by calculating μ_1 and ε_i for ionization from the ground level. For this statement of the problem, a higher accuracy is not required. We present plots only for a small number of cases, because the qualitative pattern does not change under different initial conditions.

DEPENDENCE OF SW PARAMETERS ON ENERGY LOSSES

The dimensionless flux Q characterizes the fraction of the SW kinetic energy radiated to infinity. Since we consider the case of $\lambda = 0$, all of the energy behind the discontinuity is drawn from the kinetic energy. Using (14), from (11)–(13) we derive the quadratic equation (for $\gamma = 5/3$)

$$3(7-3\beta_1)\eta_1^2 - (8-3\beta_1)(3+gQ)\eta_1 = 3(Q-1+\varepsilon_i). \tag{15}$$

Since $0 < \beta_1 < 1$, we see from the equation that the reciprocal compression $\eta_1 \longrightarrow 0$ as $Q \longrightarrow Q_{fin} = 1 - \varepsilon_i$ (if we disregard ε_i, which is small for large D, then $\eta_1 \longrightarrow 0$ as $Q \longrightarrow 1$). However, for $Q = Q_{fin}$ and $\eta_1 = 0$, Eqs. (11) and (12) have the solution $\Theta_1 = 0$. But the gas with a zero temperature behind the discontinuity does not radiate, in conflict with the statement of the problem. Hence, the flux $Q = Q_{fin}$ is unattainable, and the limiting compression is finite (infinite compression is physically meaningless). This is clearly seen in Figs. 1 and 2. As the energy losses increase [as $\log(1 - Q)$ decreases], the ratio of the effective temperature to the temperature behind the discontinuity monotonically increases, but the limiting value $W = 1$ is reached for $Q_{lim} < Q_{fin}$ and for the corresponding density of the outgoing flux $F_\infty = F_{lim} = Q_{lim}\rho_0 D^3/2$. The reciprocal compression also monotonically decreases with increasing energy losses; it reaches the limiting value η_{lim} at $W = 1$, which is several orders of magnitude smaller than for an adiabatic SW: $\eta_A = 1/(7 - 3\beta_1)$ [the solution of (15) for $\varepsilon_i = 0$ and $Q = 0$].

In Fig. 3, the final and effective temperatures are plotted versus W. We see that there is a certain critical value $W_m(D)$ (W_m is virtually independent of density) for which the maximum temperature behind the discontinuity $T_m = T_1(W_m)$ is reached and which separates the two modes. If $T_{eff} < T_{eff}^{cr} = T_{eff}(W_m)$ and, accordingly, $F_\infty < F_{cr} = F_\infty(W_m)$, then the final-state temperature even increases compared to the adiabatic case. The heating through additional compression dominates over the energy losses. The gas compression at the maximum of T_1 exceeds significantly the adiabatic one. If, alternatively, $W > W_m$, i.e., $F_\infty > F_{cr}$, the matter behind the discontinuity cools down; the cooling is accompanied by a very large compression, as we clearly see in Fig. 2. Obviously, we have $F_\infty = F_{lim}$ for $T_{eff} = T_1 = T_{lim}$. The temperatures T_{eff}^{cr} and T_{lim} are very close, and it is not noticeable on the scale of Fig. 3 that, actually, $T_{eff}^{cr} < T_{lim}$, and the cooling takes place when T_{eff} monotonically increases. The change of mode at F_{cr} is associated with the passage from the leading role of radiation in the final state to the dominance of gas pressure, as we

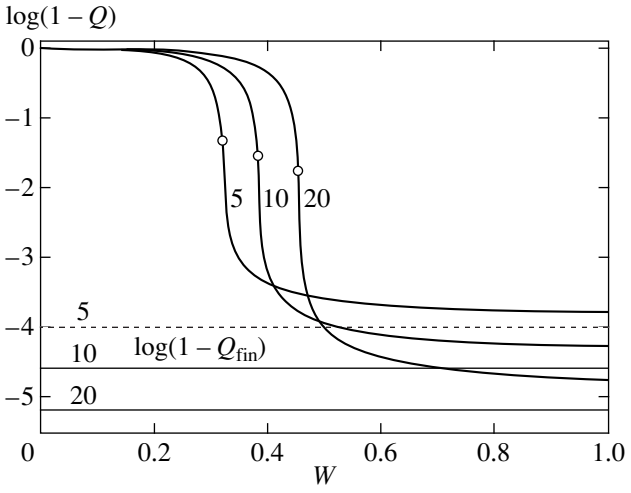

Fig. 1. Fraction of the radiated kinetic energy $Q = 2F_\infty/\rho_0 D^3$ versus ratio of the effective temperature to the final-state temperature $W = T_{\rm eff}/T_1$. The points corresponding to the temperature maximum behind the discontinuity T_1 (see Fig. 3) are marked in the curves. $Q_{\rm fin} = 1 - \varepsilon_i$ corresponds to the energy losses for which the reciprocal compression $\eta_1 = 0$. The numbers alongside the curves are velocities D (in 10^3 km s^{-1}). The density $\rho_0 = 10^{-13}$ g cm^{-3} is the same for all cases.

clearly see in Fig. 4. The gas-to-total pressure ratio behind the discontinuity is nearly zero for $W < W_{\rm m}$ and rapidly increases almost to unity in the state of limiting compression for $W > W_{\rm m}$.

The parameter W is convenient for constructing graphs, because the change of modes becomes clearer. If we consider variations of the quantities behind the discontinuity with outgoing flux, which is physically more correct, then it turns out that energy losses in a wide range have virtually no effect on the final state: the gas compression and the temperature change insignificantly. Only when the flux density approaches its critical value does the compression increases considerably, and the temperature behind the discontinuity slightly rises. However, because of the small difference between $T_{\rm eff}^{\rm cr}$ and $T_{\rm lim}$, even a small excess of the losses over the critical value results in an abrupt cooling and in catastrophic compression of the matter behind the discontinuity.

We call the mode subcritical if $dT_1/dF_\infty > 0$ and supercritical if $dT_1/dF_\infty < 0$; the passage through the maximum $T_1 = T_{\rm m}$ is called a critical point.

THE CRITICAL POINT

The function $\Theta_1(\eta_1)$ given by Eq. (11) for specified B, g, λ, and the parameter Q (or δ) has a maximum. Using the condition $d\Theta_1/d\eta_1 = 0$ (assuming that $\lambda = 0$ and disregarding the derivative of molecular mass), we derive from (11) and (13)

$$\Theta_{\rm m}^4 = \frac{2(1-2\eta_{\rm m})}{2-\delta}. \qquad (16)$$

The inverse substitution in (11) yields

$$B\Theta_{\rm m}\frac{1}{\mu_{\rm m}} = \eta_{\rm m}^2, \qquad (17)$$

which corresponds to an exact equality of the isothermal speed of sound $c_{\rm iz}$ behind the discontinuity to the velocity of gas outflow from the discontinuity u_1. For the final state to coincide with the maximum of Θ_1, (16) and (17) must satisfy Eq. (12). Substituting (16) and

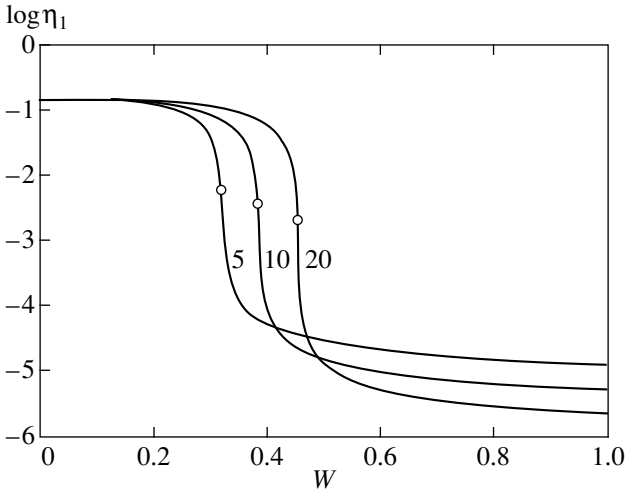

Fig. 2. Reciprocal compression $\eta_1 = \rho_0/\rho_1$ versus $W = T_{\rm eff}/T_1$. The notation and the cases are the same as those in Fig. 1.

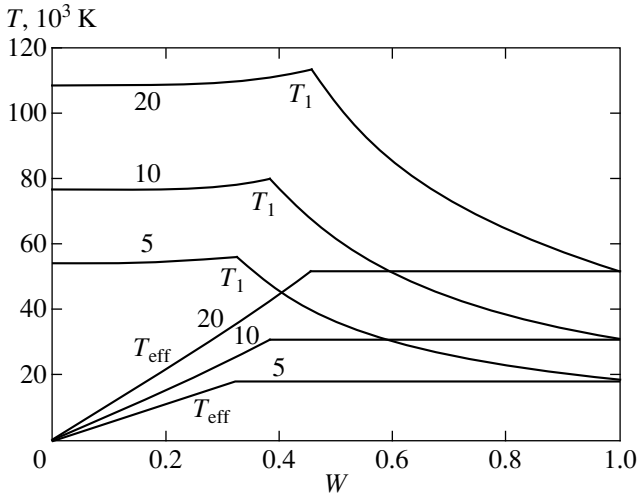

Fig. 3. Temperature behind the discontinuity T_1 and effective temperature $T_{\rm eff}$ versus $W = T_{\rm eff}/T_1$. The notation and the cases are the same as those in Fig. 1.

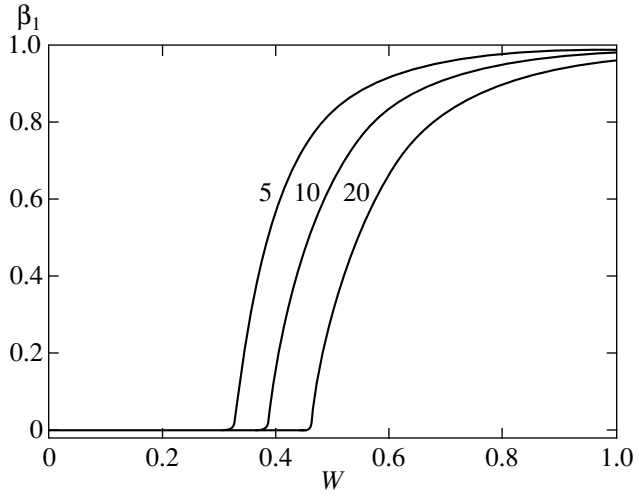

Fig. 4. Gas-to-total pressure ratio behind the discontinuity $\beta_1 = (P_G/P)_1$ versus $W = T_{eff}/T_1$. The notation and the cases are the same as those in Fig. 1.

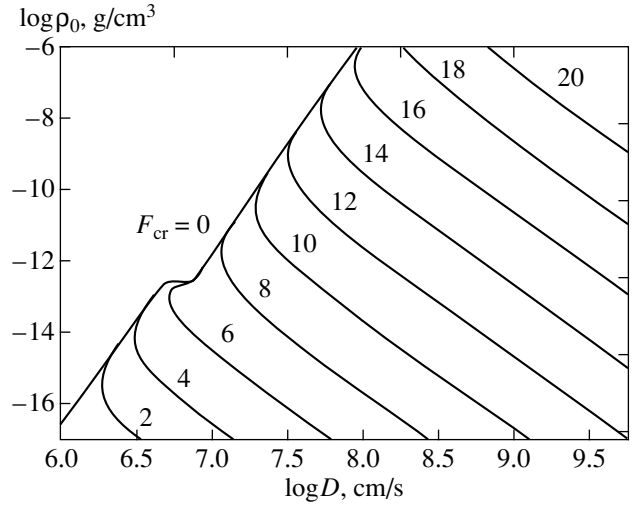

Fig. 5. The domains of existence of the subcritical and supercritical modes. The numbers alongside the curves are $\log F_{cr}$ (erg cm^{-2} s^{-1}). The kink of the $F_{cr} = 0$ curve corresponds to a change of molecular mass μ_{mA} in the final state.

(17) in (12) and assuming that $\varepsilon_i = 0$ yield the quadratic equation for $\gamma = 5/3$

$$2g(10 + 3\delta_m)\eta_m^2 - 2(8g - 3\delta_m)\eta_m = (3 + g)\delta_m - 2g. \quad (18)$$

At $\delta_m = 0$, i.e., for an adiabatic SW, Eq. (18) uniquely determines $\eta_{mA} = 0.155$ and, together with (16) and (17), yields values of the pressure ratio in the final state corresponding to the maximum of T_1: $\beta_{mA} = 0.183$ and $h_{mA} = 4.449$. Zeld'ovich and Raizer 1966 used Eqs. (16), (17), and (18) with $\delta_m = 0$ when considering the structure of the front of a strong adiabatic SW in the approximation of radiative heat conduction. In this case, at $h_1 = h_{mA}$, the transition takes place from a discontinuous solution if $h_1 < h_{mA}$ to a continuous one with $h_1 > h_{mA}$. The same equations yield another critical quantity

$$B_{cr}(\rho_0, D) = \frac{\mu_{mA}\eta_{mA}^2}{(1 - 2\eta_{mA})^{1/4}} = 2.638 \times 10^{-2}\mu_{mA}, \quad (19)$$
$$\mu_{mA} = \mu(\rho_0/\eta_{mA}, T_{mA}(\rho_0, D)).$$

For hydrogen in a wide range of ρ_0 and D, the molecular mass is $\mu_{mA} \simeq 0.5$. If $B > B_{cr}$, then $h_1 < h_{mA}$ in the adiabatic case, and an isothermal discontinuity takes place; the reciprocal compression $\eta_1 > \eta_{mA}$, with $\eta_1 \sim 1/4$ for $B \gg B_{cr}$. If, alternatively, $B < B_{cr}$, then $h_1 > h_{mA}$, and a continuous transition to the final state occurs; the reciprocal compression $\eta_1 < \eta_{mA}$, and $\eta_1 \sim 1/7$ for $B \ll B_{cr}$. The critical values obtained in this way correspond to a treatment of the SW structure in the approximation of radiative heat conduction. Using the kinetic equations slightly changes the values of η_{mA} and h_{mA} (Imshennik 1962, 1975).

In our problem, we cannot infer the front structure of a nonadiabatic SW, and, moreover, we cannot use the approximation of radiative heat conduction for small optical depths. In our case, however, B_{cr} also separates two regions of initial ρ_0 and D. Solving the set of equations (12), (16), and (17) (everywhere $\delta \equiv \delta_m$, $\eta_1 \equiv \eta_m$, $\Theta_1 \equiv \Theta_m$) yields the functions $\delta_m(\rho_0, D)$, $\eta_m(\rho_0, D)$, and $\Theta_m(\rho_0, D)$. Changing to dimensional quantities, we obtain the critical flux density

$$F_{cr}(\rho_0, D) = \frac{ac}{4}\delta_m(\rho_0, D)T_m^4(\rho_0, D). \quad (20)$$

A physically acceptable solution exists only in the region $B \le B_{cr}$; with $F_{cr} = 0$ for $B = B_{cr}$. Hence, if $B \ge B_{cr}$, then $F_{cr} = 0$, and the supercritical mode is always realized for any fluxes from the front, from zero to the limiting one: energy losses reduce the temperature behind the discontinuity. If, alternatively, $B < B_{cr}$, then the temperature rises for $F_\infty < F_{cr}$ and falls for $F_\infty > F_{cr}$. $c_{iz} < u_1$ in the subcritical mode behind the discontinuity and $c_{iz} > u_1$ in the supercritical mode (the adiabatic speed of sound c_{ad} is always larger than u_1).

In Fig. 5, the lines for various values of $F_{cr} = \text{const}$ are drawn in the $\log\rho_0 - \log D$ plane. The regions $B > B_{cr}$ and $B < B_{cr}$ lie to the left and to the right of the $F_{cr} = 0$ line, respectively. Since F_{cr} differs only slightly from the limiting flux density F_{lim} for given ρ_0 and D, the $F_{cr} = \text{const}$ lines (to the right of $F_{cr} = 0$) almost coincide with the $F_{lim} = \text{const}$ lines.

APPROXIMATE FORMULAS

In our case of small ρ_0 and large D, we always have $B < B_{cr}$ and, moreover, $B \ll 1$ and $\eta_m \ll 1$. In this case, according to (16), $\Theta_m \sim 1$. From (17), setting $\mu_m = 0.5$, we immediately obtain an estimate of the reciprocal compression at the critical point,

$$\eta_m \simeq \sqrt{2B} \simeq 0.86\rho_0^{1/8} D_3^{-3/4}, \quad (21)$$

where D_3 is the velocity in 10^3 km s^{-1}, and ρ_0 is in g cm^{-3}. Given that g is small, we obtain from (18) for $\eta_m \ll 1$

$$\delta_m = W_m^4 \simeq \frac{2g}{3+g} \sim \frac{2}{3}\frac{D}{c}. \quad (22)$$

Next, using (16), (17), and (22), we determine the pressure ratios at the critical point

$$h_m \simeq \frac{3+g}{3\eta_m} \sim \frac{1}{\eta_m} \gg 1, \quad \beta_m = \frac{1}{1+h_m} \sim \eta_m \ll 1. \quad (23)$$

We see that $h_m > h_{mA}$, and the contribution of radiation to the total pressure at the critical point is larger than that in the state separating the continuous and discontinuous solutions in an adiabatic SW.

Estimates for the state of limiting compression can be obtained from (11)–(13) for $\eta_1 = \eta_{lim} < \eta_m \ll 1$ and $\delta = 1 (\lambda = \varepsilon_i = 0)$:

$$\eta_{lim} \simeq B\frac{1}{\mu_{lim}}\left(\frac{2}{3}g\right)^{1/4} \simeq 0.16\rho_0^{1/4} D_3^{-5/4}, \quad (24)$$

$$h_{lim} \simeq \frac{2g}{3-g}, \quad \beta_{lim} \simeq \frac{3-g}{3+g} \sim 1. \quad (25)$$

The estimates obtained from formulas (21)–(25) closely agree, with a high accuracy, with numerical calculations for the values of ρ_0 and D we consider.

CONCLUSION

Below, we summarize our results. Energy losses always increase the post-shock gas compression compared to the adiabatic case, and the reciprocal compression $\eta_1 < \eta_A$. However, there is a nonadiabaticity limit. The flux density of the energy radiated to infinity F_∞ cannot exceed the limiting value $F_{lim}(\rho_0, D)$, which depends on the gas density ρ_0 and the shock velocity D, and there is a limiting degree of reciprocal compression $\eta_{lim}(\rho_0, D)$ for a given SW. F_{lim} is close to the flux density of the energy flowing into the discontinuity, but is smaller than it.

The presence of a maximum in the function $\Theta_1(\eta_1)$ defined by Eq. (11) determines the existence of two modes of a nonadiabatic SW. The temperature behind the discontinuity reaches a maximum at a certain flux density $F_\infty = F_{cr}(\rho_0, D)$. A certain degree of gas compression $\eta_m(\rho_0, D)$ and a certain post-shock radiation-to-gas pressure ratio $h_m(\rho_0, D)$, as well as the post-shock equality of the isothermal speed of sound c_{iz} and the gas velocity u_1, correspond to this maximum.

The subcritical (in our terminology) mode corresponds to a reciprocal compression $\eta_1 > \eta_m$, to the dominance of the post-shock radiation pressure, and to $h_1 > h_m$. In the final state, the inequalities $c_{ad} > u_1$, but $c_{iz} < u_1$ hold. This mode is realized when the gas density and the SW velocity correspond to the inequality $B(\rho_0, D) < B_{cr}(\rho_0, D)$, and the radiation flux density $F_\infty < F_{cr}$. Energy losses increase the gas compression compared to an adiabatic SW, but affect weakly the final-state temperature by slightly raising it.

The supercritical mode corresponds to a reciprocal compression $\eta_1 < \eta_m$ and to the final-state inequalities $c_{ad} > u_1$ and $c_{iz} > u_1$. It is always realized if $B > B_{cr}$ (i.e., for any energy losses $F_\infty \le F_{lim}$), as well as for $B < B_{cr}$ and $F_\infty > F_{cr}$. Here, the role of the post-shock gas is significant, and $h_1 < h_m$. As the energy losses increase above the critical ones, the inequalities $c_{iz} > u_1$ and $h_1 < h_m$ are strengthened, the post-shock temperature decreases compared to the adiabatic case, and the gas compression increases by several orders of magnitude. It follows from the closeness of F_{cr} to F_{lim} that even a small excess of the flux over the critical value results in a catastrophic gas compression and in $h_1 \ll 1$.

We cannot definitely judge the structure of a nonadiabatic SW. However, there is a close analogy with the problem of the front structure of a strong adiabatic SW with a major role of radiation if it is considered in the approximation of radiative heat conduction (Zel'dovich and Raizer 1966). Here, two modes separated by the final state $h_1 = h_{mA}$, which is realized for $B = B_{cr}$, are possible, also depending on the wave amplitude. $B < B_{cr}$ and a continuous transition to the final state correspond to the subcritical mode. $B > B_{cr}$ and an isothermal discontinuity correspond to the supercritical mode.

Thus, the case of $B < B_{cr}$ admits a transition to the supercritical mode. However, the energy losses necessary for this to occur are close to the limiting ones. Therefore, such a transition can take place only under unusual conditions, which arise, for example, during a SN explosion, when a SW emerges on the stellar surface, and when the optical depth up to infinity is not enough for the viscous discontinuity to be screened.

Of considerable importance is the presence of an optically thick zone behind the front of a nonadiabatic SW with the dominance of true absorption and the equilibrium of gas with radiation in it, as we assumed when stating the problem. The formation of such a zone can be traced only in more comprehensive model calculations. The necessary increase in opacity takes place in the supercritical mode, whereas in the subcritical mode the scattering dominates. In the models of SN explosions in a stellar wind calculated in the approximation of radiative heat conduction (see, e.g., Grasberg and Nadyozhin 1987), the supercritical mode was realized. With a more accurate allowance for radiative transfer (see, e.g., Blinnikov and Bartunov 1993)), the situation

can be slightly different. The instabilities, which can result in the fragmentation of an optically thick raked-up layer, require a separate analysis.

ACKNOWLEDGMENTS

I wish to thank V.S. Imshennik, D.K. Nadyozhin, and S.I. Blinnikov for helpful discussions.

REFERENCES

1. S. I. Blinnikov and O. S. Bartunov, Astron. Astrophys. **273**, 106 (1993).
2. R. A. Chevalier, Astrophys. J. **258**, 790 (1982).
3. R. A. Chevalier and R. I. Klein, Astrophys. J. **234**, 597 (1979).
4. S. W. Falk and W. D. Arnett, Astrophys. J., Suppl. Ser. **33**, 515 (1977).
5. E. K. Grasberg, Baltic Astron. **3**, 252 (1994).
6. E. K. Grasberg, V. S. Imshennik, and D. K. Nadyozhin, Astrophys. Space Sci. **10**, 28 (1971).
7. E. K. Grasberg and D. K. Nadyozhin, Astron. Zh. **64**, 63 (1987) [Sov. Astron. **31**, 31 (1987)].
8. V. S. Imshennik, Fiz. Plazmy **1**, 202 (1975) [Sov. J. Plasma Phys. **1**, 108 (1975)].
9. V. S. Imshennik, Zh. Éksp. Teor. Fiz. **42**, 236 (1962).
10. V. S. Imshennik and Yu. I. Morozov, Astron. Zh. **46**, 800 (1969) [Sov. Astron. **13**, 628 (1969)].
11. V. S. Imshennik and Yu. I. Morozov, Zh. Prikl. Mekh. Tekh. Fiz., No. 2, 8 (1964).
12. I. A. Klimishin, *Shock Waves in Stellar Envelopes* (Nauka, Moscow, 1984).
13. Yu. I. Morozov, Zh. Prikl. Mekh. Tekh. Fiz., No. 4, 42 (1966).
14. D. K. Nadyozhin, Astrophys. Space Sci. **112**, 225 (1985).
15. D. K. Nadyozhin, Preprint No. 1, ITÉF (Institute of Theoretical and Experimental Physics, Moscow, 1981).
16. M. A. Tsikulin and E. G. Popov, in *Radiative Properties of Sock Waves* (Nauka, Moscow, 1977).
17. Ya. B. Zel'dovich and Yu. P. Raizer, *Physics of Shock Waves and High-Temperature Hydrodynamic Phenomena* (Nauka, Moscow, 1966, 2nd ed.; Academic Press, New York, 1966).

Translated by G. Rudnitskiĭ

Astronomy Letters, Vol. 26, No. 9, 2000, pp. 589–599. Translated from Pis'ma v Astronomicheskiĭ Zhurnal, Vol. 26, No. 9, 2000, pp. 683–694.
Original Russian Text Copyright © 2000 by Lamzin.

Analysis of the HST Ultraviolet Spectra for T Tauri Stars: RY Tau and HD 115043

S. A. Lamzin*

Sternberg Astronomical Institute, Universitetskiĭ pr. 13, Moscow, 119899 Russia

Received September 10, 1999

Abstract—The ultraviolet spectra of the stars RY Tau and HD 115043 from the Hubble Space Telescope are analyzed. RY Tau belongs to the classical T Tauri stars, while HD 115043 is a young ($t \sim 3 \times 10^8$ years), chromospherically active star. The most intense emission lines were identified, and their fluxes were measured. Low-resolution spectra of RY Tau and HD 115043 in the wavelength range 1160–1760 Å exhibit almost the same set of emission lines. However, first, the luminosity of RY Tau in these lines is approximately a factor of 300 higher than that of HD 115043, and, second, the relative line intensities differ greatly. The intensity ratio of the C IV λ1550, Si IV λ1400, and NV λ1240 doublet components is close to 1 : 2 in the spectra of both stars. Judging by the continuum energy distribution, the spectral type of RY Tau is later than that of HD 115043. Synchronous flux variability in the C IV λ1550 and He II λ1640 lines in a time of ~20 min was detected in RY Tau. The flux rise in these lines was accompanied by a redshift of the intensity peak in the profiles by ~50 km s^{-1}. Intermediate-resolution spectra are used to study line profiles in the spectrum of RY Tau. In particular, the profiles of (optically thin) Si III] λ1892 and C III] λ1909 lines were found to be asymmetric and about 300 km s^{-1} in width. The (optically thick) C IV λ1550 doublet lines have similar profiles. The Mg II λ2800 doublet lines are also asymmetric, but their shape is different: they consist of a broad (≃750 km s^{-1} at the base) emission component on which an interstellar absorption line shifted from the line symmetry center by about 20 km s^{-1} is superimposed. The intensity ratio of the Mg II λ2800 doublet components is ≃1.4. Whether there are molecular hydrogen lines in the spectrum of RY Tau is still an open question. It is shown that the emission lines in the ultraviolet spectrum of RY Tau cannot originate in a hydrostatically equilibrium chromosphere. It is argued that quasi-steady accretion of circumstellar matter is responsible for the emission. © *2000 MAIK "Nauka/Interperiodica".*

Key words: *stars—variable and peculiar*

INTRODUCTION

Here, we continue to analyze the ultraviolet spectra of T Tauri stars from the Hubble Space Telescope (HST). We consider RY Tau, a classical T Tauri star (CTTS) with $W_{H\alpha} \sim$ 10–20 Å. There is a fairly large spread in the estimates of its spectral type: from G1–2 IV (Petrov *et al.* 1999) to K1 IV (Hartigan *et al.* 1995). This appears rather strange, because Petrov *et al.* (1999) specially pointed out that the photospheric spectrum of RY Tau had remained unchanged for many years, despite its large ($\Delta V > 1^m$) variability. The above authors also give values of the interstellar extinction A_V for the star differing by a factor of 2: from $0\overset{m}{.}55$ to $1\overset{m}{.}3$.

Correlated variations in the magnitude and direction of the polarization vector suggest that the variability of RY Tau results from an eclipse of the star by dust fragments (protocomets) with fairly large dust grains (Eaton and Herbst 1995; Petrov *et al.* 1999). The relatively high projected rotational velocity of the star, $v \sin i \simeq 50$ km s^{-1} (Hartmann *et al.* 1986), testifies that the line of sight passes not too far from the plane of the (protoplanetary) disk around RY Tau. On the other hand, radical changes in the profile shape and equivalent widths of emission lines were observed in the star (Eaton and Herbst 1995); therefore, the variability of RY Tau, at least occasionally, is associated with nonstationary processes near the stellar surface.

For comparison, we analyzed the spectrum of HD 115043 (=Gl 503.2), which is marked in the HST archive as a weak-line T Tauri star (WTTS). The presence of a weak ($W \simeq 0.09$ Å) emission feature in the Hα line (Soderblom and Mayor 1993a) and fairly intense ($L_X \simeq 8.9 \times 10^{28}$ erg s^{-1}) X-ray radiation (Hunsch *et al.* 1999) apparently served as a ground for this classification. However, judging by its kinematic parameters (Soderblom and Mayor 1993a) and lithium abundance (Soderblom *et al.* 1993), the age of HD 115043 is ~3×10^8 years; i.e., it lies near the zero-age main sequence. Neither optical variability nor circumstellar matter were detected in this star (Tsikoudi and Bromage 1995). This all implies that HD 115043 should be classified as a chromospherically active star rather than

* E-mail address for contacts: lamzin@sai.msu.ru

as a WTTS. Note in this connection that $v\sin i$ for HD 115043 $\simeq$ 7.5 km s^{-1} for HD 115043; it is unlikely that we observe this star at a small inclination i (Soderblom and Mayor 1993b).

Since the spectral type of HD 115043 is G2, i.e., more or less similar to that of RY Tau, it is of interest to compare the ultraviolet spectra of both stars in order to elucidate the nature of the RY Tau activity. Below, we show what kind of information can be extracted from an analysis of the HST spectra.

OBSERVATIONAL DATA

The spectra analyzed below were taken from the HST archive (http://archive.stsci.edu/hst/target.descriptions.html). We reduced the spectra by means of the IRAF v2.11 (http://iraf.noao.edu/iraf) and STSDAS/TABLES v2.0.2 (http://ra.stsci.edu/STSDAS.html) software packages. The standard technique described in Chapter 36 of the HST Data Handbook (http://www.stsci.edu/documents/data–handbook.html) was used; the files recommended in the archival database were used for calibration.

Intermediate- and low-resolution spectra of RY Tau were obtained with the GHRS spectrograph on December 31, 1993, and November 13, 1994, respectively. HD 115043 was observed only once, on May 19, 1994, and only in low-resolution mode. The GHRS spectrograph in this mode with a G140L grating has a 0.57 Å resolution per photodiode of the receiving array, which is a factor of 10 lower than that in intermediate-resolution mode. On the other hand, this is an order of magnitude higher than that in low-resolution spectrograms from the IUE satellite, which until now have been almost the only source of information about the spectra of CTTSs in the wavelength range 1200–2000 Å.

Table 1 gives the identification numbers of archival spectra, the diffraction grating used, the wavelength range, the number of intermediate exposures (parameter RPTOBS+1), the starting time of the first exposure to within a minute (UT), and the total exposure. All spectra were taken in ACCUM mode through aperture LSA ($D \simeq 2''$) and have the same values of the following service parameters: FP_SPLIT = 'NO', STEPPATT = 5, and COMB_ADD = 'FOUR'. The abbreviation W_Cal in column "Object" refers to calibration spectra for wavelength calibration. Similar calibrations were also made during low-dispersion observations, but they were not used here and, hence, are not given in the table. The 1993 and 1994 spectra were taken on detectors 2 and 1, respectively. The wavelengths were corrected for the Earth's and spacecraft motions and are given below for a vacuum. We used the Atomic Line List v2.01 electronic database (http://www.pa.uky.edu/peter/atomic) for line identification.

INTERPRETATION OF THE SPECTRA

Figure 1 shows the spectrum of RY Tau near the Mg II λ2800 resonance doublet. The doublet lines have identical asymmetric profiles: an interstellar absorption line, whose intensity minimum coincides, within the error limits, with the laboratory λ_c, is superimposed on a broad (~750 km s^{-1} at the base) emission component. The fluxes in Mg II λ2803.5 and Mg II λ2796.4 are 8.95×10^{-13} and 1.23×10^{-12} erg s^{-1} cm^{-2}, respectively; i.e., the former line is a factor of 1.37 weaker than the latter.

The wings of both emission lines are nearly symmetric about the central wavelength; the centroid determined from them is shifted from λ_c approximately by +20 km s^{-1}, in agreement with V_r = +16.4 km s^{-1} obtained by Hartmann *et al.* (1986) from optical photospheric lines. Thus, the observed asymmetry of the Mg II line profiles appears to result from a shift between the centers of the emission and absorption lines. To illustrate this assertion, Fig. 1 (upper right corner) shows how the Gaussian $y = \exp(-x^2)$ on which an "absorption line" with $\tau(x) = 2\exp[-(x + 0.25)^2/0.01]$ is superimposed appears. The Gaussians (and their parameters) were taken only for convenience: the actual profiles of the line emission components are poorly fitted by Gaussians.

We see from Fig. 1 that there is a weak, but undoubtedly real broad emission feature near λ = 2792 Å. If it is assumed to be attributable to Mg II λ2796 stellar-wind emission, then its short-wavelength boundary corresponds to a gas velocity $V_w \simeq 600$ km s^{-1}. This value appears abnormally large, because the short-wavelength boundary of the [O I] 6300 line in the RY Tau spectrum does not exceed –200 km s^{-1} (Hamann 1994). Identification of this emission feature with Mg II λ2791.60 belonging to the $^2P^o$–^2D (uv3) multiplet seems more likely. The lower level of this line is apparently pumped by Mg II k emission, while Mg II h photons must excite the upper level of the two remaining lines in the uv3 triplet: λλ 2798.75 and 2798.82 Å. Unfortunately, the presence or absence of these lines falling on the Mg II k red wing is by no means obvious (see Fig. 1). Completing the description of Fig. 1, note the presence of a continuum with an intensity of $\simeq 9.6(\pm 3.4) \times 10^{-15}$ erg s^{-1} cm^{-2} Å^{-1}.

Figure 2 shows two intermediate-resolution spectra of RY Tau. Since the quality of the spectra is not high, averaged (by the method of moving average over four points) data are shown in the figure. Nevertheless, a number of interesting features are seen in the spectrograms.

First of all, we see from Fig. 2a that the Si III λ1892 and C III λ1909 intercombination lines have asymmetric profiles with blueshifted peaks. It is important that the total line width exceeds 300 km s^{-1}: since these lines are optically thin (for example, $A_{ij} \simeq 97.3$ s^{-1} for C III] λ1909), the shape of their profiles strongly sug-

Table 1. Information about the analyzed spectra

Date	t_0, UT	Spectrum code	Object	Grating	Δλ, Å	N_{exp}	Δt, s
Dec. 21, 1993	04:20	z1e70103t	W_Cal	G160M	1503–1539	1	5
	04:31	z1e70104t	RY Tau	G160M	1382–1419	4	1088
	05:53	z1e70105t	RY Tau	G160M	1532–1567	5	1360
	06:17	z1e70106t	RY Tau	G160M	1623–1658	5	1360
	07:37	z1e70107t	W_Cal	G200M	2082–2121	1	5
	07:43	z1e70108t	RY Tau	G200M	1879–1920	5	1496
	08:58	z1e70109t	W_Cal	G270M	2879–2924	1	5
	09:04	z1e7010at	RY Tau	G270M	2777–2823	1	245
May 19, 1994	10:32	z2dl0107t	HD 115043	G140L	1162–1449	10	3535
	12:23	z2dl0109t	HD 115043	G140L	1430–1714	11	3890
Nov. 13, 1994	09:32	z2dl0207t	RY Tau	G140L	1162–1449	21	7426
	14:12	z2dl020an	RY Tau	G140L	1430–1714	22	7779

gests gas motion at a velocity above 100 km s^{-1} in the emission region. The C IV λ1548, 1551 doublet resonance lines have similar profiles (see Fig. 2b). The C IV lines probably have a significant optical depth (see below), and it would be natural to expect their profiles to differ from those of the intercomination lines. Unfortunately, this cannot be judged for certain because of the low signal-to-noise ratio.

For the same reason, whether there is a continuum in Fig. 2 is also still an open question. The identifications of emission features with iron lines (Fe II λ1897.549 and the Fe II a^4D–w^4D^o multiplet lines) shown in the figure were made by analogy with the spectrum of RU Lup (Lamzin 2000a). The archive contains two more intermediate-mode spectrograms of RY Tau which were taken on December 31, 1993, near the Si IV λ1400 doublet and the He II λ1640 line, but their quality is so low that they are virtually unsuitable for analysis.

Let us now consider the low-resolution spectra of the stars under study obtained with the G140L grating.

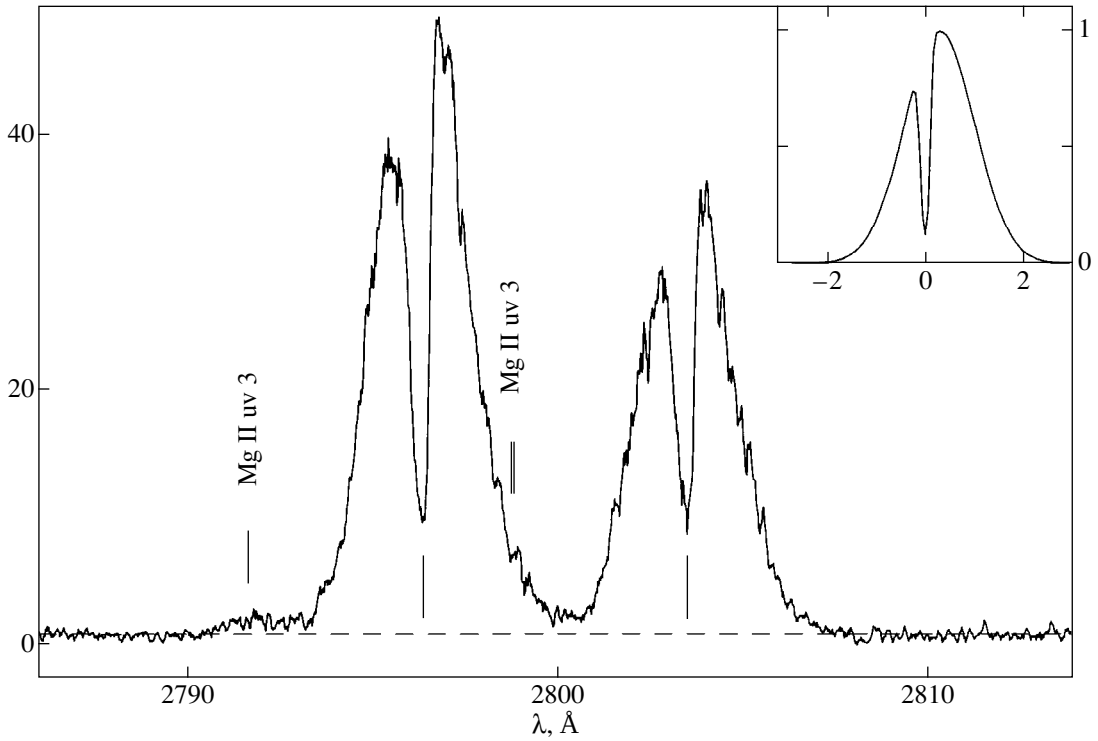

Fig. 1. The spectrum of RY Tau near 2800 Å. The spectral flux density (in units of 10^{-14} erg s^{-1} cm^{-2} A^{-1}) is plotted along the y axis in this and the following figures.

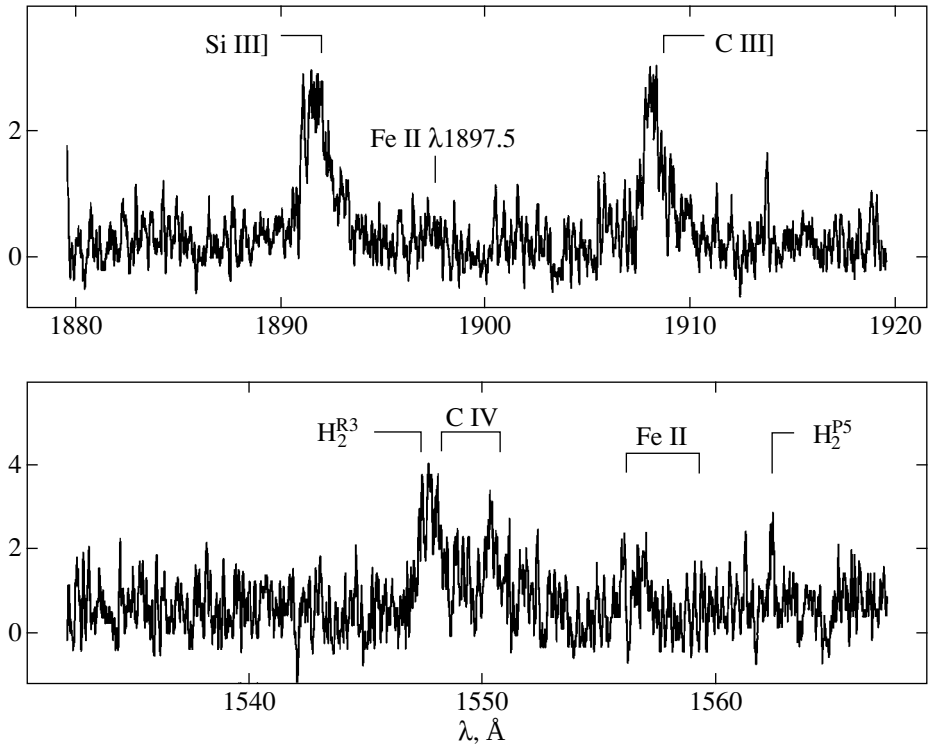

Fig. 2. Intermediate-resolution spectra for RY Tau.

Figures 3 and 4 show the spectra of RY Tau and HD 115043 in the ranges 1160–1420 and 1460–1720 Å, respectively. Statistically significant emission features are identified in the figures; more detailed information about the corresponding lines and the fluxes in them is given in Table 2. For strong lines, the flux was determined with an accuracy no lower than 10%, except for the Si IV λ1402.77 line in the spectra of both stars and the O I 1304 multiplet in the spectrum of HD 115043: the values in Table 2 appears to have been appreciably overestimated due to blending. For weak lines, blending and/or uncertainty in the continuum level prevented a reliable determination of the flux: there is a question mark against these lines in the corresponding column. For three weak, but undoubtedly real features, it is difficult to find an unambiguous identification: they are marked by Latin letters in Fig. 3 and Table 2. The spectra of both stars exhibit a very intense (and highly variable) H I Lα line, which was reported by the staff of the HST Institute to belong entirely to the geocorona (Dashevski *et al.* 1999).

Without providing evidence, Walter and Liu (1998) assert that there are molecular hydrogen lines in the spectra of RY Tau we study. Two emission features that could be identified with the H_2 R(3) λ1547.34 and P(5) λ1562.39 lines observed in the spectrum of RU Lup [see Fig. 5a in Lamzin (2000a)] are labeled in Fig. 2b. These two Lyman lines have the common upper level $2p\sigma B^1\Sigma_u^+$ $v' = 1$, $J' = 4$ and the lower levels with $v'' = 8$, $J'' = 3$ and $v'' = 8$, $J'' = 5$, respectively, which belong to the ground electronic configuration $X^1\Sigma_g^+$. However, the reality of these emission features is by no means obvious, because their intensity is comparable to the noise signal. Moreover, it follows from Fig. 4 that, eleven months later, the P(5) λ1562.39 line was virtually absent in the spectrum of RY Tau, as were the R(3) λ1489.57 and P(5) λ1504.76 lines with the same upper level and with an almost twice as large A_{ij}; the expected positions of these three lines are marked by crosses. (The position of R(3) λ1547.34 is not shown in Fig. 4, because it merges with C IV λ1548 at low resolution.) Thus, whether H_2 lines are present in the spectrum of RY Tau is still an open question.

Qualitatively, the spectra of RY Tau and HD 115043 are closely similar and exhibit virtually the same set of lines. However, the relative line intensities in these stars differ markedly, as we see from Fig. 5, which shows equally spaced segments whose lengths are proportional to the intensity ratio of the corresponding multiplet and the C IV λ1550 doublet. The heavy, thin solid, and thin dashed lines correspond, respectively, to the spectra of HD 115043, RY Tau, and the quiet Sun, as constructed by Linsky *et al.* (1982). The observed fluxes in the RY Tau spectrum were corrected for interstellar extinction by assuming a "standard law" (Seaton 1979) with A $A_V = 0.^m6$ in Fig. 5a and $A_V = 1.^m2$ in Fig. 5b. The fluxes in the HD 115043 spectrum were not cor-

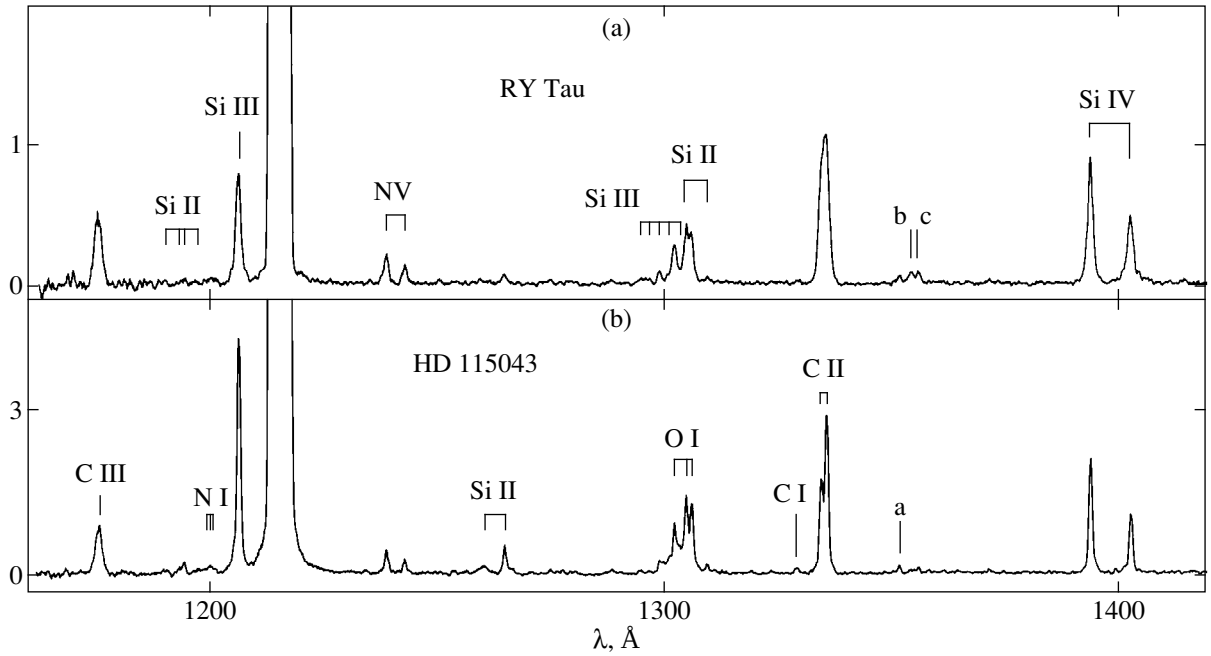

Fig. 3. Low-resolution spectra for (a) RY Tau and (b) HD 115043 in the range 1160–1420 Å.

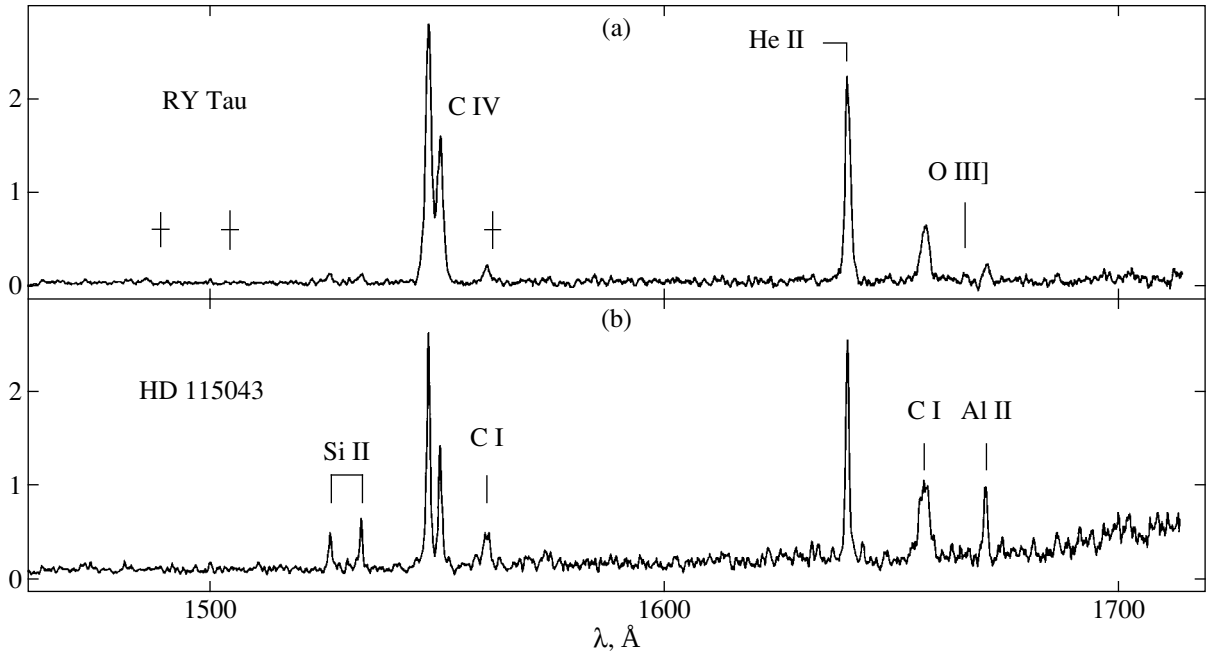

Fig. 4. Low-resolution spectra for (a) RY Tau and (b) HD 115043 in the range 1460–1720 Å.

rected for interstellar extinction, because the star is 25.6 pc away (Soderblom and Mayor 1993a). Incidentally, a comparison of Figs. 5a and 5b indicates that the uncertainty in A_V for RY Tau does not affect strongly our results.

Each low-resolution spectrum in Figs. 3 and 4 is an average over a fairly large series of independent exposures (see Table 1). For RY Tau and HD 115043, they were taken during three and two HST revolutions around the Earth, respectively. When comparing individual spectra, we found appreciable intensity variations of C IV λ1550 and He II λ1640 in the RY Tau spectrum.

Figure 6 shows how the flux in the C IV λ1550 and C I λ1657 multiplet lines varied with time; we call this

Table 2. The observed line fluxes

λ, Å	Species	Transition	F, 10^{-14} erg s^{-1} cm^{-2}	
			RY Tau	HD 115043
1176	C III	$2s2p\ ^3P^o–2p^2\ ^3P$	0.994	1.72
1194	Si II	$3s^23p\ ^2P^o–3s3p^2\ ^2P$	?	0.565
1200	N I	$2p^3\ ^4S^o_{3/2}–2p^23s\ ^4P$	?	?
1206.510	Si III	$3s^2\ ^1S_0–3s3p^1\ P^o_1$	1.32	5.04
1238.821	N V	$2s\ ^2S_{1/2}–2p\ ^2P^o_{1/2}$	0.293	0.496
1242.804	N V	$2s\ ^2S_{1/2}–2p\ ^2P^o_{3/2}$	0.150	0.287
1260.422	Si II	$3s^23p\ ^2P^o_{1/2}–3s3p^2\ ^2D_{3/2}$	?	0.399
1265	Si II	$3s^23p\ ^2P^o_{3/2}–3s3p^2\ ^2D$	0.010	0.655
1300	Si III	$3s3p\ ^3P^o–3p^2\ ^3P$	0.01	0.24
1304	O I	$2p^4\ ^3P–2p^33s\ ^3S^o_1$	1.46	4.9
1309.276	Si II	$3s^23p\ ^2P^o_{3/2}–3s3p^2\ ^2S_{1/2}$	?	?
1329	C I	$2s^22p^2\ ^3P–2s2p^3\ ^3P^o$	?	0.096
1335	C II	$2s^22p\ ^2P^o–2s2p^2\ ^2D$	2.65	4.69
1351.7	?a		?	0.114
1354.3	?b		?	?
1355.7	?c		?	?
1393.755	Si IV	$3s^2S_{1/2}–3p\ ^2P^o_{1/2}$	1.49	2.27
1402.770	Si IV	$3s^2S_{1/2}–3p\ ^2P^o_{3/2}$	0.9	1.18
1526.707	Si II	$3s^23p\ ^2P^o_{1/2}–3s3p^2\ ^2S_{1/2}$	0.155	0.378
1533.431	Si II	$3s^23p\ ^2P^o_{3/2}–3s3p^2\ ^2S_{1/2}$	0.156	0.511
1550	C IV	$2s^2S_{1/2}–2s\ ^2P^o$	7.40	4.25
1561	C I	$2s^22p^2\ ^3P–2s2p^3\ ^3D^o$	0.326	0.772
1640.42	He II	2p–3d	3.33	2.48
1657	C I	$2p^2\ ^3P–2p3s\ ^3P^o$	1.31	2.64
1666.153	O III	$2s^22p^2\ ^3P_2–2s2p^3\ ^5S^o_2$	<0.08	–
1670.787	Al II	$3s^2\ ^1S_0–3s3p^3\ ^1P^o_1$	0.24	0.93

event a flare. To improve the signal-to-noise ratio, we combined individual observations during each HST revolution into two groups of equal duration. The points in the figure correspond to the mean times of observations and the group-averaged fluxes. The duration of observations and the rms deviation from the mean flux are shown for each point. There is no doubt that the flux in the C IV λ1550 doublet lines during the third HST revolution rose by more than a factor of 1.5 compared to the initial one, whereas the flux in the C I 1657 multiplet lines apparently did not change appreciably: the flux averaged during the three revolutions is indicated in Fig. 6 by a dashed line.

It is important that the flux rise in C IV λ1550 and He II λ1640 was accompanied by a change in the shape of their profiles, implying that some nonstationary phenomenon is observed in the line formation region. Figure 7 shows the line profiles for the same groups as

those in Fig. 6; for comparison, the profile of the first group (Fig. 7a) is indicated in Figs. 7b–7f by dashed lines. We see that the intensity peak of both C IV λ1550 doublet lines is redshifted from the initial one already during the second HST revolution. The shift reaches $\simeq$+60 km s^{-1} at the flare maximum (Fig. 7e) and then apparently decreases. The redshift in the intensity peak during the third HST revolution is also clearly seen in He II λ1640.

RY Tau: AN ACTIVE CHROMOSPHERE OR AN ACCRETION SHOCK WAVE?

The main problem in the physics of T Tauri stars is to elucidate the nature of their emission spectra. Two alternative explanations of the phenomenon are currently considered: a thick chromosphere and an accretion shock wave. The situation is complicated by the possible contribution of stellar-wind radiation to the CTTS emission spectrum.

The outward similarity between the ultraviolet spectra of the Sun and T Tauri stars is commonly considered as an argument for the chromospheric model (see, e.g., Brooks *et al.* 1999). If the activity of CTTSs, as that of HD 115043, were associated with the presence of a thick chromosphere, then it would be natural to expect the spectrum of HD 115043 to differ less from the solar one than does the spectrum of RY Tau, because the projected rotational velocity of RY Tau is approximately a factor of 7 higher. Incidentally, the fact that the lines in the spectrum of HD 115043 are appreciably narrower than those in the spectrum of RY Tau (see Figs. 3 and 4) is apparently explained by the difference in $v\sin i$.

As for the luminosities of the stars under study in the C IV λ1550 line, for example, this is actually the case: disregarding the interstellar extinction, we find that $L_{\mathrm{C\,IV}} \simeq 3.4 \times 10^{27}$ erg s^{-1} for HD 115043; this value is approximately a factor of 500 lower than that for RY Tau (at $A_V = 1\overset{m}{.}0$ and d = 140 pc), but a factor of 8 higher than that for the Sun (Linsky *et al.* 1982). However, if we look at the relative line intensity of various species (Fig. 5), then the situation is not than unambiguous.

We now turn our attention to the profiles of the Si III λ1892 and C III λ1909 intercombination lines in the spectrum of RY Tau. It was already noted above that their shape, as in the case of RU Lup, suggests gas motion at a velocity $U > 100$ km s^{-1} in their formation region. This implies that these lines cannot originate in regions similar to the solar chromosphere! Note that U considerably exceeds the speed of sound at the temperature of maximum C^{++} and Si^{++} abundance under coronal equilibrium conditions. The clear asymmetry of the C IV λ1550 line profiles also points to gas motion in the region of maximum C^{+++} abundance. However, since these lines may have a significant optical depth, the shape of their profiles does not allow the gas velocity in the corresponding region to be directly determined.

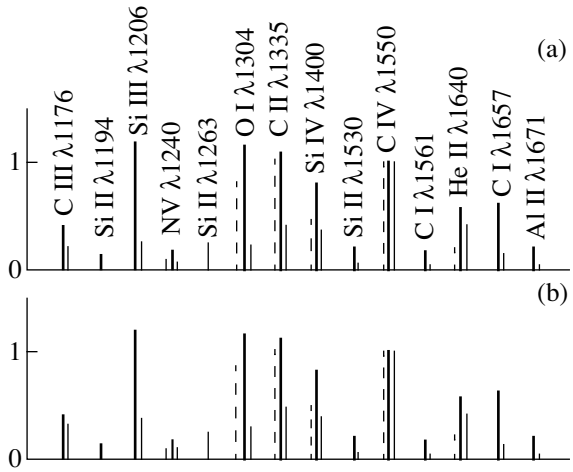

Fig. 5. The relative intensity of multiplets in the spectra of HD 115043 (heavy line), RY Tau (thin solid lines), and the quiet Sun (thin dashed lines). The total intensity of the C IV λ1550 doublet lines was taken as a unity. The observed fluxes for RY Tau were corrected for interstellar extinction with (a) $A_V = 0\overset{m}{.}6$ and (b) $A_V = 1\overset{m}{.}2$.

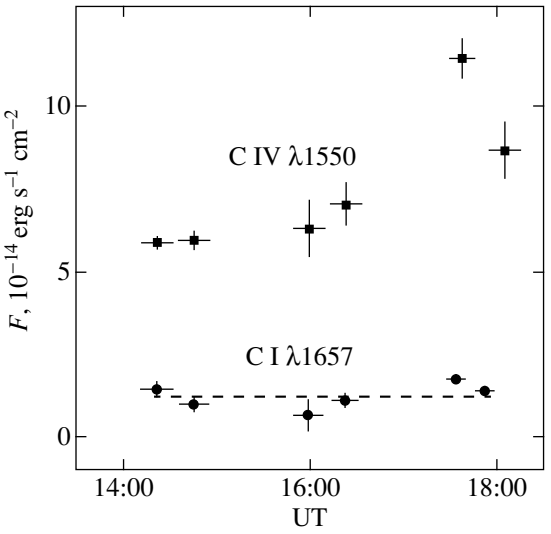

Fig. 6. Change in the intensity of the C IV λ1550 and C I λ1657 multiplets in the spectrum of RY Tau during a flare.

We see in Fig. 2 that the Si III] λ1892 and C III] λ1909 lines have approximately the same intensity ($F \simeq 4 \times 10^{-14}$ erg s^{-1} cm^{-2}); therefore, if they are assumed to be formed under coronal equilibrium conditions, then the electron density N_e in their formation region must exceed 10^{10} cm^{-3} (Keenan *et al.* 1987). Taking the distance to the star to be 140 pc and the extinction to be $A_V = 1\overset{m}{.}0$, we find the luminosity in the intercombination lines under consideration for a normal interstellar extinction law (Seaton 1979) to be $\simeq 10^{30}$ erg s^{-1}. Based

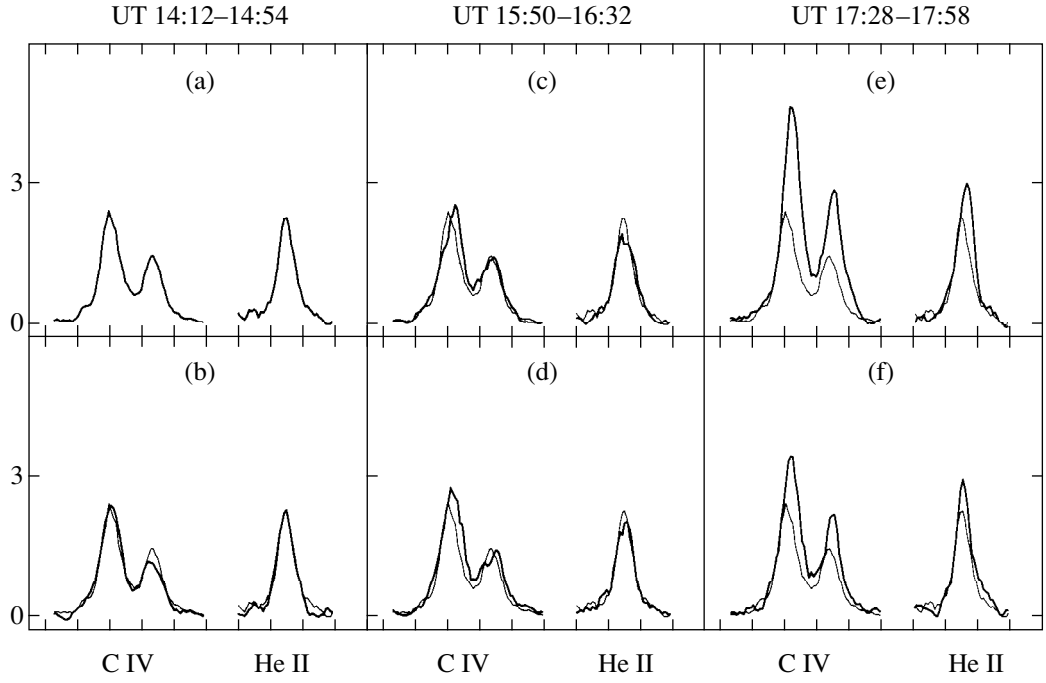

Fig. 7. The C IV λ1548+1551 and He II λ1640 line profiles in the spectrum of RY Tau at various times during a flare.

on the standard technique used to analyze stellar chromospheres and on the corresponding atomic data from Brooks *et al.* (1999), we find, for example, that the volume emission measure in the emitting region for Si III] λ1892 is $EM \sim 3 \times 10^{53}$ cm^{-3}. This implies that the volume of the emitting region for $N_e > 10^{10}$ cm^{-3} is $V < 3 \times 10^{33}$ cm^3, and that its characteristic size is $l \sim V^{1/3} < 10^{11}$ cm, i.e., smaller than the stellar radius $R_* \sim 3R_\odot$.

Let us now assume that the intercombination lines under consideration originate in a stellar wind. If the mass outflow took place from the stellar surface, then, given that $l < R_*$, the extent of the C III] λ1909 and Si III] λ1892 red wings would be a factor of 2 or 3 smaller than that of the blue ones, because the wind is screened by the star; however, we see from Fig. 2 that this is not the case. For the same reason, there can be no radial mass outflow from the magnetosphere either unless it extends further than $2R_*$.

The high temperature needed for the lines of the species under consideration to be formed and the large N_e make the hypothesis of their formation in the stellar wind "blowing" from the accretion-disk surface at a considerable distance from the star unattractive. The intercombination-line emission is unlikely to be associated with the shock waves produced by the interaction of the stellar wind with the ambient medium either: precisely because $N_e \sim 10^3$–10^6 cm^{-3} in Herbig–Haro objects; by contrast to the spectrum of RY Tau, C III] λ1909 in their spectra is several-fold more intense than Si III] λ1892.

The above discussion leads us to conclude that, in the case of RY Tau, the ultraviolet emission lines do not originate in a stellar wind. Petrov (1990) associated the optical line emission region with active structures like giant prominences corotating with the star. If the ultraviolet emission is assumed to be associated with the same active structures, then it should be recognized that they are virtually always present in the star. This follows from the fact that our measured C III] λ1909 and Si III] λ1892 fluxes differ by no more than a factor of 2 from the means obtained over the entire period of IUE observations in the 1980s [see Table 1 in Gomez de Castro and Lamzin (1999)].

According to Petrov *et al.* (1999), these regions must lie at high latitudes, because it follows from observations that the emission region is not eclipsed by dust fragments of the disk. However, the total width of the ultraviolet intercombination lines is much larger than $v \sin i$ determined from photospheric lines. Therefore, active regions must be at a height of 1 or $2R_*$ above the stellar surface, which raises the question of their heating mechanism.

In the accretion model, the ultraviolet lines originate in the regions behind and ahead of the accretion-shock front. We have shown previously (Lamzin 2000b) that the observed shape of the C III] λ1909 and Si III] λ1892 profiles in the spectrum of RY Tau can be reproduced in the accretion-shock model if the velocity field of the infalling gas differs markedly from an axisymmetric one. However, it would be premature to draw final conclusions from the only spectrogram of a rather low quality. Note only that the shock wave during magneto-

spheric accretion must be localized just at high latitudes.

Gomez de Castro and Lamzin (1999) showed that the basic shock parameters, the density and velocity of the pre-shock accreted gas, could be determined from the intensity ratio of O III] λ1665, C III] λ1909 and Si III] λ1892. The O III] λ1661+1666 doublet lines did not fall within the range of the intermediate-resolution spectrograms taken on December 31, 1993; as for the intensity ratio of Si III] λ1892 and C III] λ1909, we can only say that it lies in the range from 1 to 1.5 because of the low signal-to-noise ratio in Fig. 2a. Assuming the gas infall velocity to be close to 300 km s^{-1}, we find from the corresponding diagram that the accreted-gas density N_0 must be $\sim 1\text{–}2 \times 10^{11}$ cm^{-3}.

This value is approximately a factor of 30 lower than N_0 for RU Lup (Lamzin 2000a). From the viewpoint of the accretion model, this circumstance accounts for the low intensity of the veiling continuum, the Hα equivalent width that is an order of magnitude smaller than that for RU Lup, and the relative weakness of the lines of singly ionized metals in the ultraviolet spectrum of RY Tau. The molecular hydrogen lines, which originate in stellar winds from young stars, are either completely absent or have a much lower (and highly variable) intensity than those in RU Lup. It is unclear whether this is associated with the star's relatively low Lα luminosity or the stellar wind from RY Tau is considerably less intense than that from RU Lup. The relatively low intensity of the O I λ1304 multiplet, whose lines are commonly assumed to be excited through fluorescent pumping by H I Lβ photons, argues for the former assumption.

Of the three intercombination lines mentioned above, only O III] λ1666 falls within the range of the November 13, 1994 spectrograms; the flux in this line does not exceed 8×10^{-16} erg s^{-1} cm^{-2}, i.e., it is more than an order of magnitude lower than the flux in C III] λ1909 eleven months earlier. Figures 1–3 from Lamzin and Gomez de Castro (1998) show that these two lines must have approximately the same intensity for all reasonable parameters of the accretion shock wave. It is unclear whether observations are in conflict with theoretical calculations or such a large difference between the line intensities is attributable to variability.

The lines of the subordinate $^3P^o$–^3P multiplet belonging to C III (λ ≃ 1176 Å) and Si III (λ ≃ 1300 Å) were identified (for the first time in T Tauri stars) in the low-resolution spectra for HD 115043 and RY Tau. The presence of these lines points to the sufficiently high N_e needed for the $^3P^o$ term to be pumped; downward transitions from this term are accompanied by the emission of C III] λ1909 and Si III] λ1892. Let us consider the flux ratio of the Si III 1296 and 1892 Å lines in the spectrum of RY Tau while remembering that the fluxes refer to different dates. For the Si III 1296 flux, we can only give an upper limit: $F_{1296} < 7 \times 10^{-17}$ erg s^{-1} cm^{-2} (see Fig. 3a and Table 2). Assuming that $F_{1892} \simeq 4 \times 10^{-14}$ erg s^{-1} cm^{-2} for A_V in the range from $0\overset{m}{.}6$ to $1\overset{m}{.}3$, we therefore find that $\xi = F_{1296}/F_{1892} < 2 \times 10^{-3}$ with an accuracy of ~30%. Meanwhile, it follows from calculations of Si III level populations that $\xi > 5 \times 10^{-3}$ for $T > 3 \times 10^4$ K and $N_e > 10^{10}$ cm^{-3} [see Fig. 1 in Dufton *et al.* (1983)]. The calculations by Dafton *et al.* refer to the case of a small optical depth in the Si III resonance lines, but allowance for the finite optical depth in the 1206.5 Å line only increases the $3s3p\,^1P_1^0$ level population, which must increase ξ further still. For theory to be reconciled with observations, we must either assume that the temperature in the Si III line formation region is appreciably lower than 30 000 K or attribute the discrepancy to variability.

The simultaneous presence of C III] λ1909 and C IV λ1550 with asymmetric profiles in the spectrum of RY Tau suggests a wide range of temperatures in the moving gas. It is easy to understand that, under coronal equilibrium conditions, i.e., when the gas ionization is attributable to electron impacts, this circumstance does not allow the temperature in the Si III line formation region to be reduced, because the Si III abundance exponentially decreases with decreasing temperature. Abandoning the assumption of coronal equilibrium in the chromospheric hypothesis poses the problem with the source of ionizing radiation, because the X-ray luminosity of RY Tau is $L_X \sim 5 \times 10^{29}$ erg s^{-1} (Damiani *et al.* 1995); i.e., it is even lower than, for example, that in the C IV λ1550 lines. Thus, if we associate the ultraviolet emission region with active structures, then the observed smallness of ξ can be attributed only to large variability.

However, in the accretion-shock model, Si III ions are produced just at $T < 30\,000$ K: through gas photoionization by X-ray radiation ahead of the front and because the recombination is slower than the cooling behind the front (Lamzin 1995, 1998). Unfortunately, a theoretical spectrum of the accretion shock wave cannot be directly compared with the observed one. The problem is that most of the observed lines are resonance ones, and theory predicts that they must have a considerable optical depth. Consequently, the spectrum must depend markedly on the geometry of the accretion zone, and this is a special problem requiring a special study.

As for the ultraviolet flux variability of RY Tau, the following is worth noting. As we already pointed out above, the fluxes in C III] λ1909 and Si III] λ1892 on December 31, 1993, were approximately a factor of 2 lower than the mean values in the previous decade. The C IV λ1550 and Si IV λ1400 fluxes on November 13, 1994, were lower than the respective means by factors of 1.5 and 3.7, while the He II λ1640 flux was slightly higher than the mean [Table 2; see also Gomez de Castro and Franqueira (1997)]. This suggests that the variability is not related to eclipses by dust fragments and is nontrivial in nature. The latter, in particular, implies

that the similarity between the peak intensities of the C IV λ1550 lines in Figs. 2a and 4 does not prove that the fluxes in C III] λ1909 or Si III] λ1892 were approximately the same on December 31, 1993, and November 13, 1994.

Recall in this connection that variability in the C IV λ1550 lines was detected just on November 13, 1994, and the line profile in Fig. 2a was averaged over all observations. What can be said about the nature of this flare? If the intensity peak in the C IV λ1550 profiles was actually redshifted during the second HST revolution (Fig. 7), then it should be concluded that the flare began at about 16:00, although this is not so evident from Fig. 6. In that case, however, by contrast to classical chromospheric flares, the rise in the star's line intensity was appreciably slower than its fall. Moreover, the intense C IV λ1550 emission lasts no more than fractions of a second during chromospheric flares (Katsova *et al.* 1997). Even if the intensity did not rise during the HST second revolution, the fairly small flux dispersion at maximum light (Fig. 7) suggests that the flare lasted no less than 20 min. Based on the above discussion and taking into account the redshift of the intensity peak in the C IV λ1550 and He II λ1640 profiles, we believe the flare to have resulted from an increase in the accretion rate of the circumstellar matter.

Unfortunately, we cannot quantitatively analyze the spectrum of HD 115043, because there are no spectra of sufficiently high resolution and no information about the Si III] λ1892 and C III] λ1909 line intensities. As was pointed out above, the star's luminosity in the ultraviolet lines and the electron density in their formation region are appreciably higher than those for the Sun. This suggests that the resonance lines, of which the ultraviolet spectrum of HD 115043 mostly consists, can have a considerable optical depth, and, hence, the validity of using the standard technique for determining the dependence $EM(T)$ raises doubts. We detected no flux variability in the ultraviolet lines over three hours of observations, so the regions where these lines originate are stationary enough.

By contrast to RY Tau, a continuum is clearly seen in HD 115043 in the range 1460–1720 Å, which is peculiar in that its slope abruptly changes near 1700 Å. The radiation from the photosphere and the chromosphere probably dominates at $\lambda > 1700$ Å and at shorter wavelengths, respectively. The absence of a veiling continuum in the blue part of the optical spectrum for RY Tau (Valenti *et al.* 1993) suggests that its contribution is fairly small in the ultraviolet as well. For this reason, the absence of an appreciable rise in the continuum intensity of RY Tau near 1700 Å apparently provide evidence that its spectral type is later than that of HD 115043.

CONCLUSION

Our analysis of the HST spectra for RY Tau unequivocally proves that its ultraviolet spectrum cannot be formed in a hydrostatically equilibrium chromosphere. The presence of a fairly large number of resonance and subordinate lines in the star's ultraviolet spectrum leaves no doubt that the nature of the emission can be eventually elucidated through proper observations. This requires obtaining high-quality spectra of relatively low resolution in the entire range 1100–3000 Å at close times and tracing changes in the Si III] λ1892, C III] λ1909, and C IV λ1550 profiles over several days by using spectrograms with resolution of ~30 km s^{-1}.

ACKNOWLEDGMENTS

I wish to thank the Hubble Space Telescope Institute for permission to access the archive of HST observations; I. Dashevsky, L. Dressel, and C Leitherer for advice on spectrum reduction; M. Katsova, V. Kornilova, and A. Rastogruev for helpful discussions; and A. Zaitseva for help in installing the IRAF–STSDAS software package, which was widely used here, as was the Atomic Line List v.2 database.

REFERENCES

1. D. H. Brooks, V. M. Costa, M.T.V.T. Lago, and A. C. Lanzafame, Mon. Not. R. Astron. Soc. (1999) (in press).
2. F. Damiani, G. Micela, S. Sciortino, and F. R. Harden, Astrophys. J. **446**, 331 (1995).
3. P. L. Dufton, A. Hibbert, A. E. Kingston, and G. A. Doschek, Astrophys. J. **274**, 420 (1983).
4. I. Dashevski, L. Dressel, and C. Leitherer, private communication (1999).
5. N. L. Eaton and W. Herbst, Astron. J. **110**, 2369 (1995).
6. A. I. Gomez de Castro and S. A. Lamzin, Mon. Not. R. Astron. Soc. **304**, L41 (1999).
7. A. I. Gomez de Castro and M. Franqueira, *ULDA Access Guide to T Tauri Stars observed with IUE*, ESA SP-1205, ESTEC (ESA Publications Division, Noordwijk, 1997).
8. F. Hamann, Astrophys. J., Suppl. Ser. **93**, 485 (1994).
9. P. Hartigan, S. Edwards, and L. Ghandour, Astrophys. J. **452**, 736 (1995).
10. L. Hartmann, R. Hewett, S. Stahler, and R. Mathieu, Astrophys. J. **309**, 275 (1986).
11. M. Hunsch, J. H. M. M. Schmitt, M. F. Sterzik, and W. Voges, Astron. Astrophys., Suppl. Ser. **135**, 319 (1999).
12. M. M. Katsova, A. Ya. Boĭko, and M. M. Livshits, Astron. Astrophys. **321**, 549 (1997).
13. F. P. Keenan, P. L. Dufton, and A. E. Kingston, Mon. Not. R. Astron. Soc. **225**, 859 (1987).
14. S. A. Lamzin, Astron. Astrophys. **295**, L20 (1995).
15. S. A. Lamzin, Astron. Zh. **75**, 367 (1998) [Astron. Rep. **42**, 322 (1998)].
16. S. A. Lamzin, Pis'ma Astron. Zh. **26**, 273 (2000a) [Astron. Lett. **26**, 225 (2000)].
17. S. A. Lamzin, Astron. Zh. **77**, 373 (2000).

18. S. A. Lamzin and A. I. Gomez de Castro, Pis'ma Astron. Zh. **24**, 862 (1998) [Astron. Lett. **24**, 748 (1998)].
19. J. Linsky, P. Bornman, K. Carpenter, *et al.*, Astrophys. J. **260**, 670 (1982).
20. P. P. Petrov, Astrophys. Space Sci. **169**, 61 (1990).
21. P. P. Petrov, G. V. Zajtseva, Yu. S. Efimov, *et al.*, Astron. Astrophys. **341**, 553 (1999).
22. M. J. Seaton, Mon. Not. R. Astron. Soc. **187**, 75 (1979).
23. D. Soderblom and M. Mayor, Astron. J. **105**, 226 (1993a).
24. D. Soderblom and M. Mayor, Astrophys. J. Lett. **402**, L5 (1993b).
25. D. Soderblom, C. A. Pilachowski, S. B. Fedele, and B. F. Jones, Astron. J. **105**, 2299 (1993).
26. V. Tsikoudi and G. E. Bromage, Astron. Astrophys. **293**, 64 (1995).
27. J. A. Valenti, G. Basri, and C. M. Johns, Astron. J. **106**, 2024 (1993).
28. M. Walter and Y. Liu, Astron. Soc. Pac. Conf. Ser. **143**, 360 (1998).

Translated by V. Astakhov

Astronomy Letters, Vol. 26, No. 9, 2000, pp. 600–608. Translated from Pis'ma v Astronomicheskiĭ Zhurnal, Vol. 26, No. 9, 2000, pp. 695–704.
Original Russian Text Copyright © 2000 by Taranova, Shenavrin.

Infrared Photometry of the Symbiotic Novae V1016 Cyg and HM Sge in 1978–1999

O. G. Taranova* and V. I. Shenavrin

Sternberg Astronomical Institute, Universitetskiĭ pr. 13, Moscow, 119899 Russia

Received February 10, 2000

Abstract—The photometric *JHKLM* observations of the symbiotic novae V1016 Cyg and HM Sge in 1978–1999 are presented. Parameters of the cool stars themselves and the dust envelopes are estimated. The periods of 470 ± 5 days (for V1016 Cyg) and 535 ± 5 days (for HM Sge) are reliably determined from the entire set of our photometric *J* data for V1016 Cyg and HM Sge. In addition, monotonic light and color variations are observed on a time scale of several thousand days, with the increase in infrared brightness occurring with the simultaneous decrease in infrared color indices; i.e., the dust envelopes in which both components of the systems were embedded before the outburst of their hot sources in 1964 and 1975, respectively, had continued to disperse until late 1999. The amplitudes of these variations for HM Sge are almost twice those for V1016 Cyg. For HM Sge, the dust envelope reached a maximum density near JD 2447500 and then began to disperse. In the case of V1016 Cyg, a maximum density of the dust envelope was probably reached near JD 2444800, and its dispersal has been continuing for about 20 years. Thus, in both symbiotic novae, their dust envelopes reached a maximum density approximately eight years after the outburst of the hot component and then began to disperse. An analysis of the color–magnitude (*J–K, J*) diagram reveals that grains in the dust envelopes of V1016 Cyg and HM Sge are similar in their optical properties to impure silicates. The observed [*J–K, K–L*] color variations for the symbiotic novae under study can be explained in terms of the simple model we chose by variations in the Mira's photospheric temperature from 2400 to 3000 K and in the dust-envelope optical depth from 1 to 3 at a wavelength of 1.25 μm for a constant grain temperature. The observed *J–K* and *K–L* color indices for both symbiotic novae, while decreasing, tend to the values typical of Miras. The dust envelopes of both symbiotic novae are optically thick. The dust envelope around HM Sge is, on the average, twice as dense as that around V1016 Cyg; the Mira in V1016 Cyg is slightly cooler (~2800–2900 K) than that in HM Sge (~2600–2700 K). The dust-envelope density decreases as the Mira's temperature increases. The absolute bolometric magnitudes are $-5^m.1 \pm 0^m.15$ for V1016 Cyg and $5^m.27 \pm 0^m.17$ for HM Sge. Their distances are 2.8 ± 0.6 and 1.8 ± 0.4 kpc, respectively; the luminosities and radii of their cool components (Miras) are $8.6 \times 10^3 L_\odot$, $1 \times 10^4 L_\odot$, $500 R_\odot$, and $540 R_\odot$. The radii of their dust envelopes are $1400 R_\odot$ and $1500 R_\odot$; the masses are $(3–3.3) \times 10^{-5} M_\odot$ and $(4–8) \times 10^{-5} M_\odot$. The dust envelope of V1016 Cyg disperses slower than that of HM Sge by almost a factor of 25.
© 2000 MAIK "Nauka/Interperiodica".

Key words: *stars—variable and peculiar; dust envelopes*

INTRODUCTION

In 1978, we initiated systematic *JHKLM* photometry of the peculiar objects V1016 Cyg (N Cyg 1964) and HM Sge (N Sge 1975), which has been continuing up until now. Both systems are very slow novae. They are currently classified as D-type symbiotic novae (with appreciable near-infrared radiation from the circumstellar dust envelope), whose cool components are Miras with periodic infrared light pulsations (Taranova and Yudin 1983; Yudin 1994). These objects attracted the attention of astronomers after their optical outbursts: V1016 Cyg in 1965 (McCuskey 1965) and HM Sge in 1975 (Dokuchaeva and Balash 1975). These two symbiotic stars are similar spectrophotometrically, but all processes are shifted in time by approximately one and a half decades. The similarity shows up in the luminosities of their components, in the brightness ratio of the Mira and the planetary nebula, in the duration of the active phase, in the prolonged return to quiescence, and in the presence of a circumstellar nebula detectable during ground-based observations. Before the outburst, both systems were embedded in a dense dust envelope, which first expanded after the outburst of the system's hot component and then began to dis-

* E-mail address for contacts: taranova@sai.msu.ru

perse. Symbiotic novae like V1016 Cyg and HM Sge are in quiescence for a long time (decades) and undergo the only intense outburst in their photometric history. It follows from polarization observations of V1016 Cyg (Schmid 1997) that the orbital period of this binary can be 60–100 years.

We published the infrared light curves for V1016 Cyg before 1984 (Taranova and Yudin 1986) and for HM Sge before 1993 (Yudin *et al.* 1994; Yudin 1994). Here, our goal is to analyze parameters of the cool sources in the two symbiotic novae V1016 Cyg and HM Sge by using long-term infrared photometry in the standard *JHKLM* system.

OBSERVATIONS

The *JHKLM* photometry of V1016 Cyg and HM Sge has been performed with the 1.25-m telescope at the Crimean Station of the Sternberg Astronomical Institute (SAI) since 1978 as part of our program of research on circumstellar dust envelopes. The photometric standards were the stars BS 7796 (for V1016 Cyg) and BS 7488 (for HM Sge) from the catalog by Johnson *et al.* (1966). We estimated the *H*, *L*, and *M* magnitudes of the standards from their spectral types by using data from Koornneef (1983). The angular diameter of the photometer aperture was about 12″, and the beam spatial separation during modulation was ~30″ in the east–west direction. The errors in the *JHK* and *LM* magnitude estimates did not exceed $0^m.03$ and $0^m.05$, respectively.

Our *JHKLM* photometry for V1016 Cyg and HM Sge is shown in Figs. 1 and 2 in the form of infrared light and color curves in 1978–1999; the vertical arrows mark the dates before which our observations have been previously published and analyzed[1].

DISCUSSION

Infrared Light and Color Variations in V1016 Cyg and HM Sge Since 1978

V1016 Cyg. From 1983 until 1999, as before, the system's near-infrared light and color variations exhibited a periodicity of several hundred days. As we see from Fig. 1, these periodic variations are grouped into "bunches" of three or four waves, after which a glitch is observed in the periodic variations; subsequently, they are restored. The glitch in the periodic variations in the summer of 1983 (marked with number *1* in Fig. 1) was analyzed by Taranova and Yudin (1986), and a sporadic ejection of the dust envelope, whose parameters are given in the above paper, turned out to have taken place in the system at this time. Episode *2*, when, judging by the light and color variations, it can be stated qualitatively that a break emerged on the line of sight and persisted for about three years, is marked in Fig. 1: the near-infrared brightness initially rose, and the system became bluer (the color indices decreased), and, subsequently, all regained their original level. In other words, it may be said that structural and temporal nonuniformities in the dust envelope can affect appreciably the Mira's periodic light and color fluctuations.

Apart from the light and color fluctuations in V1016 Cyg with a period of several hundred days, a nearly linear trend is clearly seen from the beginning of our observations in 1978 until, at least, late 1999, i.e., on a time scale of several thousand days. The monotonic increase in infrared brightness occurs with the simultaneous decrease in infrared color indices, implying that the envelope in which both components of the system were embedded before the outburst of the hot source in 1964 had continued to disperse until late 1999. In Fig. 1, our observations are fitted by second-degree polynomials (dashed lines), whose parameters are given in Table 1 (SD are the standard deviations). Taranova and Yudin (1983, 1986) estimated the dust-envelope temperature to be ~600 K; consequently, only the Mira's radiation attenuated by the dust envelope is seen in the wavelength range 1–2.5 μm, while the envelope itself contributes no more than 1 or 2%. Based on the observations before 1984, we attempted to determine the kind of grains in the dust envelope by analyzing the observed color–magnitude relations in the near infrared (Taranova and Yudin 1986). These grains turned out to be similar in their optical properties to dust grains composed of pure silicates. Using the same method for the entire set of our observations of V1016 Cyg, we attempted to refine the conclusion reached previously. Figure 3 shows the *J–K*, *J* color–magnitude diagrams for V1016 Cyg observed in 1978–1999 (circles), and the regression line whose parameters are given in the lower left corner is indicated by dashed line *1*. The slope of this line is given by $B = \Delta J/\Delta(J–K)$. If we attribute the mean *J* light and *J–K* color variations in Fig. 3 only to variations in the dust-envelope optical depth on the line of sight, then $\Delta J/\Delta(J–K) \approx \tau(J)/[\tau(J) – \tau(K)] \approx Q(J)/[Q(J) – Q(K)]$, where $\tau(J)$ and $\tau(K)$ are the optical depths, and $Q(J)$ and $Q(K)$ are the grain absorption efficiencies. With other things being equal, the wavelength dependences of τ and Q are sensitive to the kind of dust grains. A comparison of the observed $\Delta J/\Delta(J–K) = B$ and $Q(J)/[Q(J) – Q(K)]$ calculated for various kinds of dust grains (discussed as probable grains in dust envelopes) by using data from Rowan-Robinson and Harris (1982) leads us to conclude that $B = 1.83 \pm 0.13$ (Fig. 3) more likely agrees with impure silicates than with pure ones. Note that $\Delta J/\Delta(J–K) \approx 1.56$ for interstellar dust grains.

HM Sge. Periodic infrared light and color variations on a time scale of several hundred days are also clearly seen in the infrared light and color curves for this symbiotic nova (Fig. 2). As in the case of V1016 Cyg, monotonic light and color variations are also observed on a time scale of several thousand days; they are rep-

[1] Electronic tables with our photometric *JHKLM* data for these stars will be accessible via Internet at http://infra.sai.msu.ru/~taranova by the middle of 2000.

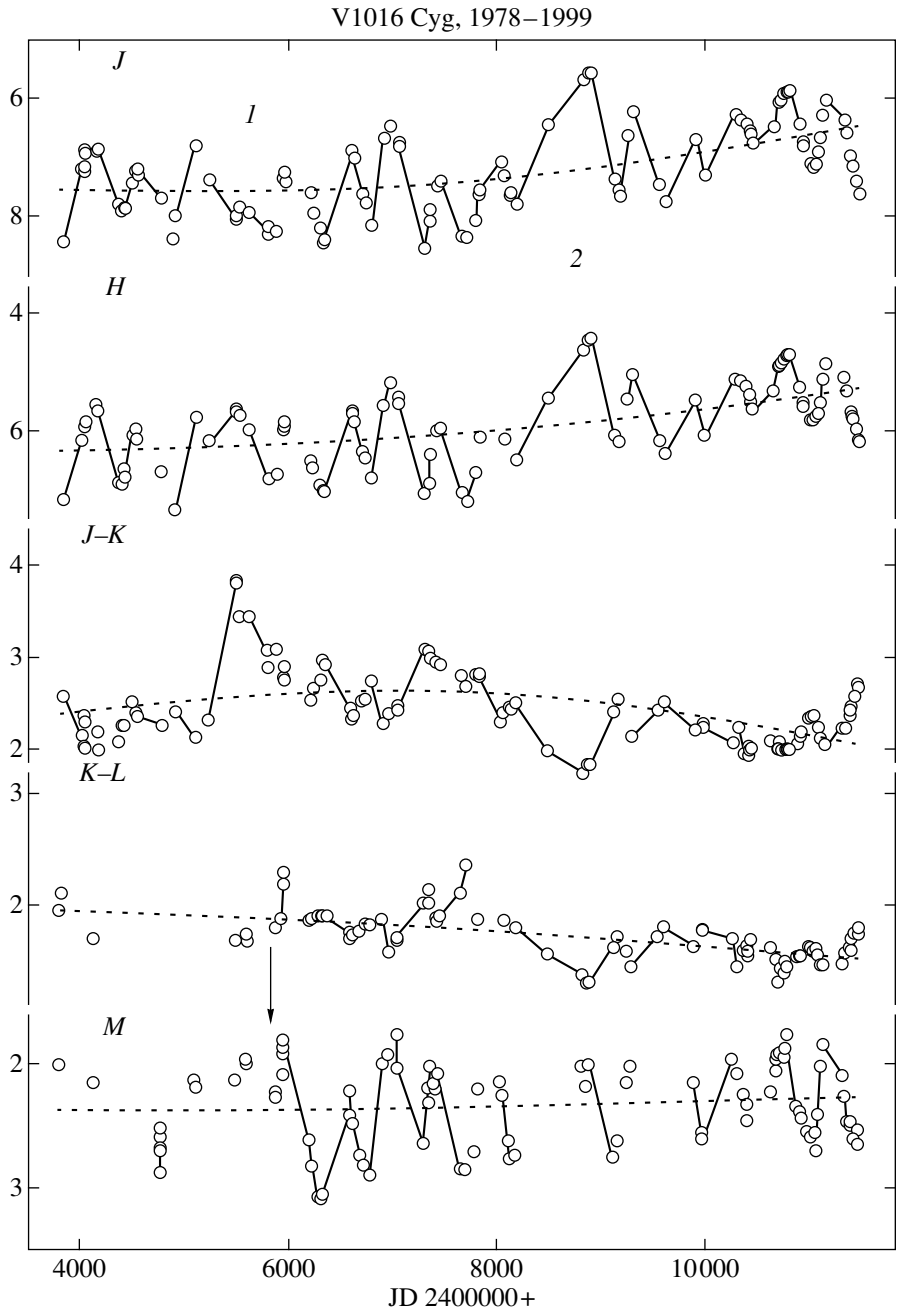

Fig. 1. *JHM* light and *J–K*, *K–L* color curves for V1016 Cyg in 1978–1999. The observations are indicated by circles, and the dashed lines represent second-order polynomial fits to the observed variations (see the text for the arrows).

resented by second-order lines (dashed lines) in Fig. 2, whose parameters are given in Table 1. It follows from Fig. 2 and Table 1 that an infrared brightness minimum and the largest reddening of the system were observed in the monotonic infrared light and color variations of HM Sge near JD 2447500. Although the long-term light and color variations of HM Sge and V1016 Cyg are similar in pattern (the decline in the systems' infrared brightness is accompanied by their reddening), the amplitudes of these variations for HM Sge are almost a factor of 2 larger. In addition, if we attribute, as in the case of V1016 Cyg, the monotonic infrared light and color variations of HM Sge to optical-depth variations in the dust envelope, which began to expand after the outburst of the system's hot source in 1975, then it can be inferred from Fig. 2 and Table 1 that this envelope reached a maximum density near JD 2447500 and then began to disperse. As follows from Fig. 1 and Table 1, the dust envelope in V1016 Cyg reached its maximum density near JD 2444800, and its dispersal has been

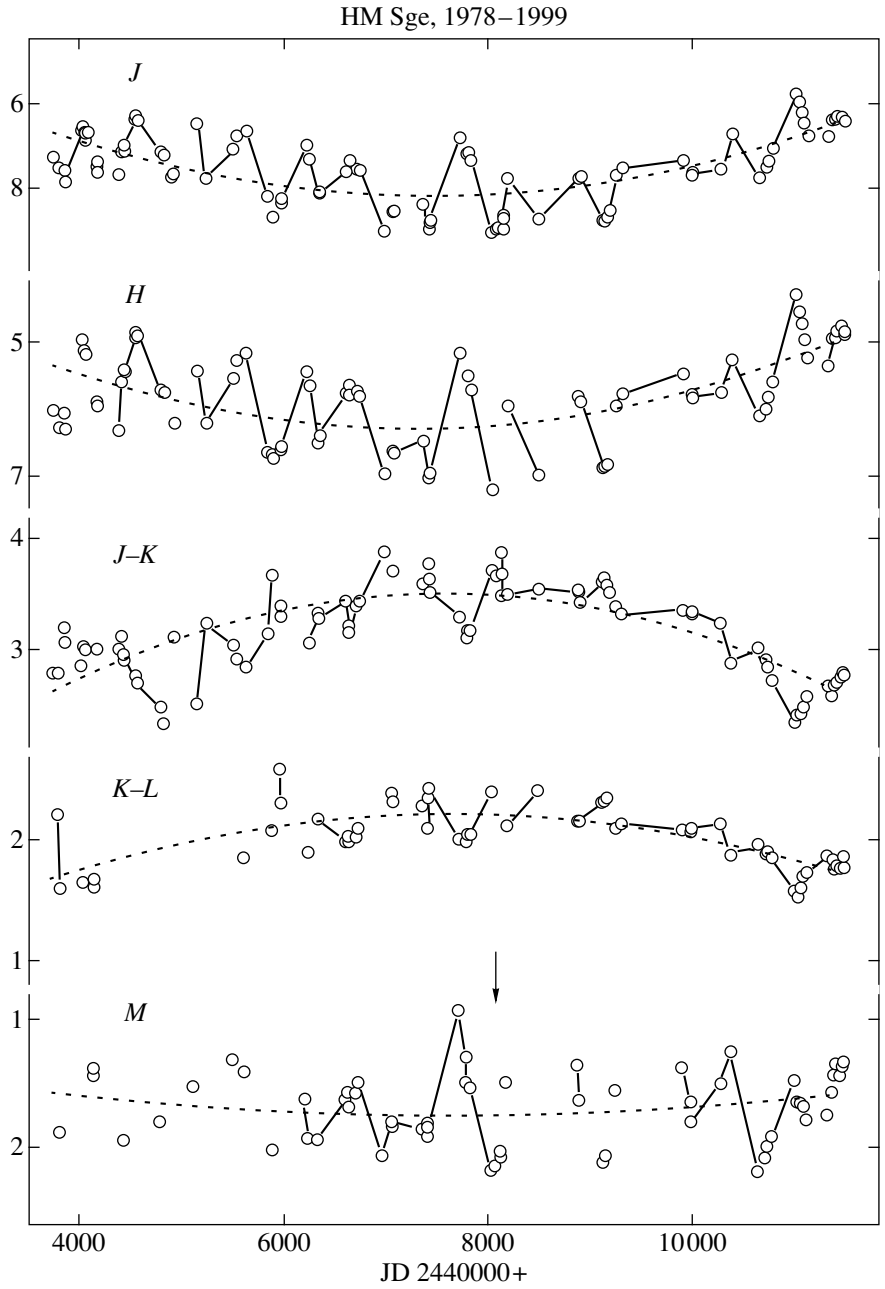

Fig. 2. Same as Fig. 1 for HM Sge.

continuing for about 20 years. Thus, the dust envelopes in both symbiotic novae reached their maximum density approximately eight years after the outburst of the hot component and then began to disperse.

In the color–magnitude diagram (Fig. 3), the data for HM Sge are indicated by asterisks, and dashed line *2* represents the regression line whose parameters are given in the lower left corner of the figure. We see from this diagram that the slopes of the regression lines for V1016 Cyg and HM Sge are virtually the same. In other words, the grains in the dust envelope of HM Sge may also be similar to impure silicates.

Figure 4 shows the periodograms and the spectral windows constructed from the entire set of our photometric *J* data for V1016 Cyg and HM Sge. The periods of 470 ± 5 days (for V1016 Cyg) and 535 ± 5 days (for HM Sge) are reliably determined. A periodicity on a time scale of ~1900 days can be noted in the periodogram for V1016 Cyg; this value is close to the observed cyclicity of "bunches" (see above) in the system's light curves. It has been established previously (Harvey 1974; Taranova and Yudin 1986, 1983) that the periods of 470 and 535 days are the pulsation periods of the cool components (Miras) in the symbiotic novae under study.

Table 1. A polynomial fit to the infrared photometric data for V1016 Cyg and HM Sge: $A = A_0 + A_1x + A_2x^2$ (R is the correlation coefficient)

V1016 Cyg

Parameter	J	SD	H	SD	$J–K$	SD	$K–L$	SD	M	SD
A_0	6.95	0.71	6.28	0.72	1.4	0.4	2.07	0.31	2.29	0.56
A_1	2.62×10^{-4}	0.0002	6.85×10^{-5}	0.0002	3.61×10^{-4}	0.00011	-1.59×10^{-5}	0.00008	2.77×10^{-5}	0.00014
A_2	-2.70×10^{-8}	1.24×10^{-8}	-1.39×10^{-8}	1.24×10^{-8}	-2.63×10^{-8}	7.24×10^{-9}	-2.50×10^{-9}	4.67×10^{-9}	-2.77×10^{-9}	8.67×10^{-9}
R	0.56	0.62	0.56	0.58	0.46	0.35	0.59	0.17	0.12	0.33

HM Sge

Parameter	J	SD	H	SD	$J–K$	SD	$K–L$	SD	M	SD
A_0	2.2	0.6	2.3	0.6	1.1	0.3	0.20	0.27	1.11	0.47
A_1	0.0016	0.0002	0.0011	0.00018	8.97×10^{-4}	0.00008	5.24×10^{-4}	0.00007	1.66×10^{-4}	0.00012
A_2	-1.07×10^{-7}	1.15×10^{-8}	-7.63×10^{-8}	1.64×10^{-8}	-5.93×10^{-8}	5.19×10^{-9}	-3.41×10^{-8}	4.35×10^{-9}	-1.09×10^{-8}	7.38×10^{-9}
R	0.69	0.59	0.63	0.55	0.78	0.25	0.74	0.16	0.20	0.27

On the Dust Envelopes of V1016 Cyg and HM Sge

Let us consider some properties of the dust envelopes in the symbiotic novae under study. In the two-color [$J–K$, $K–L$] diagram (Fig. 5), the observed colors of V1016 Cyg and HM Sge corrected for interstellar extinction [with $E(B–V) \sim 0^m.25$ for V1016 Cyg and $\sim 0^m.6$ for HM Sge] are represented by open circles and asterisks, respectively. The solid lines (NS) indicate the color variations of normal stars (Koornneef 1983). The dotted line indicates the colors of a blackbody as its temperature changes from 3000 to 1200 K. The segment of the dashed line indicates the color variations for normal interstellar extinction with $E(B–V) = 1^m$. The filled circles refer to the mean color indices for some of the Miras we observed (Taranova 2000). Solid lines *1* and *2* represent the model color variations in a system that consists of a central star surrounded by a dust envelope. We performed our model calculations by making the following simplifying assumptions:

(1) The observed monotonic near-infrared light and color variations in the symbiotic novae V1016 Cyg and HM Sge are mainly attributable to variations in the optical depth of the dust envelope heated by the Mira;

(2) The dust grains in these envelopes are similar in their optical properties to impure silicates, and their radius is ~0.1 μm;

(3) The dust envelopes are spherically symmetric and physically thin.

In this case, simple relations from our previous paper (Taranova 2000) can be used to estimate the basic parameters of such a system. In our model calculations, the Mira's photospheric temperature was varied in the range 2400–3000 K with a step of 200 K. The parameter β, which depends on the kind of grains, was taken to be 1.35 for impure silicates (Jones and Merrill 1976). We calculated the $J–K$ and $K–L$ color indices for dust grains heated from 300 to 800 K and varied the dust-envelope optical depth in the range 0–5 with a step of 0.5 at a wavelength of 1.25 μm (J band). As a result, it turned out that the observed variations in the above color indices could be explained in terms of our simple model by variations in the Mira's photospheric temperature and in the dust-envelope optical depth at a constant grain temperature. Solid lines *1* and *2* in Fig. 5 indicate color variations at the Mira's temperatures T_M = 3000 and 2400 K, respectively, and at $\tau(J)$ = 0–3 with a step of 0.5; the grain temperature in the dust envelope is ~600 K. The crosses on model curves *1* and *2* mark the colors corresponding to optical depths from 0 to 3 with a step of 0.5 at 1.25 μm. We see the following in Fig. 5: (a) the observed $J–K$ and $K–L$ color indices for both symbiotic novae, while decreasing, tend to the values typical of Miras; (b) most of the observed color indices lie in the ranges of Mira temperatures from 2400 to 3000 K and of optical depths from 1 to 3 at 1.25 μm; (c) the dust envelopes of both symbiotic novae are optically thick (on the average, the dust envelope around HM Sge is almost twice as dense as that around V1016 Cyg); (d) the Mira in V1016 Cyg is slightly cooler (~2800–2900 K) than that in HM Sge (~2600–2700 K), and the dust-envelope density decreases as the Mira's temperature increases.

If we attribute the observed (corrected for interstellar extinction) monotonic variations in $J–K$ color only to variations in the dust-envelope optical depth and assume its value outside the envelope to be close to $1^m.4$ (see Fig. 5 for the value for Miras), then the Mira's fad-

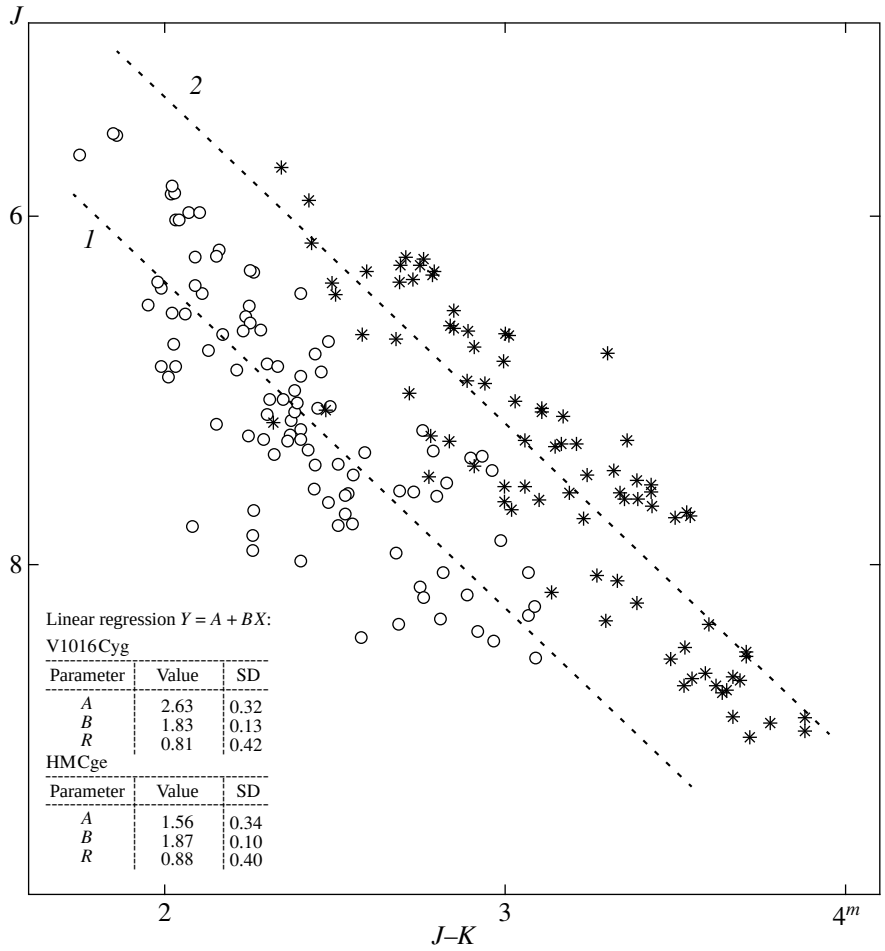

Fig. 3. Color–magnitude diagram for the *JK* photometry of V1016 Cyg and HM Sge in 1978–1999. The observations of V1016 Cyg and HM Sge are indicated by circles and asterisks, respectively; the dashed lines represent the regression lines. Parameters of the regression lines are shown in the lower left corner.

ing in J (and, consequently, at other wavelengths) can be estimated for impure silicates at various phases of the monotonic light and color variations from the relation $A'(J) \approx [(J–K) – 1.4]/0.53$. The number 0.53 in the denominator is the change of $J–K$ as the J brightness declines by $\sim 1^m$ in a dust envelope composed of impure silicates.

We made the subsequent estimates for two intervals of observations of each system. These intervals are given in the first row of Table 2 and are close to the observed minimum and maximum in the monotonic light variations of the symbiotic novae. Table 2 gives $E(B–V)$ taken for the systems under study, the $J–K$ color indices and J magnitudes averaged over the time interval in the first row and their standard errors, as well as $A'(J)/\tau(J)$ and J_0. The total flux from the Mira can be estimated from the J flux outside the envelope, $F_{M,\,tot} = D(J)F(J_0)$, where $F(J_0)$ is the flux from the Mira outside the envelope, and $D(J)$ is the ratio of the Mira's total flux to its J flux; $D(J) \sim 1.72$ at the Mira's photospheric temperature of ~2700 K. We can estimate m_{bol} from the Mira's total flux by using relations from Tsuji (1978) and Glass and Feast (1982) and M_{bol} and, consequently,

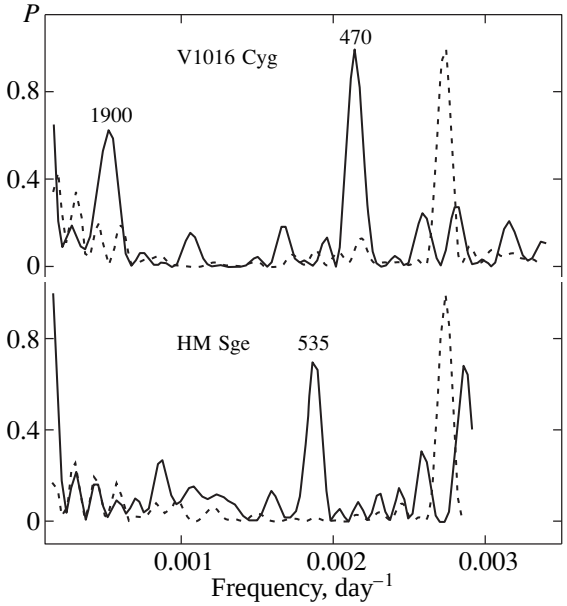

Fig. 4. Power spectra (solid lines) and spectral windows (dotted lines) as constructed from the J photometry for V1016 Cyg and HM Sge. The numbers are the most probable periods (days).

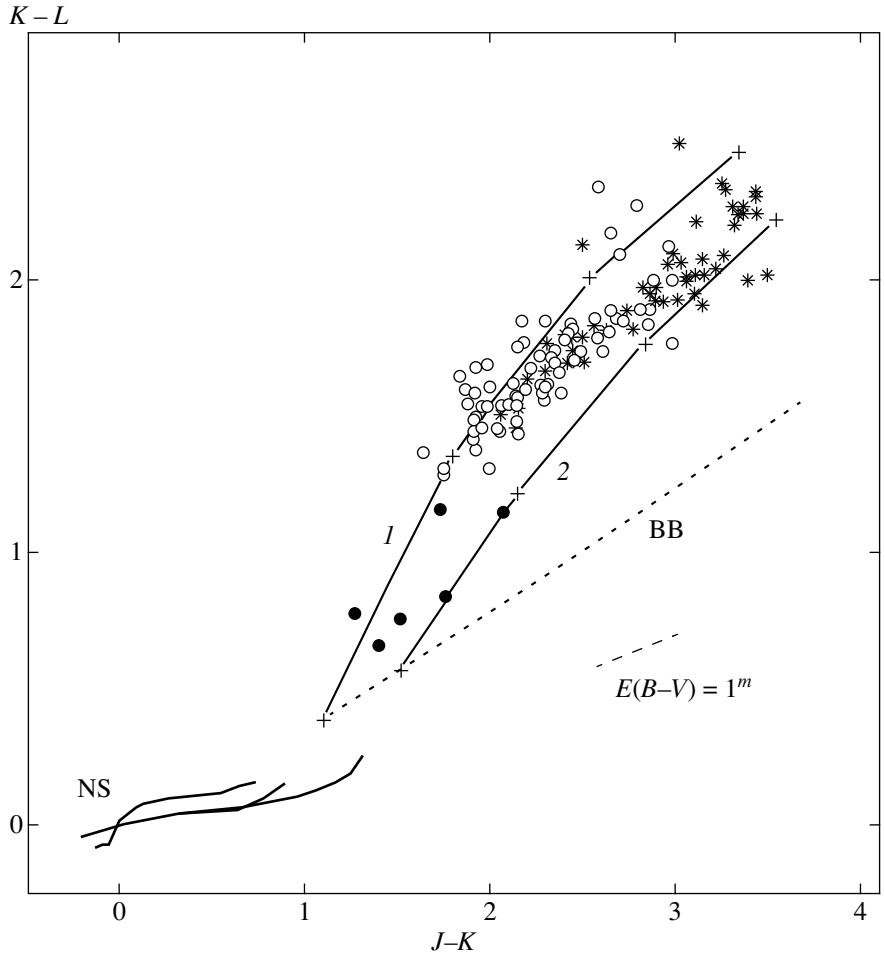

Fig. 5. Infrared color variations of the symbiotic novae V1016 Cyg and HM Sge in the two-color (*J– K*, *K–L*) diagram. The observed colors of V1016 Cyg and HM Sge are indicated by open circles and asterisks, respectively; the solid lines (NS) represent the color variations of normal stars; the dashed line represent the color variations for normal interstellar extinction with $E(B–V) = 1^m$; the dotted line (BB) represents the same for a blackbody; the solid lines (*1, 2*) indicate the color variations of the "star + dust envelope" system (when the envelope optical depth varies and for various temperatures of the cool components); the infrared color variations for the Miras are indicated by filled circles.

the distance to the system *r* (Table 2) from the Mira's pulsation period; for each system, we can then determine the luminosity L_M and radius R_M of their cool components (Miras). Assuming that the photospheric temperatures of the Miras in the systems under study are the same and close to 2700 K and that the temperatures of their dust envelopes are ~600 K (Fig. 5), we can estimate the dust-envelope radii R_d and masses M_d and the rates of mass loss by the dust envelopes during their possible dispersal for the observed monotonic rise in infrared brightness. Our estimates of the above parameters are given in Table 2. We estimated the dust-envelope mass from the relation

$$M_d \approx 4\pi R_d^2 (\rho V_d)(n\Delta R),$$

where $\rho \sim 3$ g cm^{-3} is the density of the dust-envelope matter, $V_d = 4\pi a^3/3$ is the grain volume, and $n\Delta R \approx \tau(\lambda)/Q(\lambda)\pi a^2$, ($a \sim 0.1$ μm is the grain radius).

We then have

$$M_d \sim 16\pi R_d^2 (\rho/3)(a\tau(\lambda)/Q(\lambda)) \approx 4.77 \times 10^{28}\tau(J)$$

for V1016 Cyg

$$\approx 5.47 \times 10^{28}\tau(J) \text{ for HM Sge.}$$

The mass-loss rate was determined by comparing the dust-envelope masses in the first and second intervals of observations.

The data in Table 2 confirm that the symbiotic novae under study are similar, but it may be noted that V1016 Cyg is slower: its infrared brightness rises at a lower rate, and the rate of dispersal of the dust envelope is almost a factor of 25 lower than that for HM Sge.

Table 2. Parameters for the Miras and the dust envelopes in the symbiotic novae V1016 Cyg and HM Sge

Parameter	V1016 Cyg		HM Sge	
JD 2440000+	(4600 ± 190)	(11100 ± 140)	(7200 ± 200)	(11300 ± 150)
$E(B–V)$,^{m}	0.25		0.6	
$J–K$,^{m}	2.20 ± 0.04	2.13 ± 0.03	3.40 ± 0.04	2.37 ± 0.03
J,^{m}	7.5 ± 0.11	6.46 ± 0.10	8.21 ± 0.08	5.97 ± 0.06
$A'(J)/\tau(J)$	1.51/1.39	1.38/1.27	3.77/3.47	1.83/1.68
J_0,^{m}	5.99	5.08	4.44	4.14
$F_{m,\,int}$, W cm^{-2}	2.35×10^{-15}	5.44×10^{-15}	9.82×10^{-15}	12.9×10^{-15}
m_b,^{m}	7.66	6.75	6.11	5.81
$\langle m_b \rangle$,^{m}	7.1		5.95	
M_b,^{m}	–5.1 ± 0.15		–5.27 ± 0.17	
r, kpc	2.8 ± 0.6		1.8 ± 0.4	
L_m, $L_\odot$	8.6×10^3		1×10^4	
R_m, $R_\odot$	500		540	
R_d, $R_\odot$	1.4×10^4		1.5×10^4	
M_d, $M_\odot$	3.31×10^{-5}	3.04×10^{-5}	8.2×10^{-5}	4×10^{-5}
M_d, $M_\odot$ yr^{-1}	1.54×10^{-7}		3.8×10^{-6}	

CONCLUSION

From 1983 until 1999, as before, the near-infrared light and color variations of V1016 Cyg exhibited a periodicity of several hundred days. These periodic variations are grouped into "bunches" of three or four waves, after which a glitch is observed in the periodic variations; subsequently, they are restored. The emergence of a break on the line of sight, which persisted for about three years, can be noted in the system's infrared light and color curves in 1992. Periodic infrared light and color fluctuations on a time scale of several hundred days are also clearly seen in the infrared light and color curves of HM Sge.

Apart from the light and color fluctuations in V1016 Cyg and HM Sge with a period of several hundred days, monotonic light and color variations are observed on a time scale of several thousand days. The monotonic increase in infrared brightness takes place with the simultaneous decrease in infrared color indices; i.e., the dust envelopes in which both components of the systems were embedded before the outburst of the hot source in 1964 and 1975, respectively, had continued to disperse until late 1999. An infrared brightness minimum and the largest reddening of HM Sge were observed in the system's monotonic light and color variations near JD 2447500. The long-term light and color variations of HM Sge and V1016 Cyg are similar in pattern (the decline in the systems' infrared brightness was accompanied by their reddening). In the case of HM Sge, however, the amplitudes of these variations are almost a factor of 2 larger. In addition, if we attribute the monotonic infrared light and color variations of HM Sge and V1016 Cyg to variations in the optical depth of their dust envelopes, which began to expand after the outbursts of the hot sources, then the dust envelope around HM Sge reached a maximum density near JD 2447500 and subsequently began to disperse. For V1016 Cyg, the dust envelope probably reached its maximum density near JD 2444800, and it has been continuing to disperse for about 20 years.

Thus, the dust envelopes in both symbiotic novae reached their maximum density approximately eight years after the outburst of the hot component and then began to disperse.

An analysis of the color–magnitude (J, $J–K$) diagram shows that the grains in the dust envelopes of V1016 Cyg and HM Sge may be similar in their optical properties to impure silicates.

The periods of 470 ± 5 days (for V1016 Cyg) and 535 ± 5 days (for HM Sge) are reliably determined from the entire set of our photometric J data for V1016 Cyg and HM Sge.

The observed [$J–K$, $K–L$] color variations for the symbiotic novae under study can be explained in terms of our simple model by variations in the Mira's photospheric temperature from 2400 to 3000 K and in the dust-envelope optical depth from 1 to 3 at a wavelength of 1.25 μm at constant grain temperature. The observed $J–K$ and $K–L$ color indices for both symbiotic novae, while decreasing, tend to the values typical of Miras.

The dust envelopes of both symbiotic novae are optically thick. On the average, the dust envelope around HM Sge is almost twice as dense as that around V1016 Cyg. The Mira in V1016 Cyg is slightly cooler (~2800–2900 K) than that in HM Sge (~2600–2700 K). The dust-envelope density decreases as the Mira's temperature increases. The absolute bolometric magnitudes are $-5^m.10 \pm 0^m.15$ for V1016 Cyg and $5^m.27 \pm 0^m.17$ for HM Sge, and their distances are 2.8 ± 0.6 and

1.8 ± 0.4 kpc, respectively; the luminosities and radii of their cool components (Miras) are $8.6 \times 10^3 L_\odot$, $1 \times 10^4 L_\odot$, $500 R_\odot$, and $540 R_\odot$, respectively. For photospheric temperatures of the Miras in the systems under study of ~2700 K and for a dust-envelope temperature of ~600 K, the radii of their dust envelopes are $1400 R_\odot$ and $1500 R_\odot$; the masses are $(3–3.3) \times 10^{-5} M_\odot$ and $(4–8) \times 10^{-5} M_\odot$.

Our results confirm that the symbiotic novae under study are similar, but V1016 Cyg is slower: its infrared brightness rises at a lower rate, and the rate of dispersal of its dust envelope is almost a factor of 25 lower than that for HM Sge.

ACKNOWLEDGMENTS

A.M. Tatarnikov and B.F. Yudin took part in the observations. We used the programs by V.M. Lyuty and Yu.K. Kolpakov to determine the variability periods.

REFERENCES

1. O. D. Dokuchaeva and B. Balash, Astron. Tsirk., No. 929 (1975).
2. I. S. Glass and M. W. Feast, Mon. Not. R. Astron. Soc. **199**, 245 (1982).
3. P. M. Harvey, Astrophys. J. **188**, 95 (1974).
4. H. L. Johnson, R. I. Mitchel, B. Iriarte, and W. Z. Wisniewski, Commun. Lunar Planet. Lab. **4**, 99 (1966).
5. T. W. Jones and K. M. Merrill, Astrophys. J. **209**, 509 (1976).
6. J. Koornneef, Astron. Astrophys. **128**, 84 (1983).
7. S. W. McCuskey, IAU Circ., Nos. 1916–1917 (1965).
8. M. Rowan-Robinson and S. Harris, Mon. Not. R. Astron. Soc. **200**, 197 (1982).
9. O. G. Taranova, Pis'ma Astron. Zh. **26**, (2000) (in press) [Astron. Lett. **26** (2000) (in press)].
10. O. G. Taranova and B. F. Yudin, Astron. Astrophys. **117**, 209 (1983).
11. O. G. Taranova and B. F. Yudin, Astron. Zh. **63**, 317 (1986) [Sov. Astron. **30**, 193 (1986)].
12. T. Tsuji, Astron. Astrophys. **62**, 29 (1978).
13. H. M. Schmid, in *Proceedings of the International Conference on Physical Processes in Symbiotic Binaries and Related Systems, Koninki, Poland, 1997*, Ed. by J. Mikolajewska (Copernicus Astronom. Center, Warsaw, 1997), p. 21.
14. B. F. Yudin, Astron. Zh. **71**, 900 (1994) [Astron. Rep. **38**, 801 (1994)].
15. B. Yudin, U. Munari, O. Taranova, and I. Dalmeri, Astron. Astrophys., Suppl. Ser. **105**, 169 (1994).

Translated by V. Astakhov

Astronomy Letters, Vol. 26, No. 9, 2000, pp. 609–617. Translated from Pis'ma v Astronomicheskiĭ Zhurnal, Vol. 26, No. 9, 2000, pp. 705–714.
Original Russian Text Copyright © 2000 by Arkhipova, Ikonnikova, Noskova, Sokol.

UBV Observations of Post-AGB Supergiants and Peculiarities of Their Photometric Variability

V. P. Arkhipova*, N. P. Ikonnikova, R. I. Noskova, and G. V. Sokol

Sternberg Astronomical Institute, Universitetskiĭ pr. 13, Moscow, 119899 Russia

Received February 21, 2000

Abstract—The systematic *UBV* observations of six variable post-AGB supergiants in 1991–1999 are presented. Their variability is analyzed. The coolest stars V1027 Cyg and V354 Lac exhibit bimodal pulsations with variable amplitudes. Apart from pulsations, the hotter stars V887 Her and IRAS 19386+0155 show light variations associated with a stellar wind. A variable stellar wind appears to be mainly responsible for the photometric variations in the still hotter stars SAO 163075 and IRAS 20572+4919. Distinct trends in the yearly mean brightness have been found in three of the six supergiants studied, with the trend amplitude being independent of the spectral range. They are interpreted as the result of dust envelopes composed of large grains with $R = A_V/E(B–V) \geq 7$ becoming optically thin. © *2000 MAIK "Nauka/Interperiodica".*

Key words: *stars—supergiants, variability and evolution*

INTRODUCTION

According to present views (Schoenberner 1983; Bloecker 1995; Vassiliadis and Wood 1994), the post-AGB stars move from right to left in the H–R diagram while crossing an instability strip on this way. In doing so, the star itself simulates the properties of a supergiant, although much of its initial mass has already been lost during the evolution. The rate of evolution depends markedly on the mass that left at the tip of the AGB. Various instability mechanisms, such as pulsations or a stellar wind, can manifest themselves in different places of the H–R diagram. Furthermore, since the post-AGB evolution is shown by theoretical calculations to proceed at constant bolometric luminosity, the star's mean optical brightness and its color indices must exhibit trends associated with variations in the bolometric correction and in the stellar temperature.

In the early 1990s, we initiated a program of search for and study of the variability of post-AGB supergiants, candidates for future planetary nebulae. As a result of its implementation, we found several stars to be photometrically variable: HD 51585 = OY Gem (Arkhipova 1989), IRAS 18095+2704 = V887 Her, SAO 124414 = V1427 Aql, IRAS 19386+0155 (Arkhipova *et al.* 1993), IRAS 20572+4919 (Arkhipova and Ikonnikova 1994), IRAS 18062+2410 = V886 Her (Arkhipova *et al.* 1996) and investigated the pattern of variability in the well-known semiregular variables V1027 Cyg and V354 Lac.

Here, we present our new photometric data obtained in 1994–1999 for four F–K supergiants: V887 Her, V1027 Cyg, V354 Lac, SAO 163075, as well as for two hotter A stars: IRAS 19386+0155 and IRAS 20572+4919. The observations of V1427 Aql will be published in a separate paper in view of the particular interest in its detected variations.

As previously, we carried out our observations at the Crimean Station of the Sternberg Astronomical Institute (SAI) by using the 60-cm reflector equipped with a photoelectric *UBV* photometer. The photometer aperture was 27″ in diameter. The accuracy of *BV* and *U* observations was $\pm 0\overset{m}{.}01$ and $\sim \pm 0\overset{m}{.}03$, respectively at a magnitude fainter than 13^m.

1. V887 Her = IRAS 18095+2704, spectral TYPE F3Ib

The *UBV* observations after 1992 are given in Table 1[1]; the *V* light and *B–V*, *U–B* color curves for the entire period of our observations are shown in Fig. 1. There are a distinct trend of the mean brightness in all photometric bands and light variations within the season. In ten years, the star brightened by $0\overset{m}{.}2$ in *UBV*. There is virtually no trend in *B–V*; *U–B* decreased, on the average, by a mere $0\overset{m}{.}03$, which is comparable to observational errors and cannot be regarded as a certainty. The star's brightening may result from a decrease with time in the optical depth of its dust envelope, which is com-

* E-mail address for contacts: vera@sai.msu.ru

[1] Tables 1–6 are published in electronic form only and are accessible via ftp cdsarc.u-strasbg.fr/pub/cats/J (130.79.128.5) or at http://cdsweb.u-strasbg.fr/pub/cats/J.

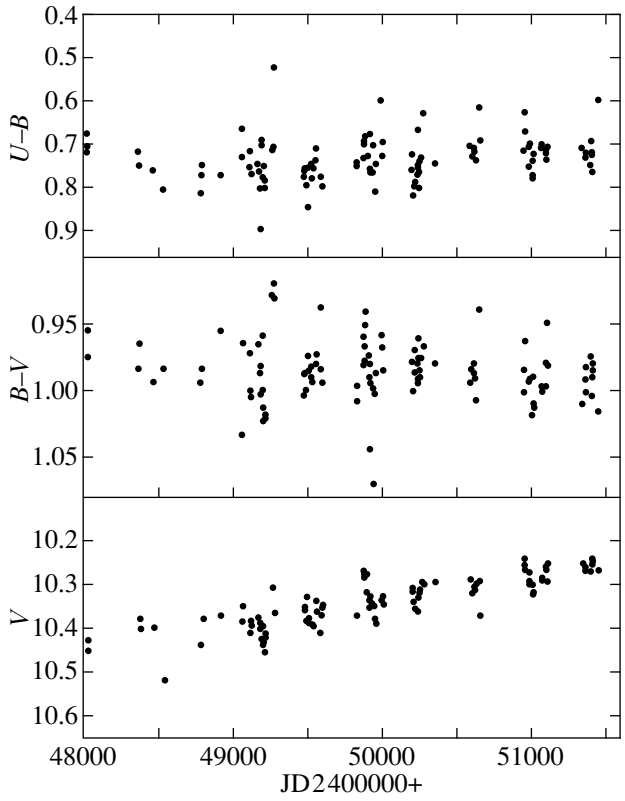

Fig. 1. Light and color variations in V887 Her.

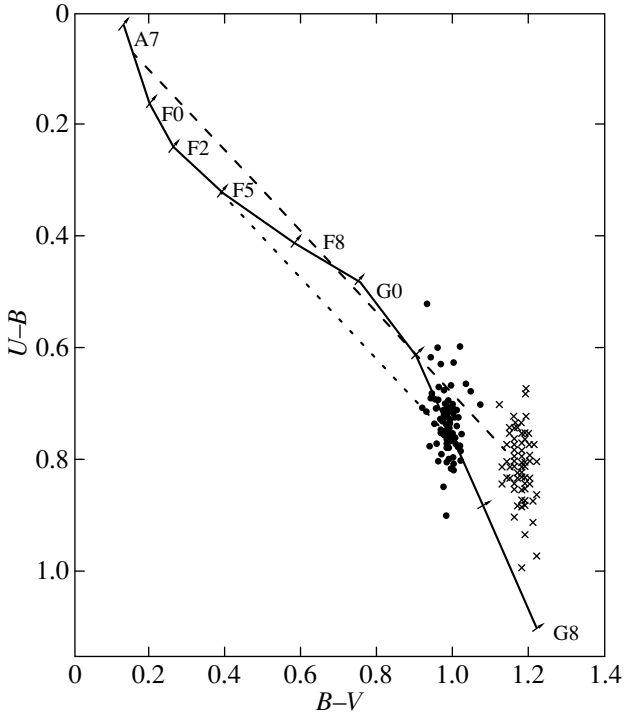

Fig. 2. V887 Her (dots) and IRAS 19386+0155 (crosses) in the two-color diagram. The solid line represents the normal colors of I supergiants, as inferred by Straizis (1977); the dashed lines represent the interstellar reddening law of Whitford (1958).

posed of sufficiently large grains with $R_d = A_d(V)/E_d(B–V) \geq 7$ for the color change to be unnoticeable at $\Delta V = 0\overset{m}{.}2$. The fact that the brightening amplitude is wavelength-independent does not allow the observed trend to be interpreted as the result of binary nature or evolution.

In the two-color *U–B*, *B–V* diagram (Fig. 2), the star moves almost vertically as its light fluctuates. This is cased by the *U* variations attributable to variations in the Balmer-continuum intensity. Tamura and Takeuti (1991) found the Hα line in the spectrum of V887 Her to have an emission component. The rapid photometric variability and the vertical track in the two-color diagram can then be naturally interpreted as the result of stellar-wind mass-loss rate variations.

An analysis of the observed light variations for periodicity after the trend has been subtracted reveals two periods, $P_1 = 99$ days and $P_0 = 152$ days; their statistical significance is not very high, though, which may be because the light curves are covered inadequately with observations. The pulsation-frequency ratio 0.65 is close to the theoretical ratio of the fundamental frequency to the first overtone. We analyzed the periodicity by using the program developed by Yu.K. Kolpakov at the SAI. In Fig. 3, the *B* observations are folded with the two detected periods. The scatter of points at each phase is apparently also attributable to the effect of a variable stellar wind. The color–magnitude diagrams show no clear correlation between the magnitudes, which suggests once again that there are two mechanisms of brightness instability: pulsations and a stellar wind.

Radial-velocity measurements for V887 Her revealed a period of 109 days (Hrivnak 1997). Our photometric data do not agree with this period.

We also investigated the photometric behavior of V887 Her in the past by using data of the SAI sky patrol and known sky atlases. Using the Palomar atlas (its plates were taken in 1951 and 1954), we estimated the star's magnitude to be $m_{pg} = 11\overset{m}{.}85$, on the average. Yet another photographic magnitude estimate, $m_{pg} = 11\overset{m}{.}7$, was obtained in 1968 from a map in the atlas of Vehrenberg (1970). Using a collection of SAI sky patrol plates, we measured the star's magnitude for the period between 1939 and 1994. The estimates were made relative to stars in the V887 Her field, whose *B* magnitudes were determined with the *UBV* photometer. Figure 4 shows the photographic light curve constructed from our plate measurements and the above atlases. Also shown in the figure are our photoelectric *B* magnitudes of V887 Her averaged over each observing season from 1990 until 1999 and the *B* magnitude estimate obtained by Hrivnak *et al.* (1988) in 1987. A trend in brightness clearly shows up over 60 years. Without information about color variations over this entire period, we attribute its origin, as was said above, to a decrease with

time in the optical depth of the dust envelope around the star.

2. IRAS 19386+0155, spectral TYPE A7 Ia

The *UBV* observations after 1992 are given in Table 2; the light and color curves are shown in Fig. 5. As in the case of V887 Her, the yearly mean brightness of the star has a trend exhibiting a brightening, which, however, by contrast to V887 Her, is nonmonotonic. In ten years, the star brightened by $0\overset{m}{.}2$ in *UBV*. No trend in its colors has been found. Light variations with an amplitude up to $0\overset{m}{.}2$ in *V* are observed within each season.

The star's behavior in the two-color *U–B*, *B–V* diagram (Fig. 2) is identical to that of V887 Her. There is an ultraviolet excess pointing to the presence of an extended envelope or a stellar wind with Balmer-continuum radiation. The color–magnitude diagrams show no correlation between the magnitudes.

An analysis of the fluctuations for periodicity after the trend has been removed reveals the only period P = 98.76 days with a high significance. The phase *B* light curve with this period is shown in Fig. 6.

The observed trend in brightness can be interpreted in a similar way as that for V887 Her; i.e., a change with time in the optical depth of the surrounding dust envelope causes the star to brighten. In that case, dust grains must absorb less selectively than do interstellar ones at optical wavelengths; i.e., the extinction law in the circumstellar envelope is characterized by a large *R*.

3. V1027 Cyg = IRAS 20004+2955 = HDE 333385 = BD+29°3865, spectral TYPE G7 Iab

The *UBV* observations after 1996 are given in Table 3; the light and color curves since 1991 are shown in Fig. 7. The previous observations were published by Arkhipova *et al.* (1993, 1997). The light curve exhibits deep and shallow minima with a different color–magnitude relation, as we noted above: at shallow minima the star reddens as it fades, while at deep minima its color indices begin to decrease as the star fades further starting from some brightness level. *UBV* data are presently available for ten photometric minima of the star. Figure 8 shows the *U–B*, *V* diagram to illustrate the aforesaid. Another protoplanetary candidate, V354 Lac, whose observations are discussed below, exhibits a similar pattern.

In the two-color *U–B*, *B–V* diagram (Fig. 9), the direction of change in the colors of V1027 Cyg during its light variations does not coincide with the line of normal colors for supergiants and is inclined to it more steeply. This may result from the presence of an ultraviolet excess, which shows up as the star fades sufficiently and which represents the Balmer-continuum emission from its extended envelope. The star's ambiguous behavior in the color–magnitude diagram can then also be explained. Under the assumption of a normal reddening law, the color excess is $E(B–V)$ = 0.6 if the normal color of a K5 I supergiant is taken for V1027 Cyg. The interstellar extinction in this direction is considerable, and the star's entire color excess may be attributable to interstellar reddening.

We analyzed our observations of V1027 Cyg for periodicity. The frequency corresponding to the period P_0 = 306 days is distinguished with the highest signifi-

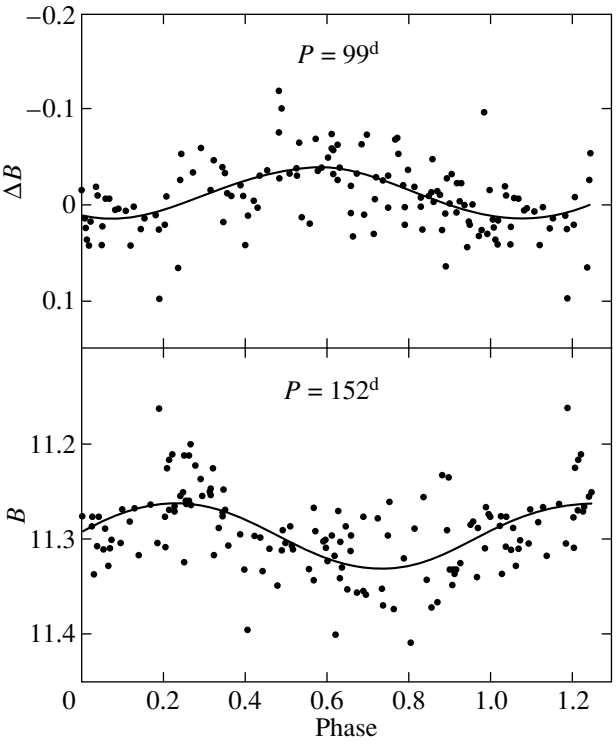

Fig. 3. The phase light curves of V887 Her for two periods: P_0 = 152d and, after its subtraction, P_1 = 99d.

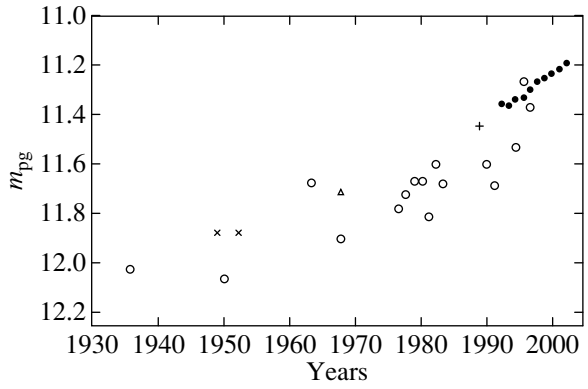

Fig. 4. The photographic light curve of V887 Her (the circles, triangles, and crosses denote the estimates from SAI plates, Vehrenberg's atlas, and the Palomar Atlas, respectively). The dots represent the yearly mean photoelectric *B* magnitudes, and the plus represents the *B* magnitude from Hrivnak *et al.* (1988).

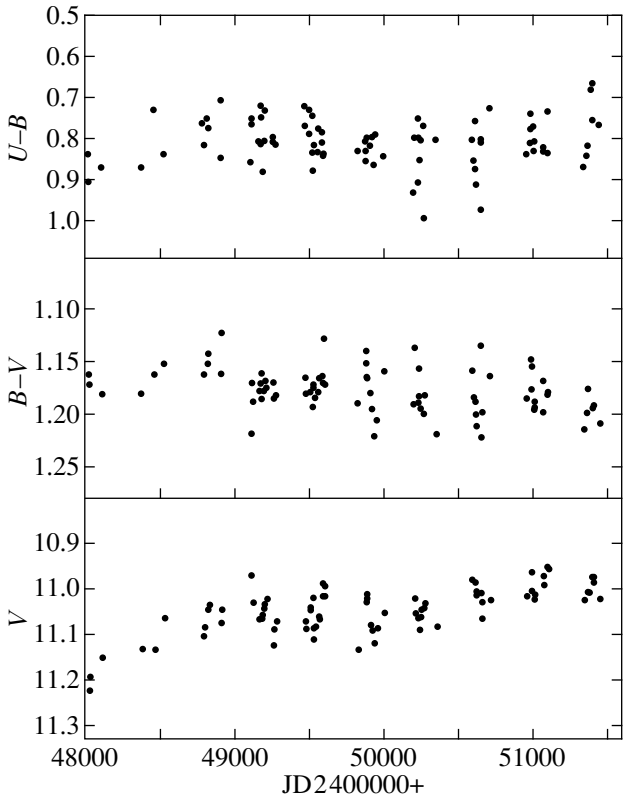

Fig. 5. The light and color curves for IRAS 19386+0155.

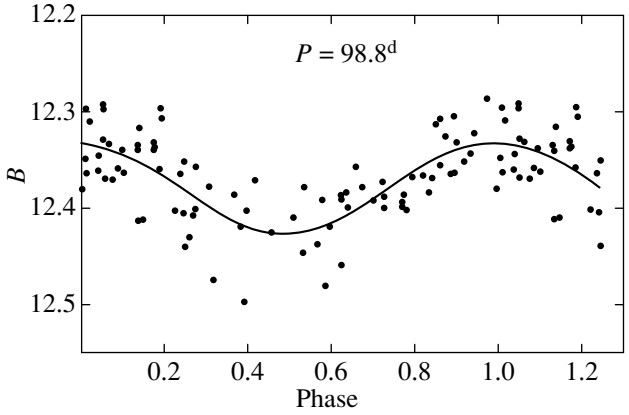

Fig. 6. The observations of IRAS 19386+0155 folded with $P = 98^{\rm d}.8$.

cance. Another period, P_1 = 225 days, was found after the average curve with this period had been subtracted. The ratio of their frequencies is 0.73, which corresponds to the ratio of the first-overtone period to the fundamental one. The phase *V* light curves for each period are shown in Fig. 10. We see that the shape of the fluctuations and their amplitude change from cycle to cycle. Nevertheless, the bimodal pattern of the stellar pulsations is beyond question. Previously (Arkhipova *et al.* 1997), we attempted to represent our photometric observations by a single period of ~250 days and noted large O–C values for several epochs; now these difficulties are completely eliminated.

4. V354 Lac = IRAS 22272+5435 = BD+54°2787 = HDE 235858 = SAO 34504, spectral TYPE GpIa, K5 (HDE)

The *UBV* observations since 1993 are given in Table 4; the light and color curves since 1991 are shown in Fig. 11. The number of observations is not large, but the star's salient photometric features are clearly revealed. In the two-color *U–B*, *B–V* diagram (Fig. 9), the star's behavior is similar to that of V1027 Cyg, but the color–magnitude diagrams, as in the case of V1017 Cyg, exhibit an ambiguous relationship between the magnitudes. We are inclined to suggest that, in the case of V354 Lac, the ultraviolet excess, which is produced by an extended gas envelope around the star and which shows up more clearly as the photospheric brightness declines, is also responsible for this ambiguity.

Our analysis of the photometric data for periodicity revealed two frequencies whose ratio is 0.70. In Fig. 12, the observations are folded with the most significant period P_0 = 207 days and, after the average curve of the fundamental pulsation has been subtracted, the residuals are represented by the first-overtone period P_1 = 145 days. The star clearly has two pulsation modes, with the shape and amplitude of the light curves being markedly unstable. Here, there is also a close similarity to V1027 Cyg.

The color excess $E(B–V)$ is estimated from the two-color diagram to be 0.4 and may be attributable to interstellar reddening, because the star lies at a low Galactic latitude.

Based on the star's radial-velocity measurements in 1994–1996, Hrivnak (1997) found *P* = 127 days for V354 Lac. Our 1994–1996 photometric data are consistent with this period.

5. SAO 163075 = IRAS 19500–1709 = HD 187885 = BD–17°5779, spectral TYPE F3Iab (Parthasarathy *et al.* 1988), A2–3 I, F8 (HD)

We began our *UBV* observations of the star (Table 5) in 1993. The comparison star is BD–17°5778, whose photometric data ($V = 9^{m}.97$, $B–V = +0^{m}.62$, and $U–B = +0^{m}.11$) were obtained by referencing to Johnson's *UBV* standards. The light and color curves are shown in Fig. 13. The variability amplitude does not exceed $0^{m}.3$ in *V* and $0^{m}.15$ for the color indices. The trends in *V* brightness and color are indistinct, except for 1999 when the star faded by almost $0^{m}.1$, on the average, while its *B–V* increased approximately by $0^{m}.05$. In the *B* and *U* bands, the fading in 1999 was more pronounced. There is virtually no correlation between the

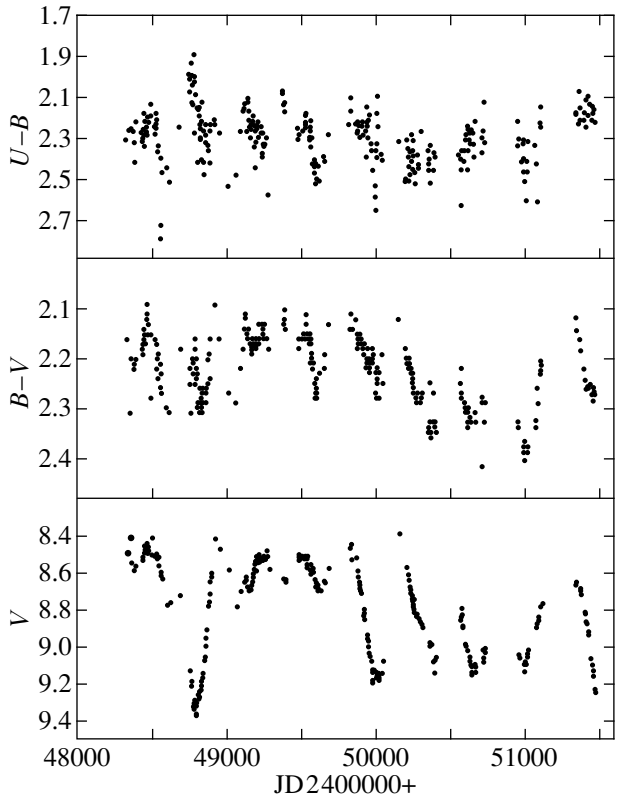

Fig. 7. The light and color curves for V1027 Cyg.

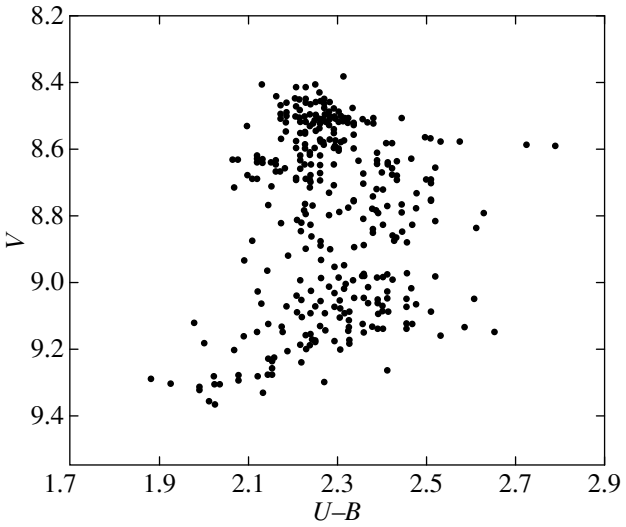

Fig. 8. The behavior of V1027 Cyg in the *U–B, V* diagram.

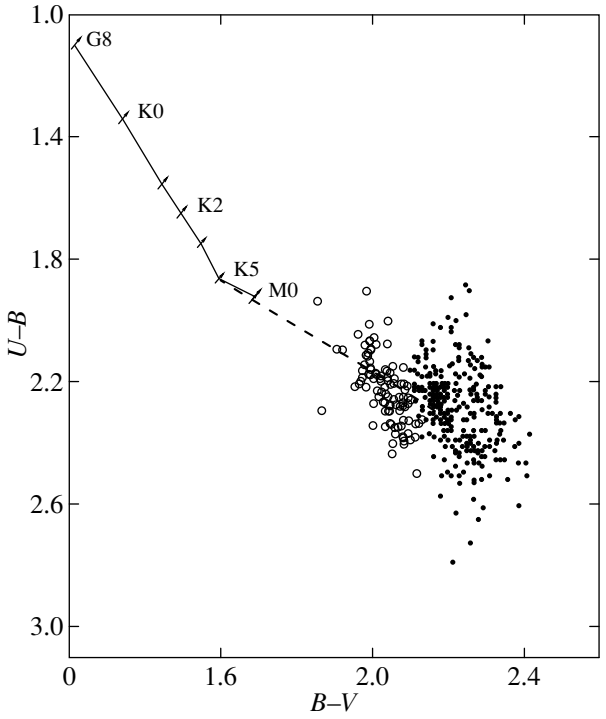

Fig. 9. V1027 Cyg (dots) and V354 Lac (circles) in the *U–B, B–V* diagram. The solid line represents the normal colors of supergiants; the dashed line represents the normal interstellar reddening law.

colors and between the light and color. The star's position in the two-color *U–B*, *B–V* diagram is shown in Fig. 14.

Our search for periodicity in *U* revealed three distinct frequencies corresponding to periods of 97.39, 53.12, and 34.89 days, but their significance is not very high. The ratio of the first two frequencies is close to a theoretical ratio of the second overtone and the fundamental pulsation. Pulsations at higher overtones may also be generated in post-AGB stars as they move into the region of hotter stars; as a result, the pulsations become increasingly erratic.

The causes of the longer term photometric variability in SAO 163075 are rather unclear and require further observations. However, it is most likely related to a variable stellar wind. Particular attention should be paid to the significant discrepancy between current estimates of the star's spectral type and those from the HD catalog.

6. IRAS 20572+4919, spectral TYPE A3 I

Our first observations of the star were carried out in 1993 (Arkhipova and Ikonnikova 1994). The *UBV* data obtained in 1994–1999 are given in Table 6; the *V* light and *B–V*, *U–B* color curves are shown in Fig. 15. The variability amplitude is $\sim 0\overset{m}{.}2$ in *V* and *B* and $\sim 0\overset{m}{.}3$ in *U*. A small trend shows up in *B* and *U*; it is less distinct in *V* and in *U–B*. In seven years, the star brightened approximately by $0\overset{m}{.}1$ in *V* and *B* and by $0\overset{m}{.}2$ in *U* and became bluer by a few hundredths of a magnitude. These values are not very significant because of the few observations in each season; rather there is a tendency for the brightness to rise. By contrast to V887 Her and IRAS 19386+0155, the degree of brightening depends on wavelength.

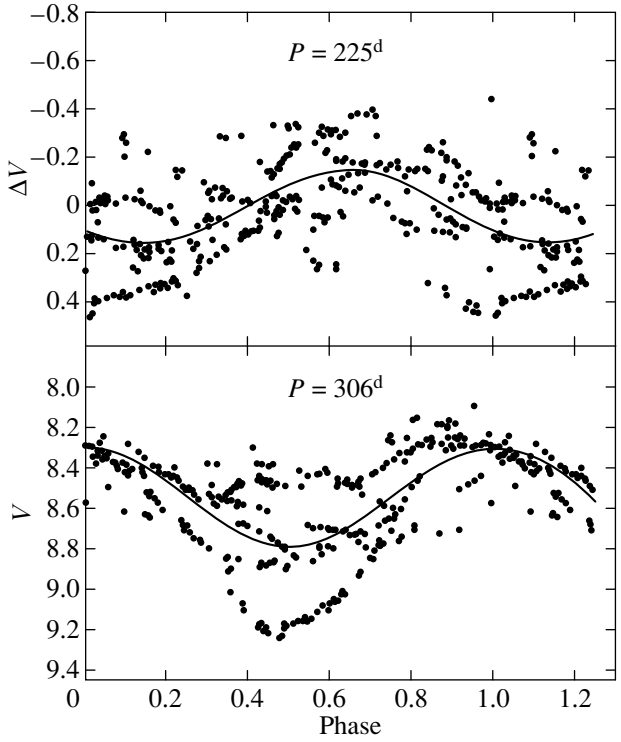

Fig. 10. The phase light curves of V1027 Cyg for $P_0 = 306^d$ and $P_1 = 225^d$.

If the trend in brightness is statistically significant rather than associated with the time distribution of observations, then, as in the case of V887 Her and IRAS 19386+0155, the observed trend in brightness and color can be interpreted as the result of a dust envelope composed of fairly large grains with $R > 3$ becoming optically thin. In that case, part of the color excess may result from circumstellar reddening.

Previously, we estimated an upper limit on the star's spectral type from the *UBV* data of Wisniewski and Coyne (1976) to be a late B supergiant of luminosity class II, although our scarce *UBV* data pointed to a later spectral type. Presently, the photometric data strongly suggest the spectral type A rather than B.

The star's position in the two-color *U–B*, *B–V* diagram (Fig. 14) points to a substantial color excess, irrespective of *R*. In addition, as in the case of V887 Her, the light variations have a larger amplitude in *U–B*, suggesting the presence of a stellar wind.

Since our search for periodicity in the light variations of IRAS 20572+4919 revealed no significant frequencies, they can be classified as random. There is no correlation between the color and magnitude in them; therefore, a variable stellar wind may be suggested as a probable cause of these fluctuations.

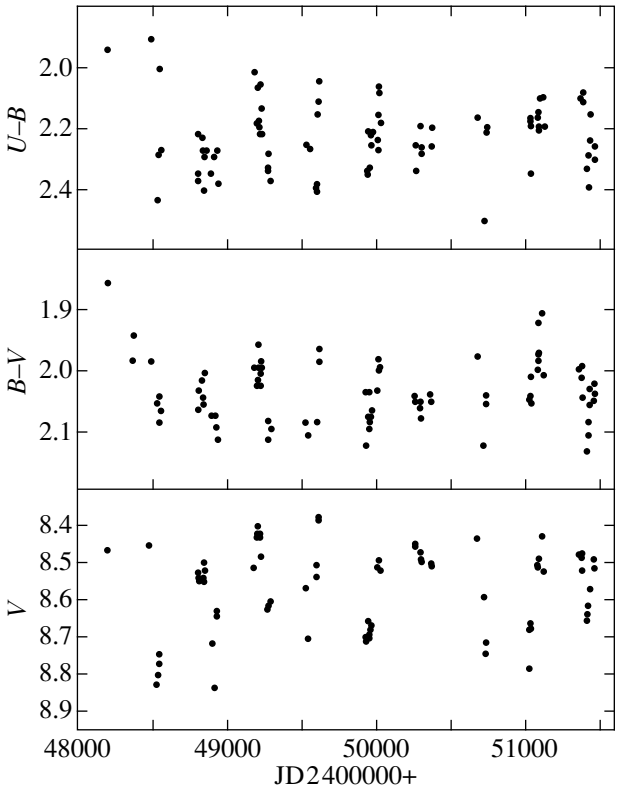

Fig. 11. Light and color variations in V354 Lac.

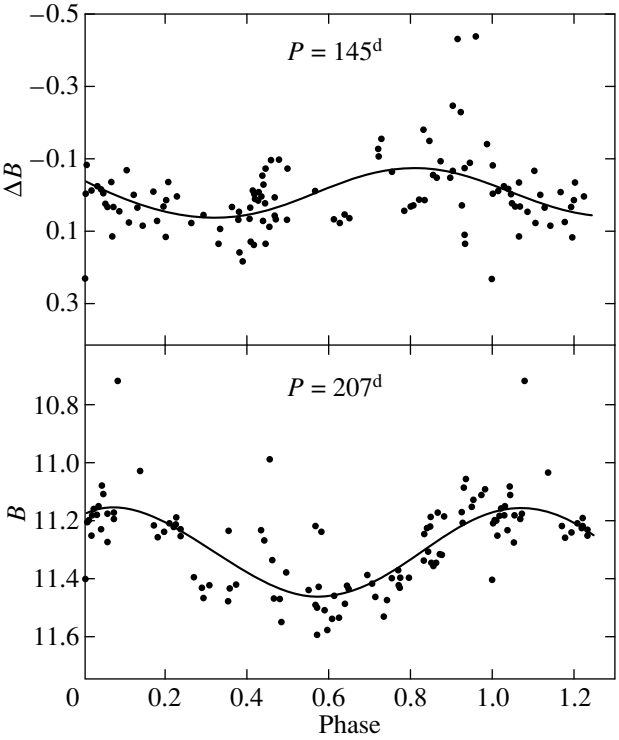

Fig. 12. The phase light curves of V354 Lac with $P_0 = 207^d$ and $P_1 = 145^d$.

DISCUSSION

Here, we have investigated stars of various spectral types, which are classified by various criteria as probable progenitors of planetary nebulae. They lie at different points of the post-AGB evolutionary track: the cooler stars V1027 Cyg and V354 Lac are just beginning their motion to the left, whereas the remaining ones are at a more advanced evolutionary stage.

The systematic photometric observations of eight supergiants over ten years of our monitoring have revealed several types of variability in these objects.

First, they all exhibit light variations with amplitudes from several tenths of a magnitude to several magnitudes. The coolest stars have the largest amplitudes, up to one magnitude or more, with both representatives (V1027 Cyg and V354 Lac) pulsating at two frequencies whose ratio is close to 0.7. The color indices vary mainly in phase with the brightness, being smallest at maximum. Although the shape and amplitude of each pulsation are unstable, the bimodal pattern of the pulsations is beyond question. We identify the detected frequencies with the fundamental period and the first overtone. Both pulsations appear to be unstable, and their amplitude ratio can vary significantly with time. Note also that SAO 124414, a protoplanetary candidate of spectral type F5 Ia (Arkhipova *et al.* 2000), also exhibits bimodal pulsations with the periods $P_0 = 204$ days and $P_1 = 142$ days and with the pulsation amplitudes $\Delta V = 0\overset{m}{.}1$, $\Delta B = 0\overset{m}{.}15$, and $\Delta U = 0\overset{m}{.}25$.

The amplitudes of the hotter F supergiants V887 Her and IRAS 19386+0155 are a few tenths of a magnitude. A periodicity analysis revealed two periods, 99 and 152 days, in the former star and only one period, 99 days, in the latter star. It can be assumed that, as the post-AGB stars evolve along the horizontal track to the left in the H–R diagram, their pulsations are switched to higher and unstable modes; therefore, both the multifrequency pattern of pulsations and the dominance of a single frequency during some time may show up. In particular, IRAS 19386+0155 may have pulsated during our observations in the first overtone.

The light variations in the still hotter A stars SAO 163075 and IRAS 20572+4919 exhibit an indistinct periodicity. We noted the multi-frequency pattern of pulsations in SAO 163075, but the significance of the periodogram peaks is not high. There are no significant frequencies in the light variations of IRAS 20572+4919 either. The photometric variability of both stars is stochastic in nature, and the most characteristic feature is a more noticeable pulsation amplitude in *U*. The latter is a manifestation of a different mechanism of photometric variability in the supergiants studied—the stellar wind typical of hotter post-AGB stars.

Noteworthy in this connection are our observations of the post-AGB B supergiant V886 Her (Arkhipova *et al.* 1999a), whose rapid irregular light variations

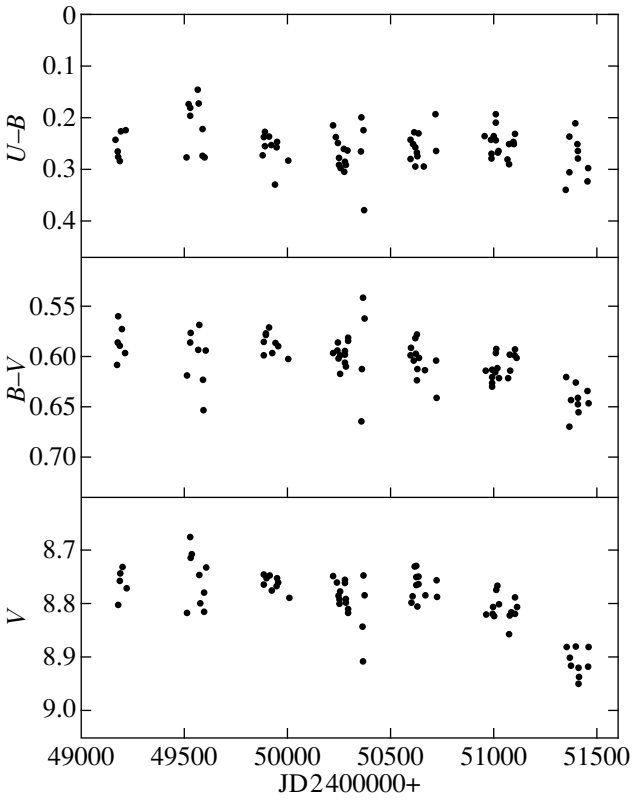

Fig. 13. The light and color curves for SAO 163075.

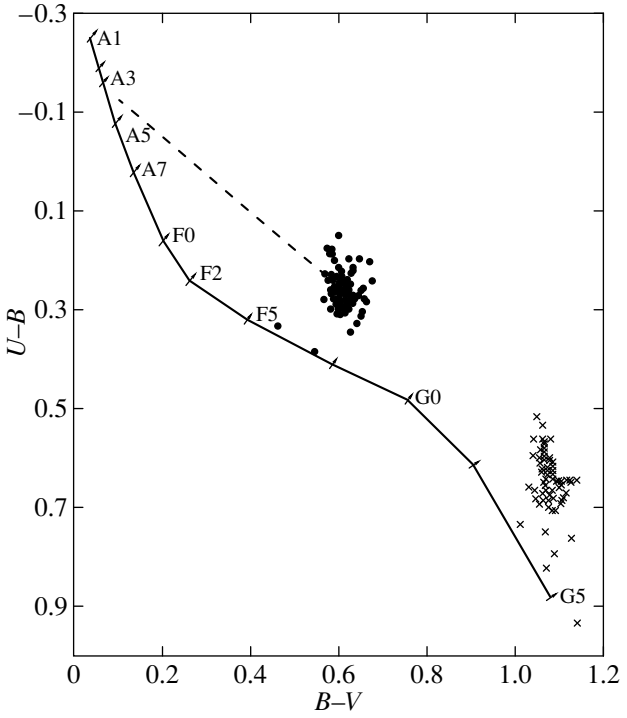

Fig. 14. SAO 163075 (dots) and IRAS 20572+4918 (crosses) in the *U–B*, *B–V* diagram. The solid line represents the normal colors of I supergiants; the dashed line represents the normal interstellar reddening law.

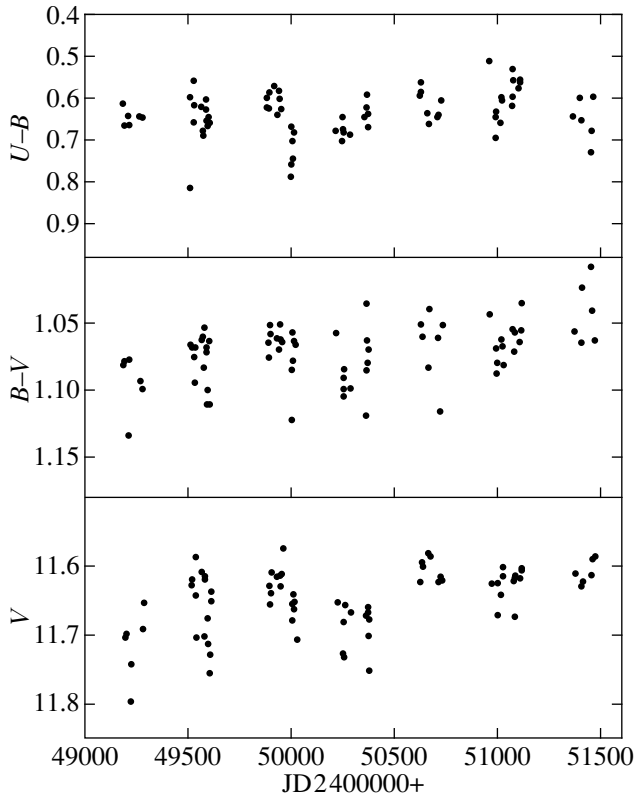

Fig. 15. The light and color curves for IRAS 20572+4919.

were interpreted as the result of variations in $\dot{M}$. A variable stellar wind is probably also mainly responsible for the variability of OY Gem (Arkhipova and Ikonnikova 1992), an essentially very young planetary nebula.

The wind-related photometric variability does not exceed $0^m.1$–$0^m.2$ and shows up more clearly in *U*, because the stellar-wind radiation is more effective in the hydrogen continuum. The cooler post-AGB stars are highly likely to also have a wind, but it is lost against the background of pulsations, and it is difficult to distinguish. In particular, the color track in the two-color *U–B*, *B–V* diagram for all the six observed supergiants deviates from the temperature track toward the presence of an additional ultraviolet excess associated with the gas continuum. For the hotter stars, the mechanism of variability attributable to a stellar wind becomes dominant, because the pulsation mechanism is weakened.

Our photometric observations suggest that there is yet another cause of the photometric variability in post-AGB stars. We detected trends in brightness in three stars, V887 Her, IRAS 19386+0155, and IRAS 20572+4919, pointing to a rise in the star's brightness; the seasonally average color indices have been virtually constant for ten years. Since the stars are surrounded by dust envelopes, it was natural to attribute the brightness rise to a decrease of the dust optical depth in *UBV*. The estimated color excesses (see the Appendix) strongly suggest a large extinction ($A_V > 3^m$) in the dust envelopes of these stars. We estimated R_d in the dust envelope, which characterizes the degree of selectivity of the extinction law in it. Since we obtained $R_d \geq 7$ for all three stars, the dust grains must be fairly large.

The decrease in the envelope optical depth shows up differently. The brightness of V887 Her in the blue has systematically risen for 60 years. Since we have no information about the star's color behavior or about its spectral type in the past, we have to explain this prolonged trend by the dust becoming optically thin rather than assume this to be a rapid evolution along the post-AGB track, as we did for V886 Her (Arkhipova *et al.* 1999a). The stars IRAS 19386+0155 and IRAS 20572+4919 may have temporary trends in brightness, which need confirmation on longer time scales.

SAO 124414 (V1427 Aql) also exhibits a trend in brightness and color, but it is more probably associated with variations in the stellar temperature. A rapid evolution is most likely responsible for the temperature trend (Arkhipova *et al.* 2000).

By contrast to the hotter supergiants considered above, V1027 Cyg and V354 Lac showed no trends in brightness and color throughout the history of their observations, and, in all probability, their dust envelopes contribute only slightly to the observed color excess.

As was already mentioned above, a rapid evolution along the horizontal track in the H–R diagram may be responsible for the brightness trend of a star at the stage of a post-AGB supergiant. In this case, the star's temperature and colors must rapidly vary, while the *V* light curve will represent variations of the bolometric correction with time. The only example we know is V886 Her, which has passed from an F star to an early B star in 150 years. Another example is the well-known variable and the planetary-nebula nucleus FG Sge, which has traversed the path along the horizontal track (though in the opposite direction because of the helium shell flash) from a very hot star to a carbon C3 star (Arkhipova *et al.* 1999b).

ACKNOWLEDGMENTS

We wish to thank S.Yu. Shugarov and G.V. Zaitseva, who took part in the observations.

REFERENCES

1. V. P. Arkhipova, Pis'ma Astron. Zh. **15**, 925 (1989) [Sov. Astron. Lett. **15**, 400 (1989)].
2. V. P. Arkhipova and N. P. Ikonnikova, Pis'ma Astron. Zh. **18**, 1017 (1992) [Sov. Astron. Lett. **18**, 418 (1992)].
3. V. P. Arkhipova and N. P. Ikonnikova, Pis'ma Astron. Zh. **20**, 700 (1994) [Astron. Lett. **20**, 603 (1994)].
4. V. P. Arkhipova, N. P. Ikonnikova, and R. I. Noskova, Pis'ma Astron. Zh. **19**, 436 (1993) [Astron. Lett. **19**, 169 (1993)].

5. V. P. Arkhipova, N. P. Ikonnikova, V. F. Esipov, and R. I. Noskova, Pis'ma Astron. Zh. **22**, 379 (1996) [Astron. Lett. **22**, 470 (1996)].
6. V. P. Arkhipova, V. F. Esipov, N. P. Ikonnikova, *et al.*, Pis'ma Astron. Zh. **23**, 794 (1997) [Astron. Lett. **23**, 690 (1997)].
7. V. P. Arkhipova, N. P. Ikonnikova, R. I. Noskova, *et al.*, Pis'ma Astron. Zh. **25**, 30 (1999a) [Astron. Lett. **25**, 25 (1999)].
8. V. P. Arkhipova, V. F. Esipov, G. V. Sokol, and S. Yu. Shugarov, Pis'ma Astron. Zh. **25**, 849 (1999b) [Astron. Lett. **25**, 739 (1999)].
9. V. P. Arkhipova *et al.*, Pis'ma Astron. Zh. (2000) (in press) [Astron. Lett. (2000) (in press)].
10. M. Asplund, B. Gustafsson, D. Kiselman, and K. Eriksson, Astron. Astrophys. **318**, 521 (1997).
11. T. Bloecker, Astron. Astrophys. **297**, 727 (1995).
12. B. J. Hrivnak, in *Proceedings of the 180th IAU Symposium on Planetary Nebulae, 1997*, Ed. by B. J. Habing and H. J. G. L. M. Lamers (Kluwer, Dordrecht, 1997), p. 303.
13. B. J. Hrivnak, S. Kwok, and K. M. Volk, Astrophys. J. **331**, 832 (1988).
14. K. Nandy and N. C. Wickramasinghe, Mon. Not. R. Astron. Soc. **154**, 255 (1971).
15. M. Parthasarathy, S. R. Pottasch, and W. Wamsteker, Astron. Astrophys. **203**, 117 (1988).
16. D. Schoenberner, Astrophys. J. **272**, 708 (1983).
17. V. P. Straĭzhis, *Multicolor Stellar Photometry* (Mokslas, Vilnius, 1977).
18. S. Tamura and M. Takeuti, Inf. Bull. Var. Stars, No. 3561, 1 (1991).
19. E. Vassiliadis and P. R. Wood, Astrophys. J., Suppl. Ser. **92**, 125 (1994).
20. H. Vehrenberg, *Atlas Stellarum* (Treugesell.–Verlag. KG, 1970).
21. W. Wisniewski and G. V. Coyne, Vatican Obs. Publ. **1**, 245 (1976).
22. A. E. Whitford, Astron. J. **63**, 201 (1958).

APPENDIX

Calculating the Color Excesses of Stars in the Case of a Nonstandard Extinction Law in Their Dust Envelopes

When a circumstellar dust envelope contains larger grains than those in the ordinary interstellar medium, the reddening law and the total-to-selective absorption ratio R differ from the standard ones. In the interstellar medium, the normal reddening law of Whitford (1958) with the mean $R = A_V/E(B–V) = 3.3$ and $E(U–B)/E(B–V) = 0.72$ is applied in most Galactic regions. These parameters slightly depend on the extinction and spectral energy distribution of the stars. A photometric determination of the spectral type from a two-color diagram assumes that the observational data are moved along the reddening line until intersection with the corresponding line of normal colors.

When R in the dust is considerably larger than its normal value, the color-excess ratio (the slope of the reddening line) also differs from 0.72. For the Orion Nebula with $R \approx 6–7$, we obtained $E(U–B)/E(B–V) = 0.46$ by using the extinction curve constructed by Nandy and Wickramasinghe (1971). The slope of the circumstellar reddening line at such R turned out to be considerably gentler than that of the interstellar reddening line. When the two different reddening laws (the unavoidable interstellar and circumstellar ones) operate simultaneously, the direction of motion of the point representing the observations is determined by the resultant of the corresponding vectors in the two-color diagram. If the normal color of a star is known and if an independent estimate is available for the interstellar reddening, then the circumstellar color excess and the total extinction in its dust envelope can be determined. However, there are large discrepancies between the spectral types estimated by different authors for most of the post-AGB stars we studied. In addition, possible chemical anomalies, notably a hydrogen underabundance, affect significantly the spectral energy distribution. As a result, the normal color of a star remains uncertain, preventing a reliable estimation of both the total and circumstellar color excesses even if an independent estimate of the interstellar reddening is available. For this reason, we provide no estimates of $E(B–V)$ for V887 Her, IRAS 19386+0155, and IRAS 20572+4919, although the positions of these stars in the two-color $U–B$, $B–V$ diagram and the interstellar color excess $E(B–V)$ estimated from neighboring stars (small in all cases, which is attributable to their appreciable Galactic latitude) point to a considerable circumstellar reddening and, accordingly, extinction in their dust envelopes. Note that a hydrogen underabundance makes the normal colors $(U–B)_0$ and $(B–V)_0$ increasingly red, as the calculations by Asplund *et al.* (1997) show.

Translated by V. Astakhov

Astronomy Letters, Vol. 26, No. 9, 2000, pp. 618–620. Translated from Pis'ma v Astronomicheskiĭ Zhurnal, Vol. 26, No. 9, 2000, pp. 715–718.
Original Russian Text Copyright © 2000 by Mikisha, Rykhlova, Smirnov.

Effects of a Micrometeorite Stream on the Accuracy of Astrometric Measurements by Scanning Space-Borne Instruments

A. M. Mikisha, L.V. Rykhlova*, and M. A. Smirnov

Institute of Astronomy, Russian Academy of Sciences, Pyatnitskaya ul. 48, Moscow, 109017 Russia

Received November 12, 1999; in final form, March 30, 2000

Abstract—The effect of micrometeorite impacts upon the surface of a spacecraft on the accuracy of astrometric measurements made by scanning with instruments onboard the spacecraft is considered. This effect is shown to be marginal for HIPPARCOS measurements. However, disregarding this kind of effect for all the currently projected spacecraft may result in the declared measurement accuracy being unachievable. Spacecraft maintaining constant spatial orientation during measurements are essentially not subject to the errors caused by collisions with micrometeorites. © *2000 MAIK "Nauka/Interperiodica".*

Key words: *astronomical observing techniques, instruments; Solar system—planets, comets, asteroids, heliosphere*

INTRODUCTION

The late 1980s to the early 1990s saw a remarkable event—successful realization of the HIPPARCOS project (Perryman *et al.*, 1989)—which proved great advantage of using space-borne astrometric instruments and, in essence, determined today's prospects for developing astrometry. The HIPPARCOS satellite was launched in 1989 and completed its mission in 1992, having measured positions of about 120 000 stars with an accuracy of 0.7 arc milliseconds. The main result of this mission is the HIPPARCOS and TYCHO catalogs (Perryman *et al.*, 1997), which are now intensively used in different areas of astronomy, astrophysics, geodynamics, etc. However, the HIPPARCOS project did not permit the determination of proper stellar motions with accuracy sufficient for maintaining the coordinate system over long time intervals. To maintain the achieved precision of the HIPPARCOS catalog, additional observations of astronomical objects are thus required because of changing their positions in the course of time. This issue can be partially solved by means of observations with ground-based interferometers and traditional meridian circles equipped by the matrix detectors operating in the automatic mode.

The success of the HIPPARCOS mission stimulated the statement of new tasks with the proviso that a higher level of measurement accuracy is attained. After the completion of the HIPPARCOS project, space agencies in various countries put forward a series of astrometric space-borne projects, which provide the next step in developing our knowledge of the Universe. Some of these projects promise to improve the accuracy of determining positions and proper motions of stars by one or two orders of magnitude. The projects call for the measurement of both the limited number of stars (several thousands) and determination of positions and proper motions of many millions of cosmic objects. Along with astrometric determination of stellar positions, high-precision multicolor photometry is planned in these projects. A large variety of projects are based on interferometric principles, which allow for the measurement of angles with an accuracy of several arc microseconds, which is much higher than the instrumental diffraction limit. Such an accuracy will exceed by 2–3 orders of magnitude that achieved in the HIPPARCOS project. It is such an accuracy that is most attractive nowadays for solving current scientific problems.

According to the principle of taking astrometric measurements, all space projects can be divided into two groups: those involving a survey of celestial sphere by the scanning method and observations of objects with an instrument maintaining a constant spacecraft orientation during exposition. By now the astrometric measurements have been carried out aboard two spacecraft: the HIPPARCOS satellite and Hubble space telescope. Observations made with HIPPARCOS are performed by the scanning technique, while the Hubble telescope is constantly oriented toward the measurable object. The accuracy of astrometric measurements achieved by both instruments is about the same although HIPPARCOS performed wide-angle astrometry and the Hubble telescope, narrow-angle astrometry.

* E-mail address for contacts: rykhlova@inasan.rssi.ru

1063-7737/00/2609-0618$20.00 © 2000 MAIK "Nauka/Interperiodica"

An improvement of accuracy of measurements of celestial objects' coordinates reveals additional sources of measurement errors. At low accuracy, their role is negligible, and they are not considered at all. Micrometeorite impacts on the spacecraft surface is one of such sources of measurement errors. This effect is of prime significance when the measurements are made by the method of scanning of the celestial sphere.

EFFECT OF MICROMETEOR IMPACTS ON MEASUREMENTS OF OBJECT'S COORDINATES BY THE SCANNING TECHNIQUE

Scanning the celestial sphere from the HIPPARCOS satellite was made on the sky areas spaced apart at the base angle $\alpha = 58°$. Both areas were observed in a single field of view. Scans of different portions of the celestial sphere are obtained by moving the spacecraft rotation axis. Observation of a star in the same field of view makes it possible to determine a current value of the period of spacecraft rotation about its axis, while observation of the given star in the other field enables one to refine the base angle value. Thus, a complete closure at the great circle occurs at the rotation period. It is supposed that the angular rotation velocity is constant on this time interval. Any alteration of the rotation velocity on the interval equal to the one period of rotation about the satellite axis leads to measurement errors.

Consider the following model of astrometric measurements by the scanning spacecraft. Let the satellite have the spin period T and the base angle α. Then the time T^* of satellite rotation through the base angle is

$$T^* = T\alpha/2\pi, \quad (1)$$

where α is in radians. We denote the satellite mass by M; its moment of inertia, by I; and spacecraft's characteristic radius, by R. In the simplest model, a satellite of spherical shape with uniform density distribution is considered. Then, $I = 0.4MR^2$.

Consider the micrometeorite of mass m, which flies at the speed v and hits the satellite surface. According to the momentum conservation law, the additional rotation rate of the satellite caused by micrometeorite impact is

$$\Delta\omega = \frac{5}{2}\frac{mrv}{MR^2}, \quad (2)$$

where r is the impact flyby distance for the micrometeorite that struck the satellite surface. Assuming that the micrometeorite stream is isotropic, the additional angular velocity directed along the spacecraft rotation, caused by the impact of a single micrometeorite, is obtained by integrating over all directions:

$$\langle\Delta\omega\rangle = \frac{5}{8}\frac{mv}{MR}. \quad (3)$$

The error in measuring the angle $\Delta\varphi$ caused by the jump-like alteration of the spacecraft angular velocity, defined by formula (3), is

$$\Delta\varphi = \langle\Delta\omega\rangle T^*. \quad (4)$$

The micrometeorite stream in the Earth's neighborhood is well studied in the mass range from 10^{-18} to 1 g (Grun *et al.*, 1985; Divine *et al.*, 1993). Using the results of these studies, we devised the function $\Phi(m^*)$ that describes the stream of micrometeorites with mass above m^*. Knowing the spacecraft surface area and time T^*, we can easily estimate the mass m^* of the micrometeorite that collides with the spacecraft for the time T^*.

The $\Delta\varphi$ value determined in this way characterizes the error in determination of the base angle obtained from measurements of a single star. The measurement processing procedure for the HIPPARCOS satellite was published in the catalog by Perryman *et al.* (1997). With allowance for this technique, we obtain a considerably lower error because the data are processed simultaneously for a large number of stars. Thus, for HIPPARCOS, we obtain the following estimate for the error caused by the satellite collisions with micrometeorites: $\Delta\varphi = 180$ arc microseconds. Micrometeorites producing such errors have a mass of about 6×10^{-11} g and strike the satellite on average every 20 minutes. In the time interval between the instants of observation of two measured stars, the effect of micrometeorite impacts is, as a rule, negligible. However, owing to the sporadic character of the micrometeorite stream, impacts of rather large bodies are also possible. These impacts are able, even in such short time interval, to introduce a significant error in the measurement of the angle between stars. Using the obtained dependence of the impact rate on the micrometeorite mass, one can readily estimate the probability of such events: rough measurement errors may reach a few arc seconds once a year and may exceed the accuracy of a single measurement (10 arc milliseconds) once a day. These estimates agree well with those made by the authors of the HIPPARCOS catalog. Processing procedure, according to the above method, leads to the smoothing of errors of single measurements, while the base angle is determined from observations of a large number of stars. Therefore, according to our calculations, the root-mean-square error, estimated for the entire sample of stars $\Delta\varphi^*$, is 5 arc microseconds. Taking into account the accuracy of the HIPPARCOS catalog (Perryman *et al.*, 1997), equal to 0.7 arc milliseconds (700 arc microseconds), such an error is negligible and, therefore, in no ways affects the accuracy of the results obtained. Our error estimate is consistent well with the results obtained by the authors of the HIPPARCOS catalog (Perryman *et al.*, 1997).

DISCUSSION

The estimate obtained by us for HIPPARCOS shows that the transition to the microsecond measurement

Table

Project	Nominal measurement accuracy, arc microsec	Satellite radius, m	Rotation period, s	Base angle	$\Delta\varphi$, arc microsec	$\Delta\varphi^*$, arc microsec
DIVA (Germany) (Roeser, 1999)	150	0.8	7200	100	22350	50
GAIA(ESA) (Lindegren and Perryman, 1996)	5	1.5	7200	58	1600	8
FAME 99(USA) (Horner *et al*., 1999)	50	1.15	2400	81.5	250	0.6
Struve (Russia) (Ershov *et al*., 1995)	500	1.5	8640	70	3300	40
LIGHT (Japan) (Yoshizawa *et al*, 1997)	50	0.75	8640	90	6750	100
HIPPARCOS(ESA) (Perryman *et al*., 1997)	700	0.8	7680	58	180	5

accuracy makes it necessary to take into account collisions with micrometeorites when developing new projects of astrometric scanning instruments.

By now, a variety of projects of astrometric satellites have been suggested in which the measurements are taken by the sky scanning method. We estimated the value of $\Delta\varphi$ for some of these projects. Since the methods of processing the measured quantities are not outlined in detail in most of suggested and currently discussed projects of space-borne astrometric instruments, we assumed that these methods are similar to that employed in the HIPPARCOS mission. On this basis, we estimated the errors of the output catalogs due to collisions with micrometeorite streams. The results of these estimates are listed in the table.

We see from this table that the error $\Delta\varphi$ is large in all suggested projects. This error is comparable to or exceeds the error of individual measurements, implying that collisions with micrometeorites represent one of the most essential sources of measurement errors. Nevertheless, the accuracy stated for these projects can be attained by joint processing of observations of many stars. However, even in this case the error $\Delta\Phi^*$ value due to micrometeorite impacts was found to be comparable to the stated accuracy of the catalogs obtained in the projects.

It is known that micrometeorite streams have seasonal and random, hundredfold and more considerable, variations (McDonnel *et al.*, 1997). As a result, in scanning various portions of the sky in various seasons, zones with anomalous error value may appear, which deteriorates the quality of astrometric catalogs. When designing the projects with submillisecond accuracy, one should take into account the very fact of the influence of the micrometeorite stream, which imposes restrictions on the choice of sizes, mass, and rotation velocity of scanning instruments. A detailed examination of the effect of micrometeorites on the spacecraft is also required in observations of various portions of the sky in different seasons.

It is noteworthy that the projects of instruments maintaining a constant orientation in space during the exposition time, such as Lomonosov (Nesterov *et al.*, 1992), SIM (Denner and Anvin, 1999), and Osiris (Boyarchuk *et al.*, 1999), have virtually no errors due to collisions with micrometeorites.

REFERENCES

1. A. A. Boyarchuk, A. V. Bagrov, A. M. Mikisha, *et al.*, Kosm. Issled. **37**, 3 (1999).
2. *Space Interferometry Mission (SIM)*, Ed. by R. Danner and St. Unwin (JPL, Pasadena, 1999).
3. N. Divine, E. Grun, and P. Staubach, in *Proceedings of the 1st European Conference on Space Debris, Darmstadt, 1993*, p. 245.
4. *STRUVE Cosmic Astrometric System*, Ed. by V. N. Ershov, I. I. Kanaev, and I. M. Kopylov (Glagol, St. Petersburg, 1995).
5. E. Grun, H. A. Zook, H. Fechtig, and R. H. Giese, Icarus **62**, 244 (1985).
6. S. D. Horner, M. E. Germain, T. H. Greene, *et al.*, in *Proceedings of the International Conference on Optical and IR Interferometry from Ground and Space, Dana Point, 1999*, p. 21.
7. L. Lindegren and M. A. C. Perryman, Astron. Astrophys., Suppl. Ser. **116**, 579 (1996).
8. J. A. M. McDonnell, N. McBride, and D. J. Gardner, ESA SP-393, 391 (1997).
9. *Lomonosov Space-Borne Astrometric Experiment*, Ed. by V. V. Nesterov, A. M. Cherepashchuk, and E. K. Sheffer (Mosk. Gos. Univ., Moscow, 1992).
10. M. A. C. Perryman, H. Hassan, T. Batut, *et al.*, ESA SP-1111, **1** (1989).
11. M. A. C. Perryman, K. S. O'Flahetry, F. van Leeuwen, *et al.*, ESA SP-1200, **1-17** (1997).
12. S. Roeser, in *Proceedings of the International Conference on Optical and IR Interferometry from Ground and Space, Dana Point, 1999*, p. 38.
13. M. Yoshizawa, K. Sato, J. Nishikawa, *et al.*, ESA SP-402, 795 (1997).

Translated by A. Kozlenkov